HYPERSONIC WAKES

Thesis by
John Francis McCarthy, Jr.

In Partial Fulfillment of the Requirements
For the Degree of
Doctor of Philosophy

California Institute of Technology
Pasadena, California
1962

ACKNOWLEDGEMENTS

ABSTRACT

An experimental investigation was made of the flow field behind a
two-dimensional circular cylinder at a nominal Mach number of 5.7.
The free-stream Reynolds number based on the cylinder diameter was
varied over a range from 4300 to 66,500 by changing both the diameter of
the cylinder and the stagnation pressure of the wind tunnel.
Pitot-pressure, static-pressure, and total-temperature measurements
were made at various distances behind the cylindrical rod in order to
determine the state properties in the wake. Base-pressure measurements
were also taken at various Reynolds numbers.

From these measurements, the transition from laminar to turbulent
flow in the wake was determined and successfully correlated with other
data. A transition Reynolds number based on local conditions and the
length of laminar run was determined. Extensive comparison of the
experimental data with Kubota's theory for laminar flow was then made.
A satisfactory comparison was made between theory and experiment.
Because of the nature of the tests conducted, only a qualitative comparison
was made with the theory of Lees and Hromas for turbulent flow.

CONTENTS

APPENDICES

ILLUSTRATIONS

TABLES

NOMENCLATURE

A   Constant determined from initial conditions

B   Constant determined from initial conditions

C   Chapman-Rubesin constant in linear viscosity-temperature relation,

$$C = \frac{\mu_r}{\mu} \frac{T}{T_r}$$

C_p Pressure coefficient, $\dfrac{\Delta p}{q}$

c_f Skin-friction coefficient, $\dfrac{\tau}{q}$

c_p Specific heat at constant pressure

D_N Diffusivity number, $\displaystyle\lim_{y \to 0} \frac{y^2}{\ln \frac{w_{\mathbb{C}}}{w}}$

$\overline{D_N}$ Transformed diffusivity number, $\displaystyle\lim_{\overline{y} \to 0} \frac{\overline{y}^2}{\ln \frac{w_{\mathbb{C}}}{w}}$

d   Cylinder diameter

G   Total-enthalpy excess, $\dfrac{H}{H_e} - 1$

g   Total-enthalpy ratio, $\dfrac{H}{H_e}$

H   Total enthalpy

h   Static enthalpy

k   Thermal conductivity

L_{2-D} Length of two-dimensional flow

M   Mach number

M_1 Mach number which would exist at θ_s without separation

N Wake-width constant defined by, $w_e = \dfrac{1}{N}$

p Static pressure

p_{atm} Atmospheric pressure

p_b Base pressure

p_o Free-stream stagnation pressure, absolute

p_{o_g} Free-stream stagnation pressure, gage

Δp Pressure increment

Pr Prandtl number

Q Heat transfer to the body

q Dynamic pressure

R Gas constant

Re_d Free-stream Reynolds number based on cylinder diameter,

$$\frac{\rho_\infty u_\infty d}{\mu_\infty}$$

Re_x Reynolds number based on distance along body and conditions at edge of boundary layer

Re_T Townsend Reynolds number, $\dfrac{\Delta u \, y_e}{\epsilon_T}$

T Absolute temperature

T_{aw} Adiabatic wire temperature

T_o Stagnation temperature

u Component of velocity parallel to wake centerline

$\bar{u}$ Transformed u, $\dfrac{u}{u_e}$

Δu $u_e - u_{\mathcal{C}}$

θ Angle of cylinder measured from stagnation point

θ_c Turning angle

θ_w Wave angle

μ Dynamic viscosity coefficient

ξ Variable in x-direction

ρ Density

σ Prandtl number, $\dfrac{c_p \mu}{k}$

τ Shear stress

τ Time constant

ϕ Angle of trailing shock

χ Hypersonic viscous interaction parameter, $\dfrac{M_\infty^3 \sqrt{C_\infty}}{\sqrt{Re_{x_\infty}}}$

Subscripts:

$\mathcal{C}$ Centerline

e   Conditions at outer "edge" of wake

m   Measured

r   Reference

s   Conditions at separation point

0   Initial conditions (usually taken at neck)

∞ Free-stream conditions

v	Component of velocity normal to wake centerline
$\bar{v}$	Transformed v
W	Dependent variable
$\overline{W}$	Laplace transform of W, $\int_0^\infty W e^{-p\xi}\, d\xi$
w	Velocity defect, $1 - \dfrac{u}{u_e}$
x	Length along wake centerline measured from center of cylinder
$\bar{x}$	Transformed x, $\int_0^x \dfrac{\rho_e \mu_e u_e}{\rho_\infty \mu_\infty u_\infty}\, \dfrac{dx}{d}$, measured from neck
$\bar{x}_o$	Effective origin for $\bar{x}$ upstream of neck
x_1	Distance measured from beginning of boundary-layer growth
y	Length normal to wake centerline measured from center of cylinder
$\bar{y}$	Transformed y, $\dfrac{u_e}{u_\infty}\sqrt{R_{e_d}} \int_0^y \dfrac{\rho}{\rho_\infty}\, \dfrac{dy}{d}$
α	Angle of shear layer
β	$\sqrt{M^2 - 1}$
γ	Specific-heat ratio
δ	Wake thickness, $2y_e$
δ	Wedge angle
ϵ	Angle of wake growth
ϵ_T	Turbulent diffusivity
η	Variable in y-direction
θ	Momentum thickness, $2\int_0^\infty \dfrac{\rho u}{\rho_e u_e}\left(1 - \dfrac{u}{u_e}\right) dy$

I. INTRODUCTION

GENERAL DISCUSSION

Wakes present one of the oldest basic problems in the field of clas-
sical fluid mechanics. Although the low-speed regime of wakes has been
discussed in several treatises, (e.g., see References 1 to 6), it was only
until recently that research was directed toward the phenomenon of high-
speed flow. The development of intercontinental ballistic missiles and
hypersonic reentry vehicles has rekindled interest in high-speed wakes.

One of the more interesting aspects of hypersonic wakes is the
extreme length of observable phenomena. For example, it is reported by
Jacchia (Reference 7) that during the descent of the 1957 Soviet satellite,
Beta One, the burning object trailed a luminous tail approximately 100 km
long A representative comment of Jacchia's relevant to the visual
observation of Beta One's descent cites the spectacular character of the
object's reentry:

> "Tail was 25-30 nautical miles long; from white it degraded
> into dark red and then into a black smoke trail without seeing
> the end of it."

Contemporary techniques employed in predicting observables are as
yet inadequate because the theoretical models devised for this purpose have
not received experimental confirmation. While some information about
gross quantities (i.e., wake width) has been obtained from downrange

measurements and ballistic ranges (e.g., References 8 and 9), it is difficult to obtain detailed state properties which would permit the basic structure of the wake to be determined experimentally. For example, Lees and Hromas (Reference 10) were able to confirm their theory only by shadowgraph and schlieren measurements taken in ballistic ranges; consequently, no confirmation of state properties has thus far been possible. For the laminar flow regime, the severity of the situation is even more critical because of the dearth of existent experimental data.

Perhaps the major obstacle in correlating theory and experiment in hypersonic wakes resides in the difficulty of obtaining reliable and detailed experimental data. Atmospheric reentry involves a temperature/Mach regime which cannot be effectively simulated by known devices for extended periods. Therefore, only limited data have been obtained, either from short-duration experimental facilities (shock tunnels and ballistic ranges) or from actual flight -- an expensive, unreliable technique. Unfortunately, these data have been inadequate in proving even the most unsophisticated theories of hot, viscous hypersonic wakes.

One tool generally overlooked in the study of hypersonic wakes is the conventional wind tunnel. Although the wind tunnel does not simulate the high Mach number and the high temperature attained during reentry, it does make possible the check-out of theoretical models by permitting the measurement of state properties throughout a hypersonic flow field. One major advantage inherent in wind tunnel testing is the ability to vary

Reynolds number -- an extremely important parameter in viscous and wake phenomena -- independently of other quantities, enabling the Reynolds number effect to be determined explicitly. A systematic hypersonic wake study program employing the hypersonic wind tunnel as the experimental tool has been in progress at GALCIT for some time.

Figure 1, which is a schlieren photograph of a circular cylinder at Mach number 5.7, enables the flow field to be segregated into various classical regimes. These regimes are presented in Figure 2. Each of these regimes can be treated analytically by suitable techniques. After individual analyses, these regimes can be figuratively assembled in a manner analogous to piecing together a jigsaw puzzle -- matching boundary conditions and, if necessary, using iterative procedures. The present investigation is focused upon the wake region shown in Figure 2.

At GALCIT the problem has been grossly divided into three regimes: (1) neck, (2) near wake, and (3) far wake. This thesis is one of several wherein the near wake is investigated. In the near wake regime the static pressure has not yet reached the ambient, an effect which may contribute to the wake structure. Previous investigations have been only concerned with specialized measurements. For example, Demetriades (Reference 11) has investigated transition by hot-wire anemometry; Mohlenhoff (Reference 12) and Kingsland (Reference 13) have studied mixing by means of helium and argon diffusion; Dewey (Reference 14) is extending the work of Demetriades and will study the neck region; Behrens (Reference 15),

d = 0.300 IN.
P_{o_g} = 85.00 PSIG
T_o = 263°F
M_∞ = 5.69
Re_d = 66.5 × 10^3
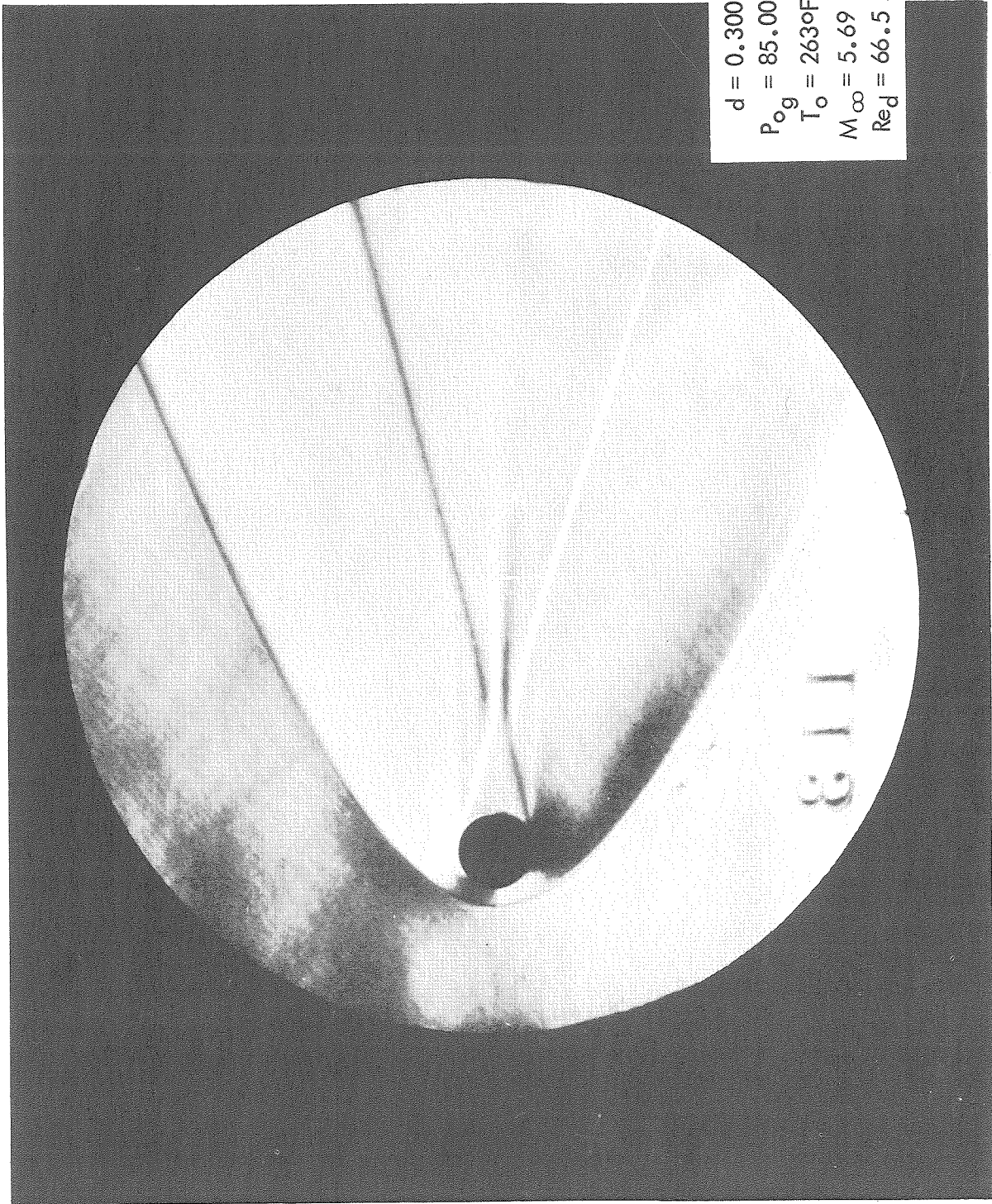
Figure 1. Schlieren Photograph of the Flow Around Cylinder
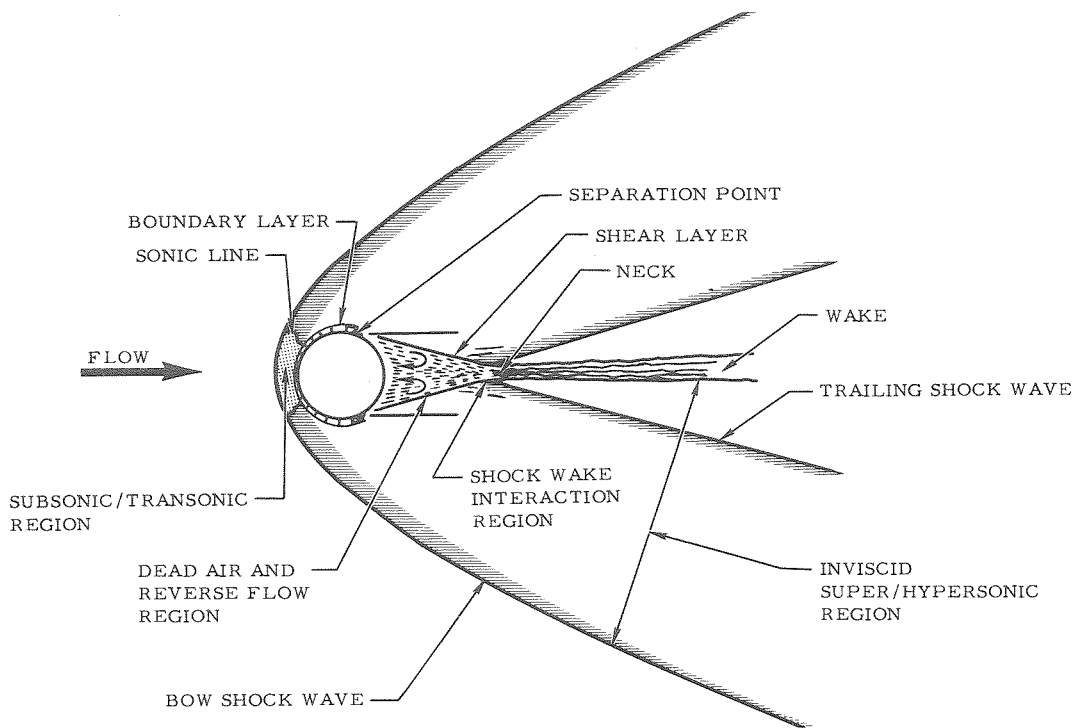
Figure 2. The Flow Field to be Analyzed

investigating the far wake by utilizing very thin heated wires as models, is

engaged in determining flow properties in the far wake by means of hot-wire

anemometry.

Lees and Hromas (Reference 10) have indicated several important

differences between the low-speed and high-speed wake structure behind

blunt bodies, viz: the existence of a stable shear layer (see Figures 1 and

2); the very small initial momentum thickness or drag at the neck compared

to the total drag of the body; and the absence of characteristic shedding

frequencies, at least in unionized air at supersonic and hypersonic speeds.

The theoretical problem of hypersonic wakes was first treated by

Feldman (Reference 16) who devised a simple model of the wake flow.

Feldman's basic approach has been extended by Lykoudis (Reference 17) who, however, added no analytical innovations. More recently, Lees and Hromas (Reference 10) have attacked the problem of turbulent diffusion in the wake by using integral methods to solve the boundary-layer equations. The two-dimensional laminar hypersonic wake with streamwise pressure gradient has been solved by Kubota (Reference 18) using linearized equations.

The purpose of the present investigation is to obtain reliable experimental data of the wake flow behind a two-dimensional circular cylinder -- the simplest model that could be devised. With these data supplemented by other experiments, transition from laminar to turbulent flow in the wake can be defined as a function of Reynolds number. Comparison between theory and experiment for the laminar region using Kubota's theory is then possible. Comparison between theory and experiment in the turbulent region will then be made to the extent possible as limited by the accuracy of the data. Whenever possible, an attempt will be made to define "universal" distributions of state properties based on experimental data and to determine the variation of centerline values with Reynolds number.

TECHNICAL APPROACH

The configuration for the experimental investigation is shown in Figure 3 where the basic model, a cylindrical rod, is mounted in the side plates of the hypersonic wind tunnel. The number and spacing of the vertical supports used for holding measuring probes were such that the
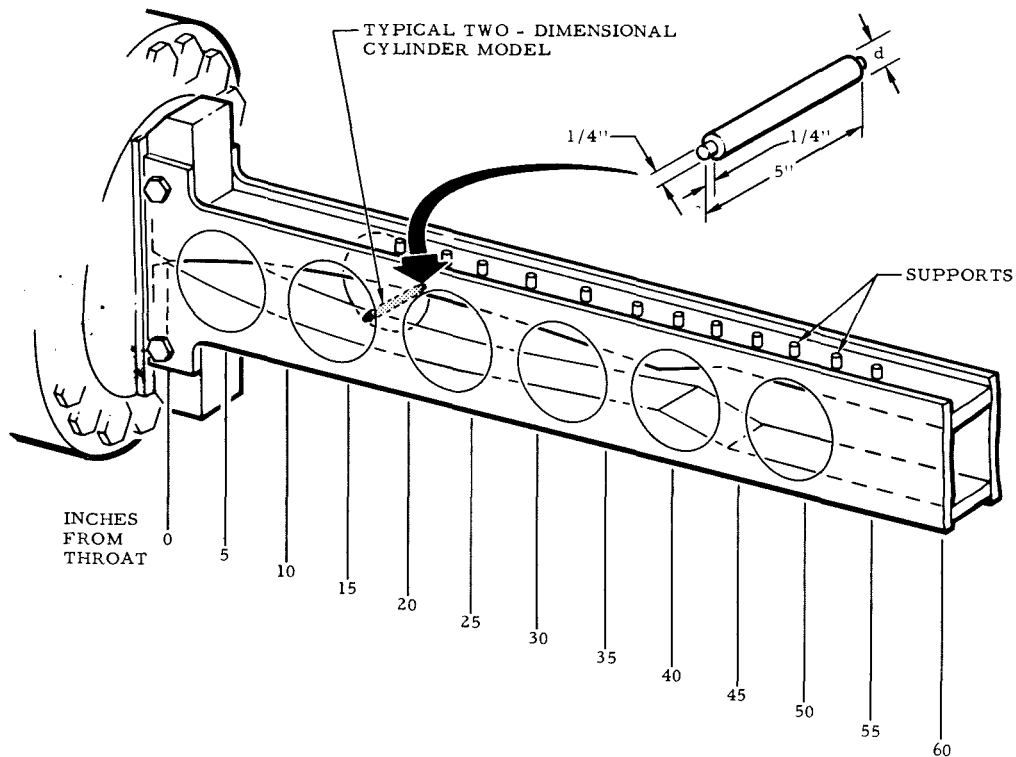
Figure 3. Model Installation

wake could be investigated at any desired downstream axial station. To

obtain a systematic variation of Reynolds number, the 11 combinations of

cylinder diameter and wind tunnel stagnation pressure shown in Table I

were tested. The 0.300-inch-diameter cylinder was close to the model

which could be conveniently tested in the wind tunnel without starting

difficulties. The 0.100-inch-diameter model represented the smallest

model that could be tested with enough resolution in measurements to give

an adequate definition of state properties. The wind tunnel stagnation

pressure, as limited by the compressor plant, could be varied between

the 0.00 and 100.00 psig limits.

Table I Test Summary

MODEL d INCH	P_{o_g} PSIG	T_o °F	Re_d $\times 10^{-3}$
0.300	85.00	263	66.5
0.300	60.00	263	49.4
0.300	35.00	262	32.7
0.300	10.00	262	16.7
0.200	96.68	264	49.3
0.200	59.48	263	32.7
0.200	22.48	262	16.6
0.200	3.80	260	8.58
0.100	59.42	263	16.3
0.100	22.54	262	8.28
0.100	3.84	260	4.29

Table I indicates that an attempt was made to duplicate Reynolds number by varying both the density and the model size. An exact duplication was not possible because of the day-to-day variations in atmospheric pressure and the variations in free-stream Mach number caused by variable boundary-layer thickness on the nozzle walls with stagnation pressure. The 3-to-1 ratio in model size and the 6-to-1 ratio in absolute stagnation pressure, promised the possibility of obtaining a sufficient variation in Reynolds number necessary to the determination of its effect on wake properties.

After selecting the combinations shown in Table I, a complete definition of the flow field was attempted through experiment. Three state

properties were selected for experimental investigation: (1) pitot pressure, (2) static pressure, and (3) total temperature.

Pitot-pressure measurements drew initial attention because these were obtained accurately and quickly; they could also be used to define the geometry of the flow field as well as determine one state property.

Regarding static pressure, an experimental verification was attempted to demonstrate that the static pressure was constant with vertical distance in the wake (as expected from theory). Static pressures were then employed to determine the two-dimensionality of the flow field. Finally, axial traverses were made along the centerline to obtain a second state property.

Minimum effort was expended in determining total-temperature because the model used was almost completely insulated -- a factor which evoked only slight variations in total temperature. However, sufficient total-temperature data were gathered to determine the dependence of this state property on free-stream Reynolds number. In the process of investigating the "near" wake characteristics, it was necessary to make base-pressure measurements in order to adequately extrapolate static-pressure data upstream.

Once the flow field was established experimentally, the data were used to define transition from laminar to turbulent flow in order to separate these two regimes. "Universal" curves were defined whenever possible and comparisons with theory were made as limited by the nature of the data.

II. EXPERIMENTAL TECHNIQUES

GALCIT HYPERSONIC WIND TUNNEL

All tests were conducted in the GALCIT Hypersonic Wind Tunnel, Leg 1 (Figure 4). The test section of this tunnel is 5 inches in width and 5-1/4 inches in height. The wind tunnel is a continuous-flow, closed-return device with a nominal fixed Mach number of 5.7 in the region where the model was ultimately placed (17.34 inches from the throat). A complete description of the compressor and the associated instrumentation is given by Baloga and Nagamatsu (Reference 19).

The reservoir pressure ranged from 0.00 to 100.00 psig, with an accuracy of ±0.02 psig with corresponding Reynolds numbers between 33,000 and 260,000 per inch based on free-stream conditions. The automatically controlled reservoir temperature can be varied between 225 and 325 F. A reservoir temperature of 262 F was selected for all tests. This temperature closely approached the minimum for good flow without condensation effects for the nominal operating dew points (based on the test section survey discussed in Appendix A). The maximum temperature was limited to approximately 275 F by the saran tubing used in the pressure-recording systems. The reservoir temperature could be maintained constant to within ±1 F. The nominal operating dew point was less than -40 F; however, after approximately eight hours of steady
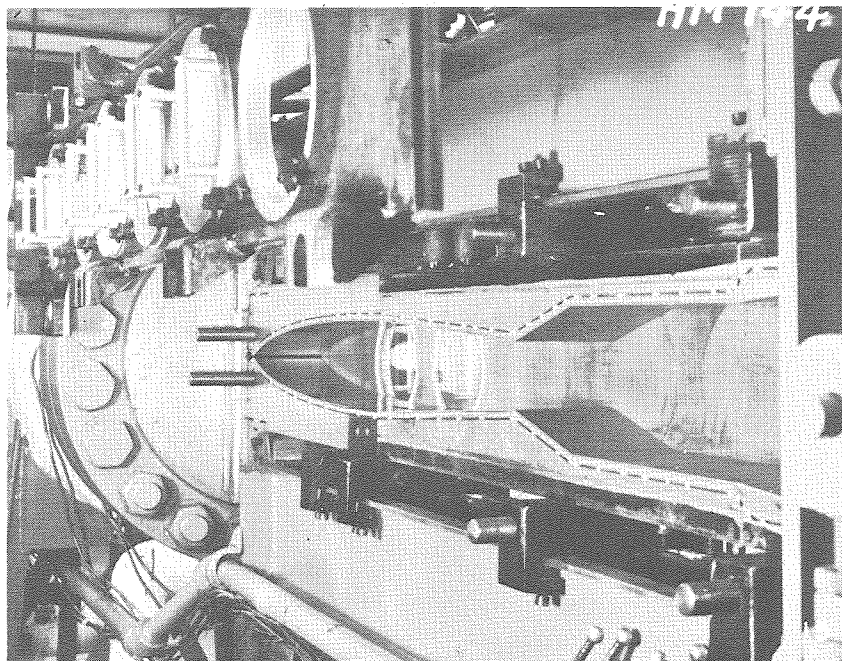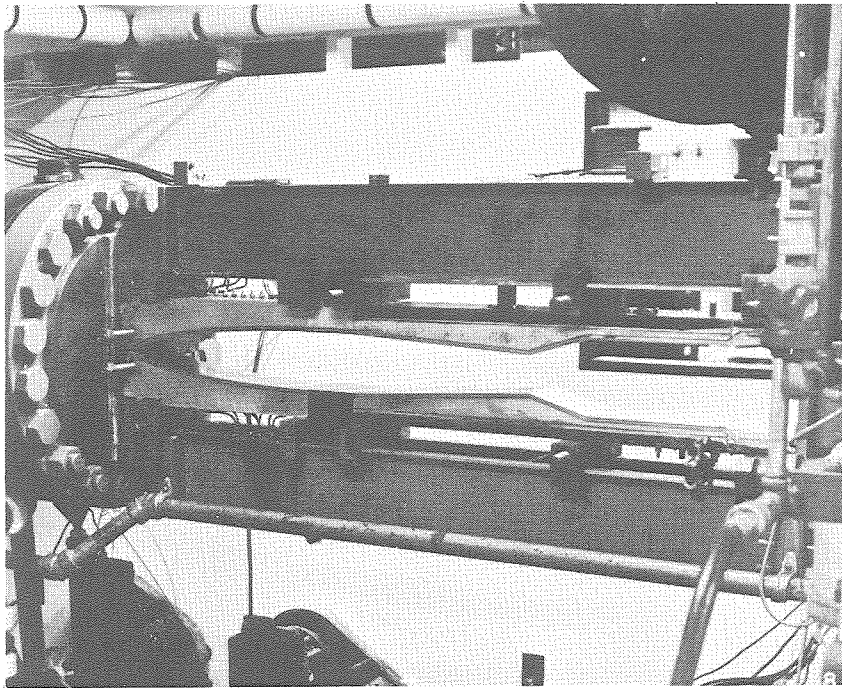
Figure 4. Leg I, GALCIT Hypersonic Wind Tunnel

testing the dew point began to deteriorate. No data were taken at dew points higher than -25 F.

To obtain maximum distance for the wake studies, two methods were employed to determine the most forward location of the test section rhombus. First, the entire test section was surveyed by a conventional rake, and pressure contours were established by feeding data into a conventional IBM 7090 program. (Details of this survey are discussed in Appendix A, where contours for a low stagnation pressure are presented.) The flow deteriorates with decreasing stagnation pressure.

The second method for determining the most forward position suitable for wake measurements was to change the axial location of the cylindrical model. Five different axial locations were selected. The most forward location was 13.12 inches from the throat; the most aft, 24.82 inches from the throat. Pitot-pressure surveys were made at each of these locations at various axial distances behind the model, and duplicability was determined. This procedure was precipitated by the unfortunate experiences of Mohlenhoff (Reference 12), Kingsland (Reference 13) and the author (Reference 20) each of whom tested too far upstream. In these latter tests unusual pitot-pressure surveys were obtained, which could not be repeated.

On the basis of these two methods, it was determined to locate the model position as far upstream as possible—17.34 inches from the throat (Figure 3). The downstream limitation of flow uniformity was determined

by disturbances orginating slightly upstream of the junction of the model
with the wind tunnel's sidewalls (discussed later in this section) and not by
the test-section rhombus.

PITOT-PRESSURE MEASUREMENTS

Obtaining reliable experimentally verified total-pressure surveys at
various axial distances in the wake and the adjacent inviscid flow region
constituted one of the experimental program's major efforts. Fortunately,
total pressure is one of the quantities which can be easily and accurately
measured by experiment. This quantity not only provides one flow
parameter, but also represents an accurate measurement of wake geometry.

Perhaps the most difficult problem encountered in obtaining satis-
factory pressure surveys was the attainment of a low time constant. As
shown in Reference 21, assuming Hagen-Poiseuille flow in the tubing, the
time constant of a pressure recording system is

$$\tau \sim \frac{\mu \, (\text{Vol}) \ell}{p \, d^4} \tag{1}$$

where

τ is the time constant

μ is the coefficient of viscosity of the measured gas

Vol is the internal volume of the system

ℓ is the length of the tubing

d is the diameter of the pressure probe

p is the measured pressure

Therefore, the pressure recording system was designed so as to minimize τ.

The small variable-reluctance pressure transducer shown in Figure 5 was selected as the basis for a very-low-time-constant pressure-recording system. Consequently, the volume of the transducer with its glass measuring tip was very small; also, the length of the tubing from pitot tip to diaphragm was minimal so that the time constant as defined by Equation 1 was minimized. The time constant of this pressure-recording system was about 50 milliseconds, as determined by driving the probe through the bow shock generated by the cylindrical model.

The magnetic circuit of this transducer consists of a shell, a magnetic coil, and an air gap—the air gap is varied by the deflection of
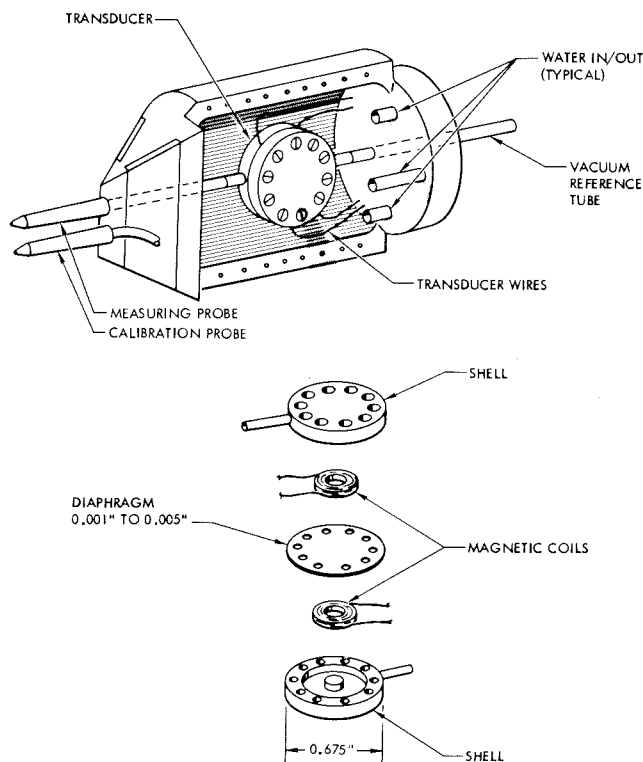
Figure 5. Installation of Variable-Reluctance Pressure Transducer

the diaphragm due to differential pressure. The range of the transducer can be varied from about ±0. 1 to ±0. 5 psig for the diaphragm thicknesses (0. 001 to 0. 005 inch) shown in Figure 5. Obviously, the range of the transducer decreases as the sensitivity is increased. Details of the theory and construction of this transducer are given by Smotherman (Reference 22).

The pressure transducer was excited by a 5-volt 20, 000-cycle carrier signal which was modulated by the magnetic circuitry, producing as final output a dc-signal up to 75 millivolts. Unfortunately, the final dc output of the transducer system was very sensitive to temperature. Since thermal environment to which the transducer was subjected varied over a large range, it was housed in a head and water-cooled so as to provide a uniform temperature during a vertical transverse (Figure 5). The temperature of the transducer was monitored by cementing a standard thermocouple on the transducer case (see Figures 5, 6 and 7).

Because of the characteristics inherent in the variable reluctance transducers used for the total-pressure measurements, it was necessary to use extreme care in the design and employment of the associated electronics. All wires had to be carefully shielded and excessive lengths avoided. An isolation transformer was used between the power source and the equipment (Figure 7). The transducer, installed as a conventional two-arm Wheatstone bridge (Figure 8), incorporates provisions for balancing the circuitry.
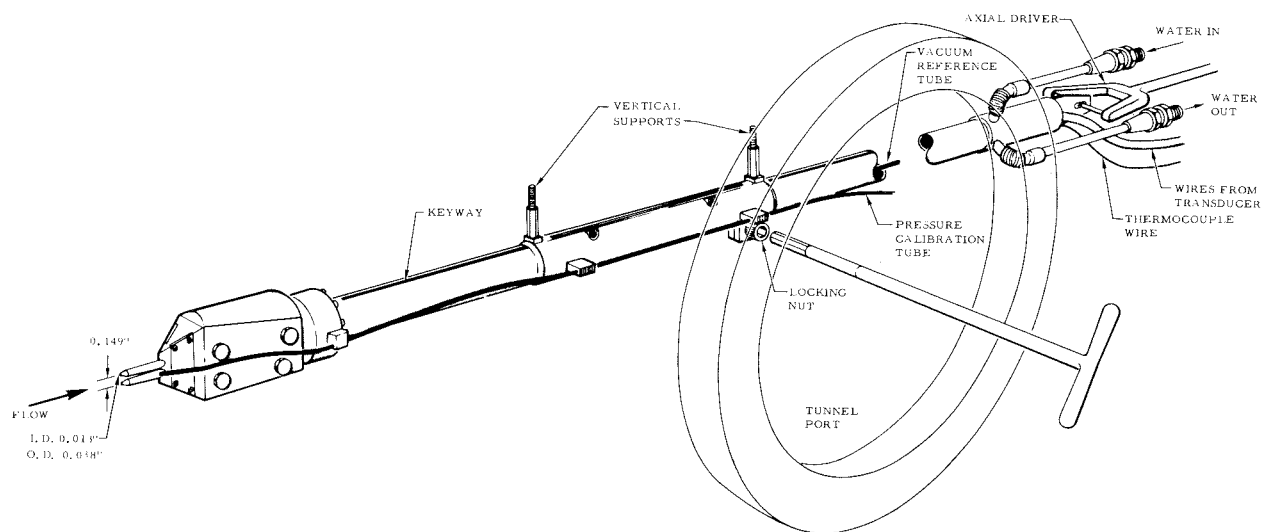
Figure 6. Pitot-Pressure Probe Recording System

Before the pressure signal was introduced into the autograph recorder, it was cleared of high-frequency noise by the low-pass filter shown in Figure 8. The filter was designed by conventional techniques (Reference 23). In designing the electronic circuitry, a floating shield was necessary to prevent ground loops. The entire electronic circuit was grounded at one location only (Figures 7 and 8).

The pitot-pressure probe was moved vertically from outside the tunnel by a rack which was activated by a motor-driven pinion (Figure 7). The probe-positioning gearing turned the helipot potentiometer which converted the probe position to a linear electrical signal. The electrical signal, in turn, was fed into the autograph recorder.
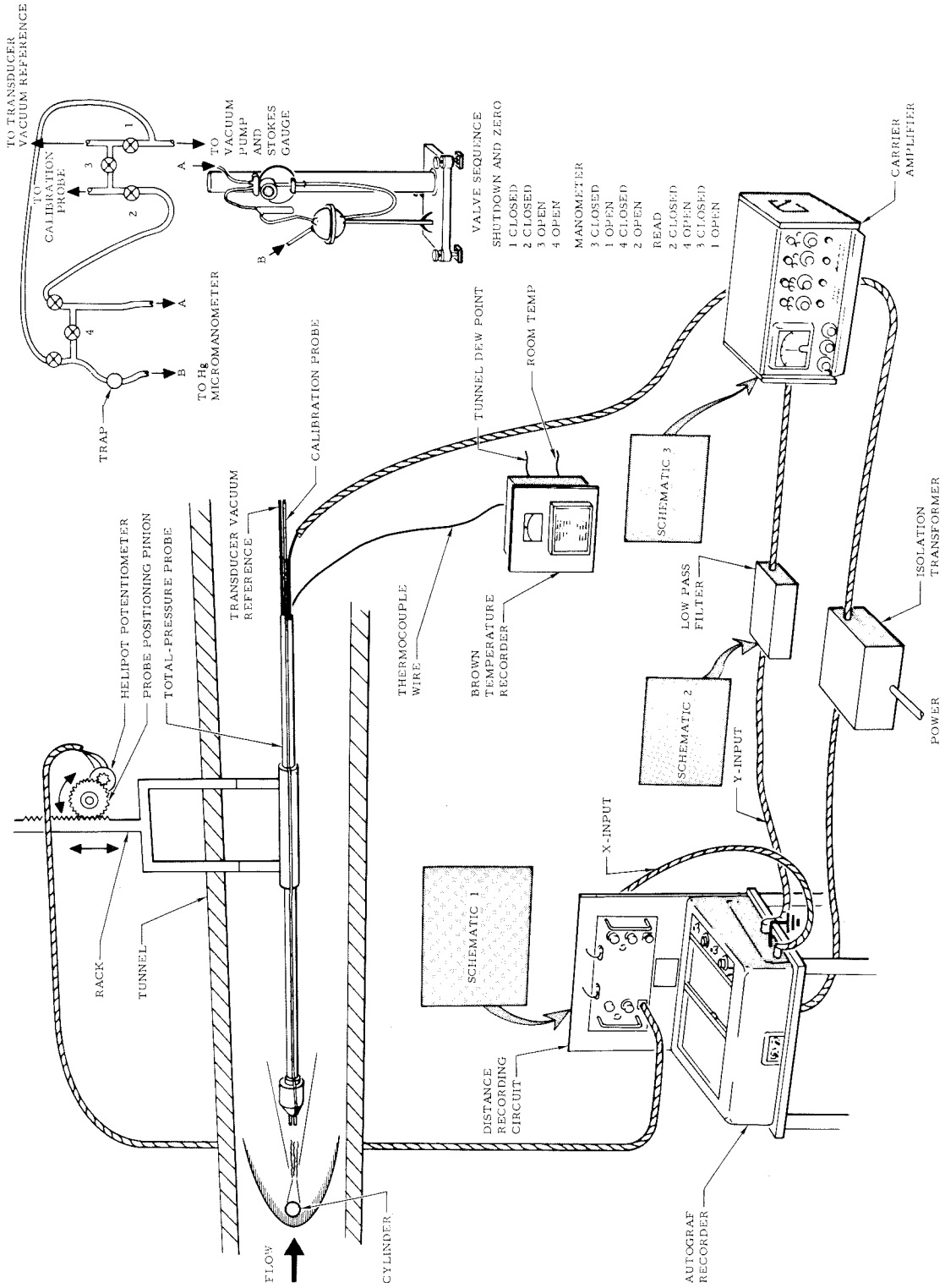
Figure 7. Pitot-Pressure Recording System
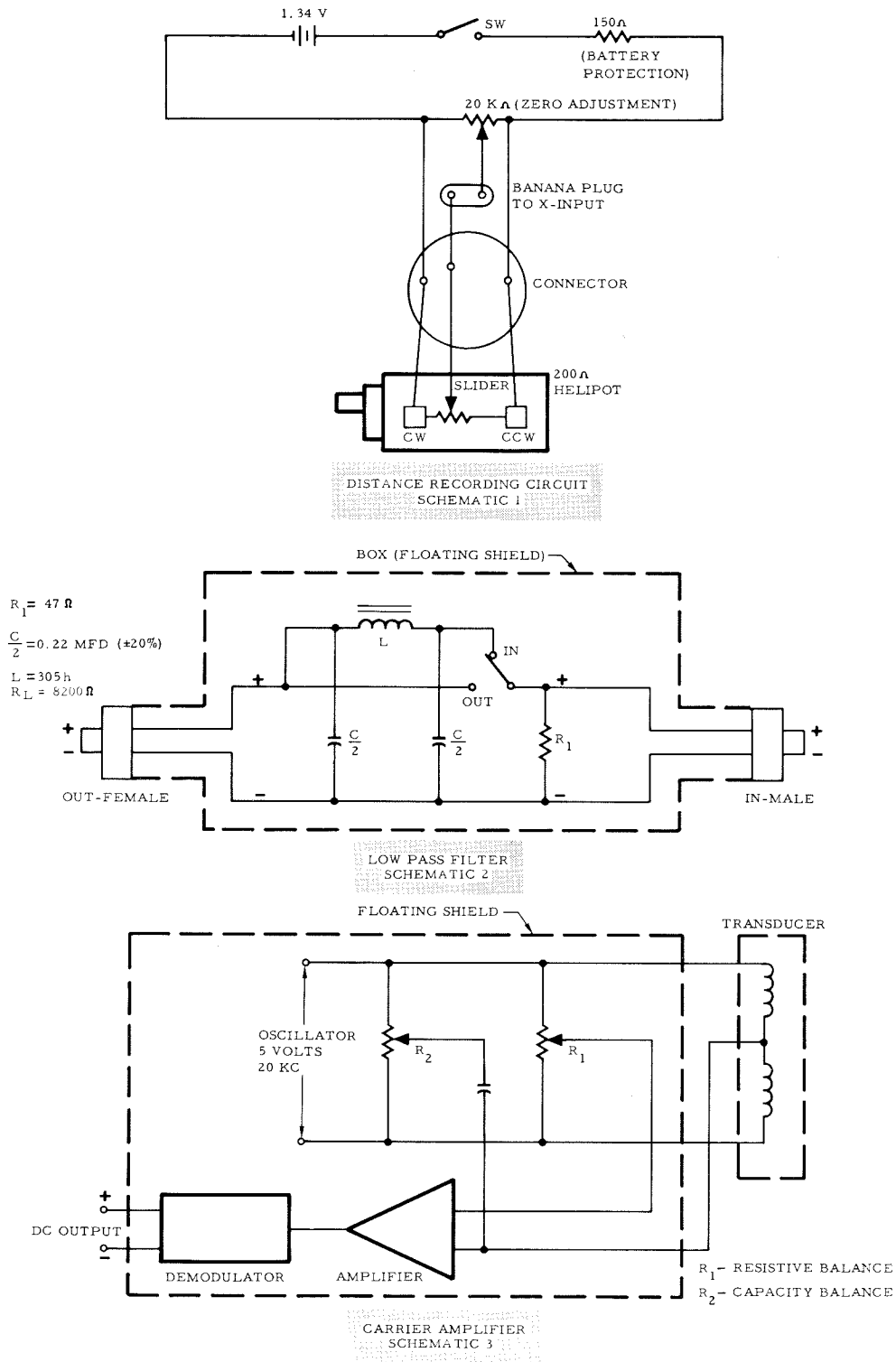
Figure 8.   Electronic Circuitry of Recording Systems

The autograph recorder is a null-balancing device which plots the data automatically. The electronic circuit for recording distances is shown in Figure 8. A 200-ohm helipot with linearity of 0.1 percent was used. The 200-ohm resistance of the helipot was much less than the resistance of the autograph recorder (2000 ohms); consequently, the linearity of the recorder was unaffected by the input signal. All distances could be recorded to ±0.001 inch. The final data were obtained as plots of pitot-pressure versus distance.

In the final test setup shown in Figures 6, 7, and 8, the reference side of the transducer was connected to a vacuum reference with a large effective capacitance, consequently, fluctuations in any component of the vacuum reference pressure system had little effect on the reference vacuum pressure. The measuring side of the transducer was connected to the glass tip. The tip was about 1-inch long and had the dimensions shown in Figure 6. The outside diameter of the apex of the glass tip was selected at 0.039 inch — small enough to obtain satisfactory resolution (Figure 9) and large enough to minimize the effects of Reynolds number (Section III).

To calibrate the transducer, another glass tip of exactly the same geometry as the original measuring glass tip was located a known distance, 0.149-inch, (Figure 6) below the measuring tip. This calibration tip was connected to the system shown in Figure 7 and was calibrated by a mercury micromanometer with which pressures could be measured to 0.001 cm mercury.

d = 0.300 IN.
x/d = 9.00
P_{o_g} = 35.00 PSIG
P_{atm} = 74.49 CM Hg
T_o = 262°F
Re_d = 31.7 X 10^3

(a) Laminar Flow

d = 0.300 IN.
x/d = 20.00
P_{o_g} = 85.00 PSIG
P_{atm} = 74.75 CM Hg
T_o = 263°F
Re_d = 65.1 X 10^3
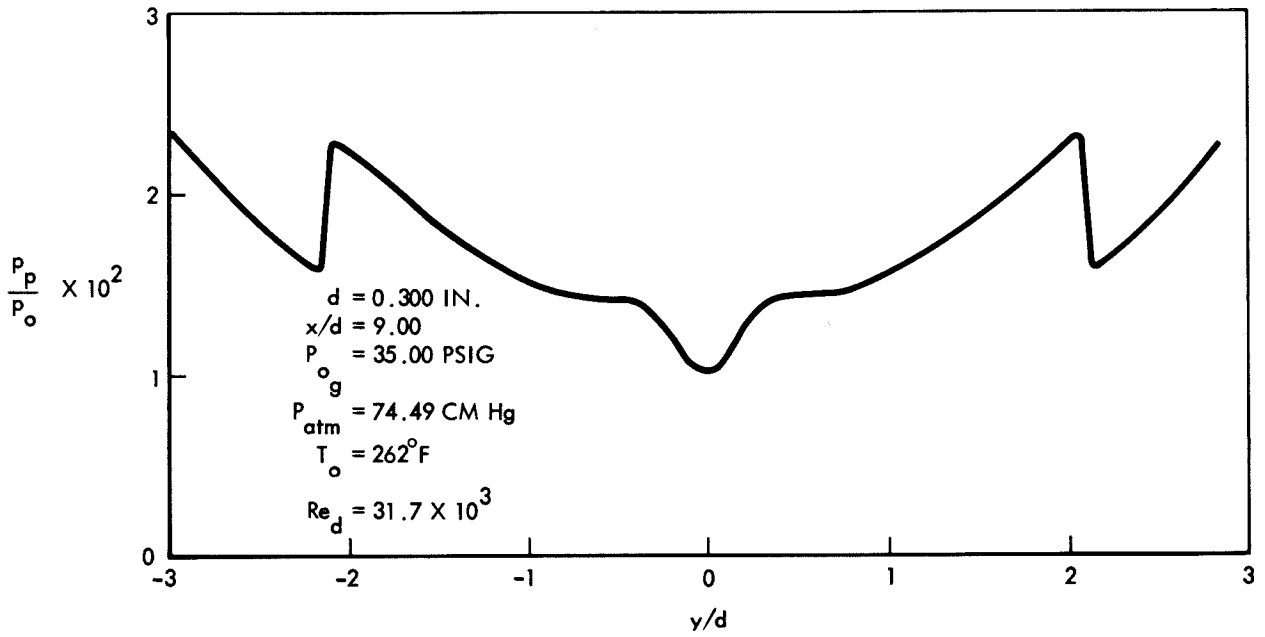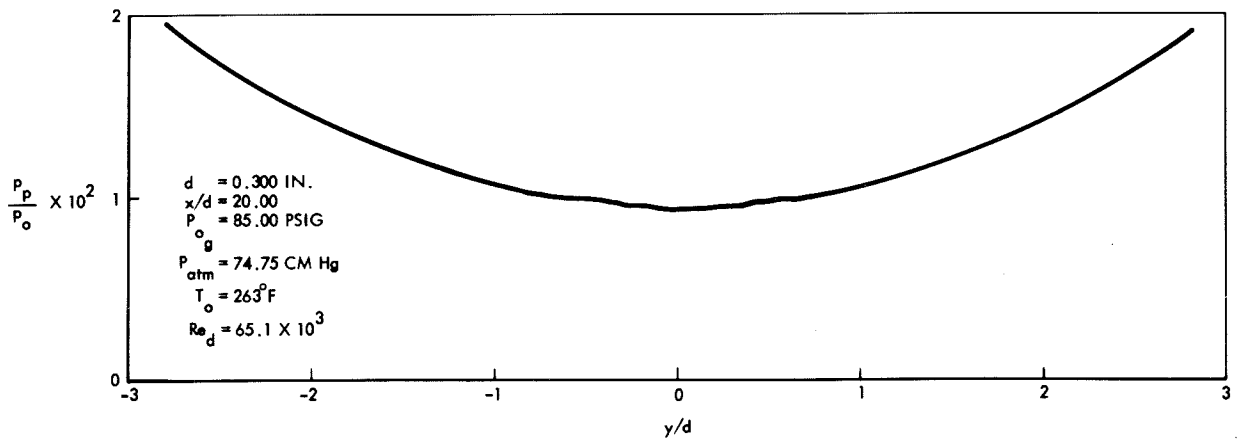
(b) Turbulent Flow

Figure 9.   Typical Pitot-Pressure Traces

The calibration procedure was to record the final voltage output of the pressure-recording system, move the probe vertically 0.149 inch, and measure the pressure with the mercury micromanometer. A typical calibration of the pressure-recording system is shown in Figure 10. All calibrations were obtained with the pressure-recording system installed ready for use. Pressure was varied by changing the stagnation pressure of the wind tunnel. The calibration resistances A - G of the carrier amplifier allowed for easy adjustment of the sensitivity of the autograph recorder. It is interesting to note that the linearity of the system was limited by the accuracy in reading ($p_p/p_o = \pm 10^{-4}$) rather than by any electronic component.
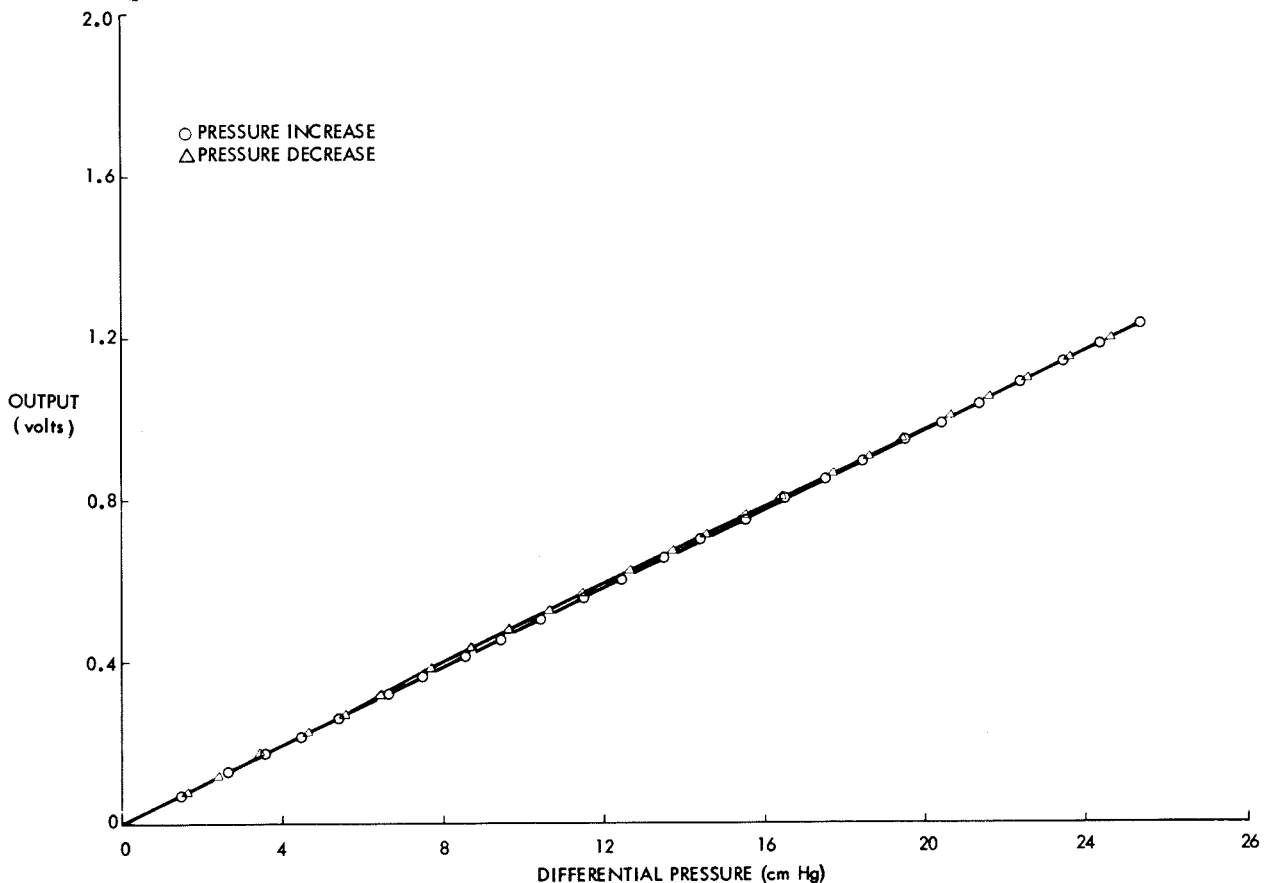
Figure 10. Typical Calibration of Pitot Pressure Recording System

Axial positioning was provided by the driving mechanism shown in Figure 6. Because of the nature of the installation, the probe was pivoted about a point downstream of the diffuser. An error induced by the angular motion about this pivot point would be introduced during a vertical survey if no provisions were made. Angular errors in axial positioning were eliminated by the locking nut shown in Figure 6. To preclude angular errors in axial positioning, the probe was driven to the desired axial position in the forward direction before tightening the locking nut from outside the wind tunnel. The axial position of the probe was determined by a counter attached to the axial driver. The counter was calibrated by inserting machine shim stock between the measuring probe and the cylindrical model after temperature equilibrium was established through several hours of wind tunnel operation.

Finally, because flow inclinations up to 15 degrees were encountered in the flow field, the device shown in Figure 11 was designed to determine the angle-of-attack sensitivity of the pitot probe. The long lever arm afforded good accuracy for small angles of attack, especially since the calibration counter had a turn ratio of 100 to 1. The results of this calibration are given in Figure 12, showing that the pitot probe is relatively insensitive to angle of attack in the range of interest (±15 degrees).

Typical pitot-pressure traces are shown in Figure 9. Isoaxiometric visualization of the entire flow fields for the combinations given in Table I
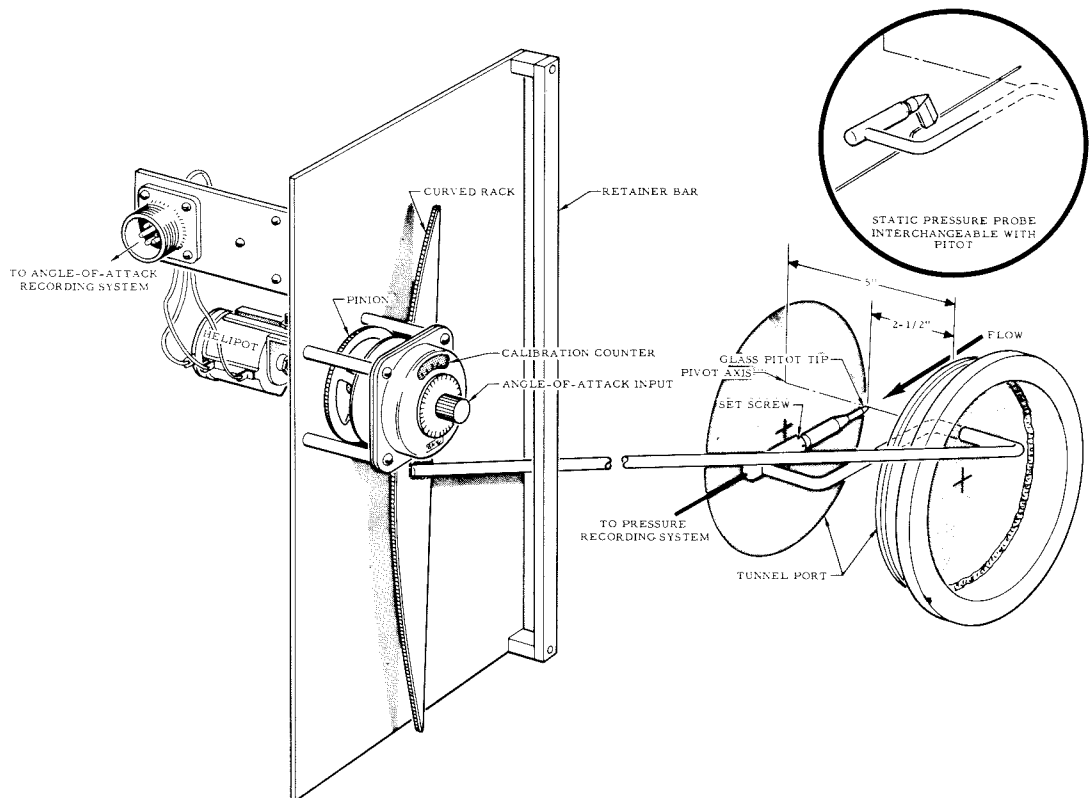
Figure 11.   Mechanism for Obtaining Angle-of-Attack
Sensitivity of Probes
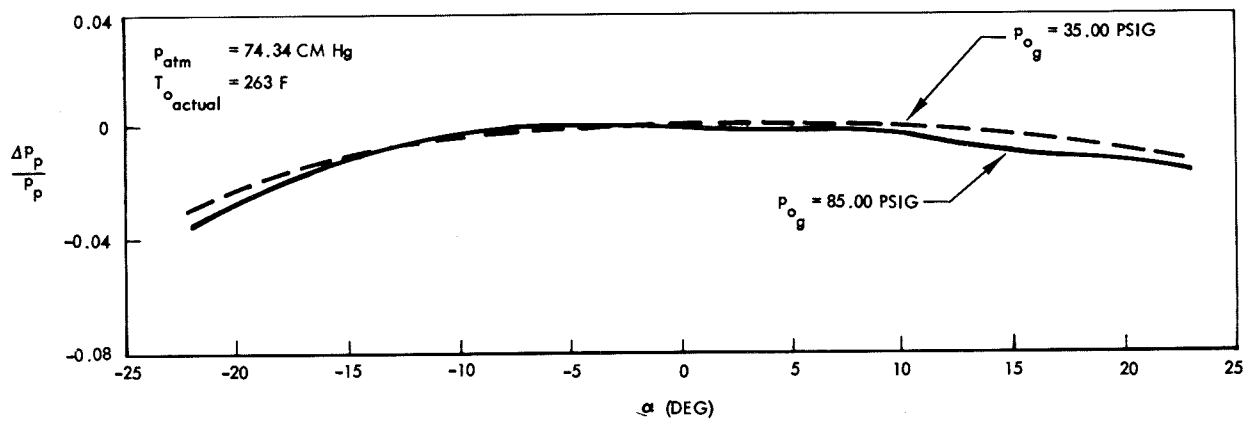
Figure 12.   Angle-of-Attack Sensitivity of Pitot-Pressure Probe

are shown in Figure 13. Figures 13.1a, 13.2a, 13.3a, and 13.4a represent enlarged versions of the flow field around the neck. Figures 13.9a, 13.10a, and 13.11a are the same as Figures 13.9, 13.10 and 13.11, respectively, but they are presented in reduced scale for vertical distance. Tunnel-empty surveys were made for each station of Figure 13 as a check on the quality of flow.

STATIC-PRESSURE MEASUREMENTS

Because of the extremely low static pressures measured, it was not practical to use the small variable-reluctance transducers shown in Figure 5. Attempts were made to use adaptations of these transducers with the static-pressure probe (shown in Figure 14) inside the wind tunnel; however, the inherent inaccuracies of the carrier-amplifier system prevented this scheme. Therefore, a very sensitive pressure transducer was employed. Transducer size, however, made the assembly of a pressure probe around the transducer impractical for measurements inside the wind tunnel. The time constant of the static-pressure recording system was approximately two seconds. Despite extensive precautions to prevent leakage (i.e., use of vacuum grease and glyptol at joints), it was necessary to encase the transducer in a vacuum vessel to obtain the required accuracies. In this manner, the pressure differential across any face was made very small.

The overall schematic of the static pressure recording system is shown in Figure 15. With the silicone manometer used, pressures could be read to an accuracy of ±1/10 micron of mercury. The valve sequence

Model: d = 0.300 inch
p_{og} = 85.00 psig
p_{atm} = 74.69 cm Hg
T_0 = 263°F
M_∞ = 5.69
Re_d = 66.5 x 10^3

FLOW

$\frac{p_p}{p_0} \times 10^2$

y/d

x/d =
1.00
1.50
2.00
2.50
3.00
3.50
4.50
5.00
6.00
7.00
8.00
9.00
10.00
15.00
20.00
25.00
30.00

x/d

y/d

Figure 13.1. Isoaxiometric Pitot-Pressure Traces

Model: d = 0.300 inch
p_{0g} = 85.00 psig
p_{atm} = 74.69 cm Hg
t_0 = 263°F
M_∞ = 5.69
Re_d = 66.5 x 10^3

FLOW

$\frac{p_p}{p_0} \times 10^2$

y/d

x/d =
1.00
1.50
2.00
2.50
3.00
3.50
4.00
4.50
5.00

x/d

y/d
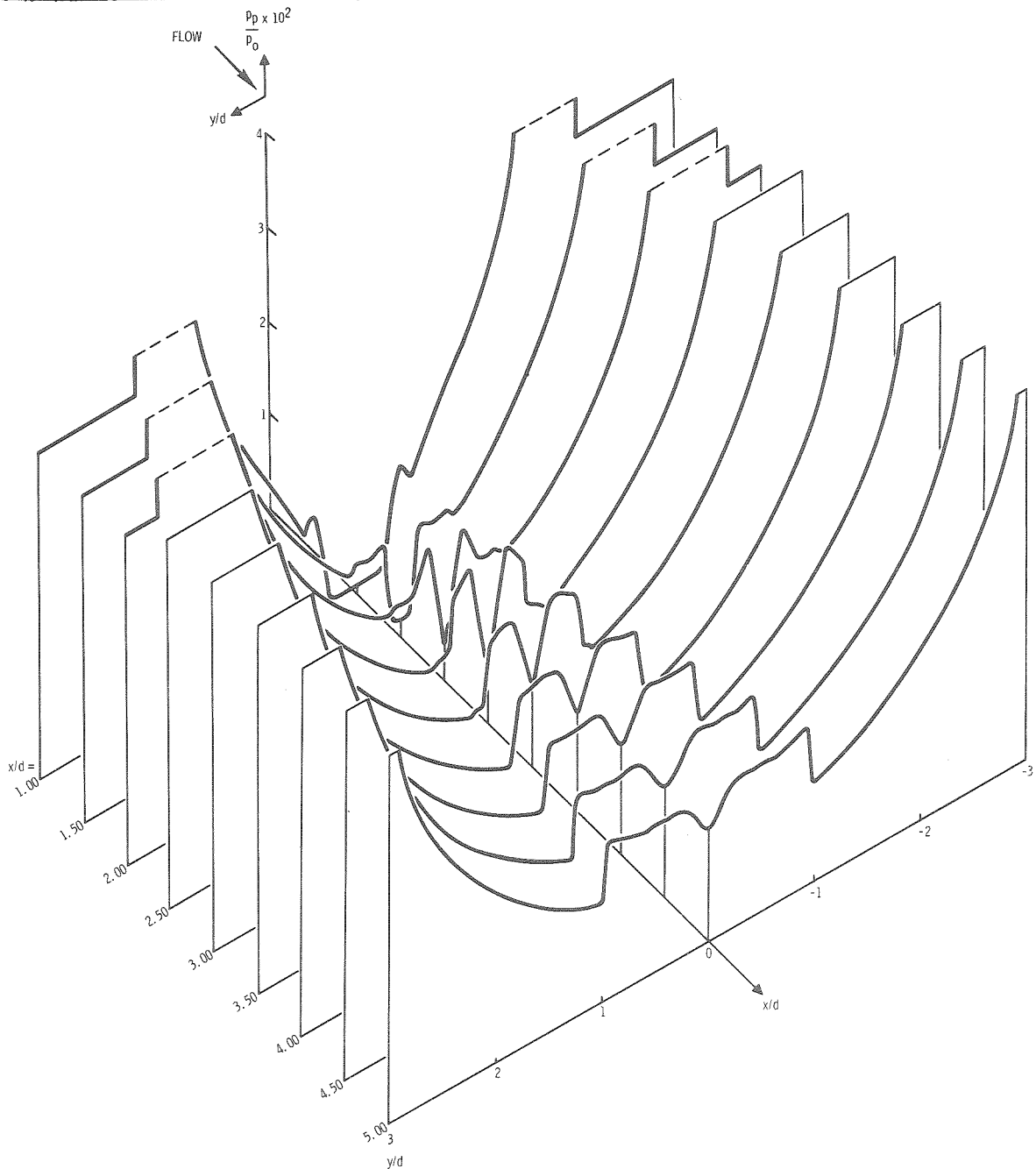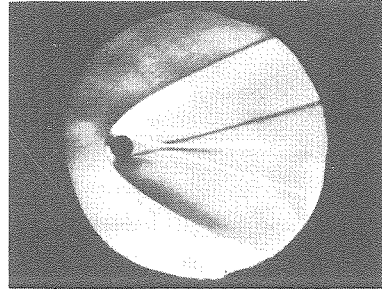
Figure 13.1a. Isoaxiometric Pitot-Pressure Traces

Model: d = 0.300 inch
p_{og} = 60.00 psig
P_{atm} = 74.53 cm Hg
T_O = 263°F
M_∞ = 5.71
Re_d = 49.4 x 10^3
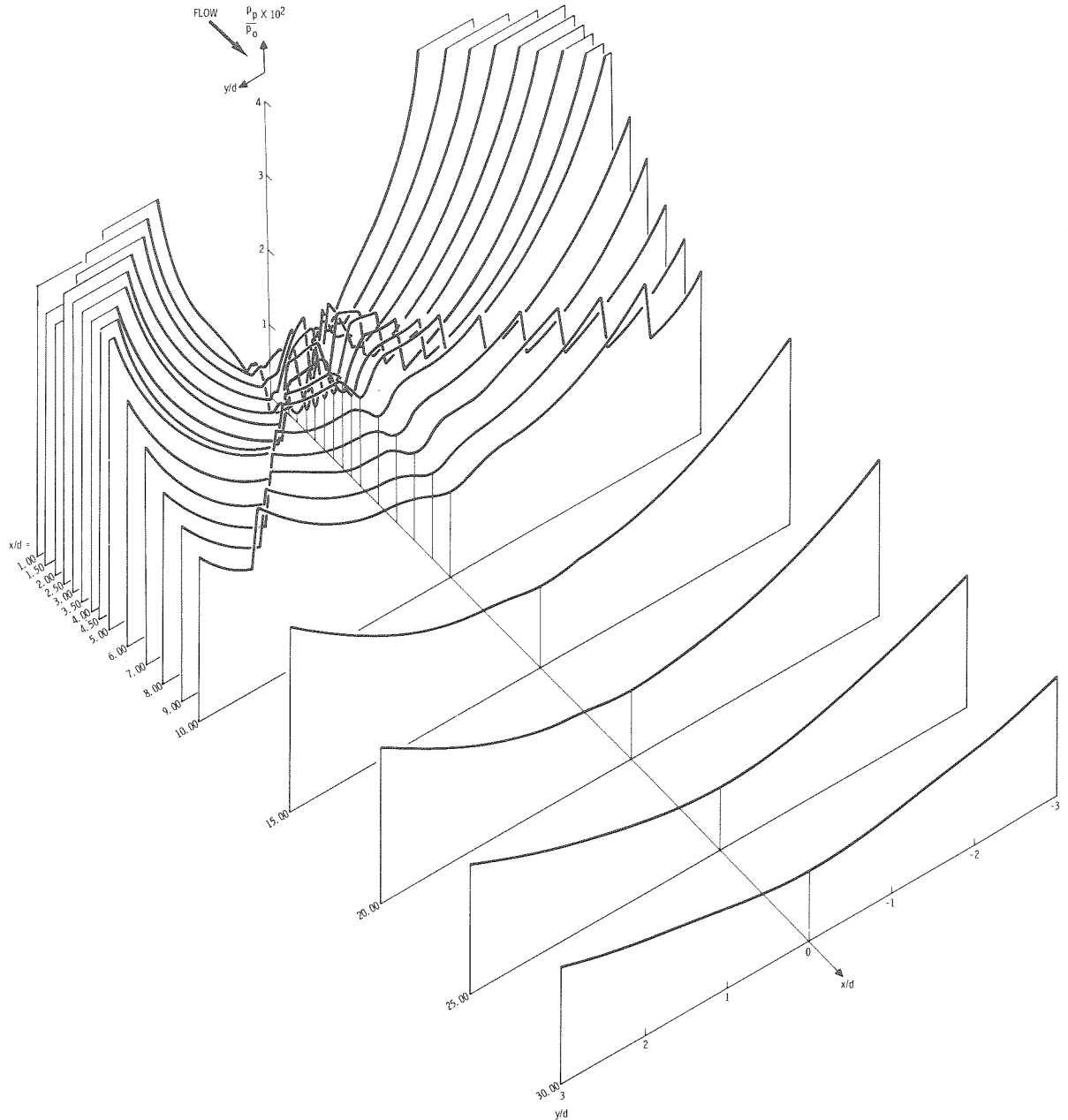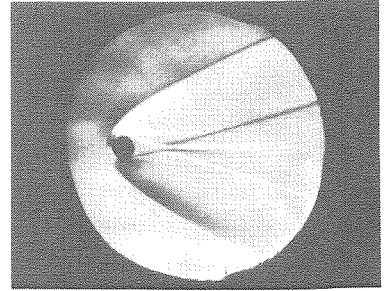
Figure 13.2. Isoaxiometric Pitot-Pressure Traces

Model: d = 0.300 inch
  pog = 60.00 psig
  patm = 74.53cm Hg
  t_0 = 263°F
  M_∞ = 5.71
  Re_d = 49.4 x 10^3

FLOW

$\frac{p_p \times 10^2}{p_0}$

y/d

4

3

2

1

x/d =
1.00
1.50
2.00
2.50
3.00
3.50
4.00
4.50
5.00

y/d

-3

-2

-1

0

1

2

3

x/d
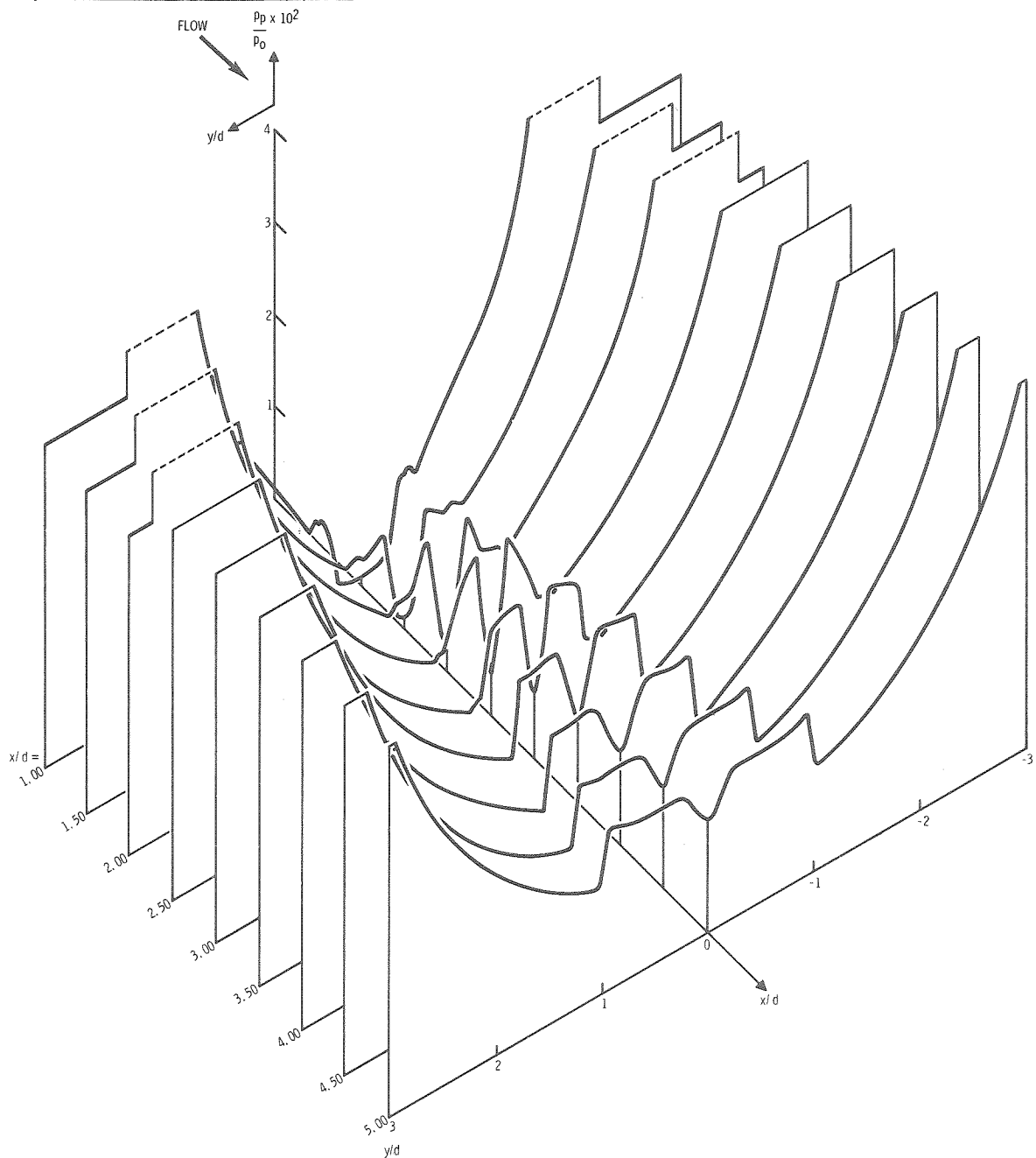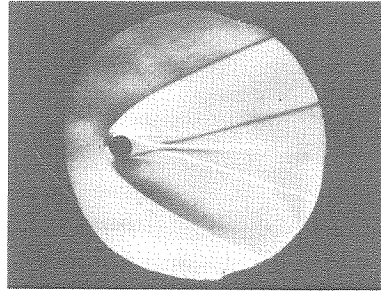
Figure 13.2a. Isoaxiometric Pitot-Pressure Traces

Model: d = 0.300 inch
p_{og} = 35.00 psig
p_{atm} = 74.33 cm Hg
T_0 = 262°F
M_∞ = 5.71
Re_d = 32.7 x 10^3
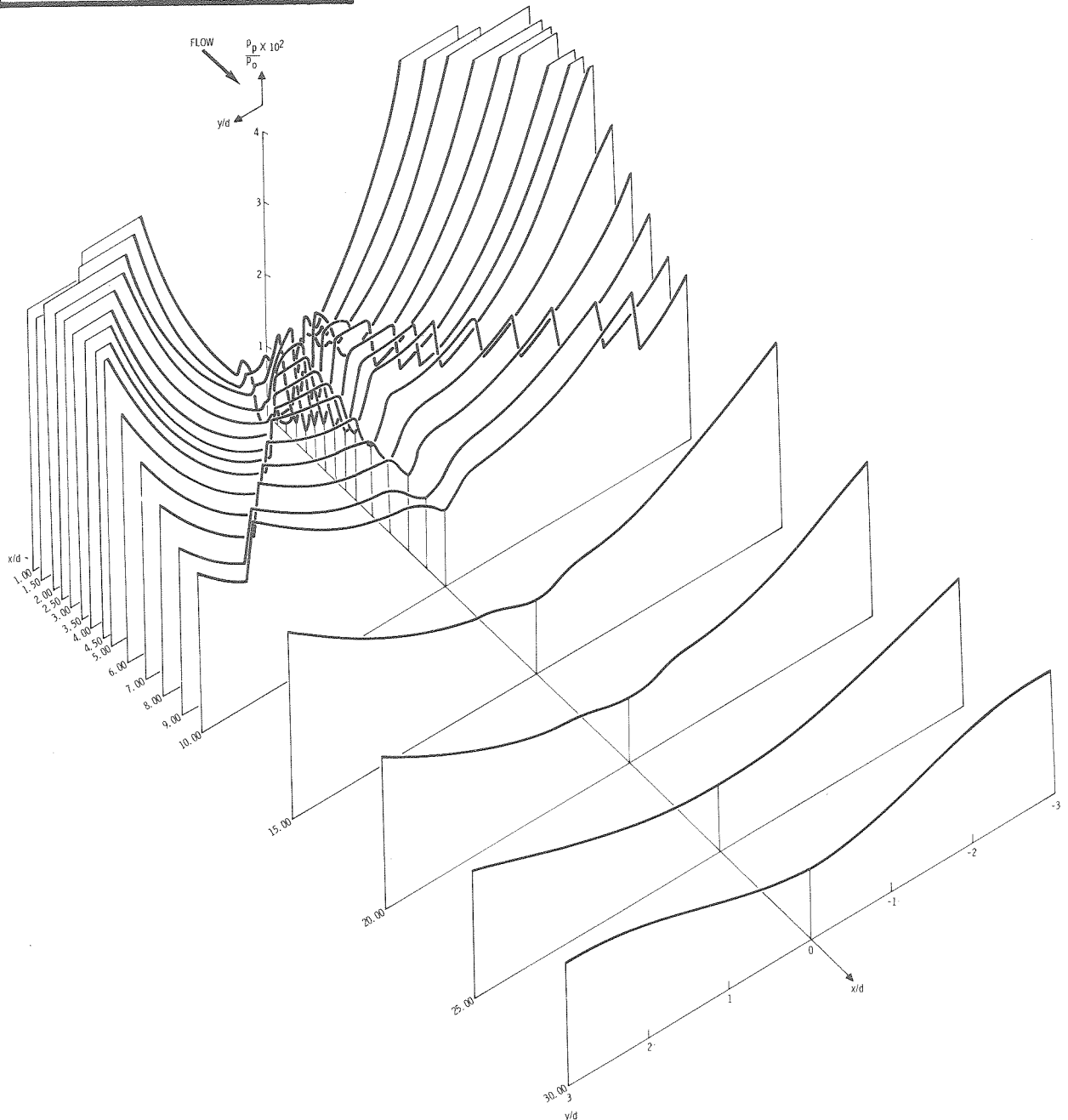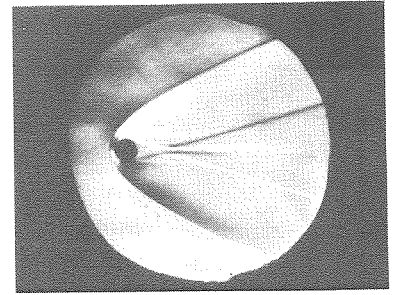
Figure 13.3. Isoaxiometric Pitot-Pressure Traces

Model: d = 0.300 inch
po_g = 35.00 psig
p_{atm} = 74.33 cm Hg
t_0 = 262°F
M_∞ = 5.71
Re_d = 32.7 x 10^3

FLOW

$\frac{p_p}{p_0} \times 10^2$

y/d

4

3

2

1

x/d = 1.00

1.50

2.00

2.50

3.00

3.50

4.00

4.50

5.00

y/d

x/d

-3

-2

-1

0

1

2

3
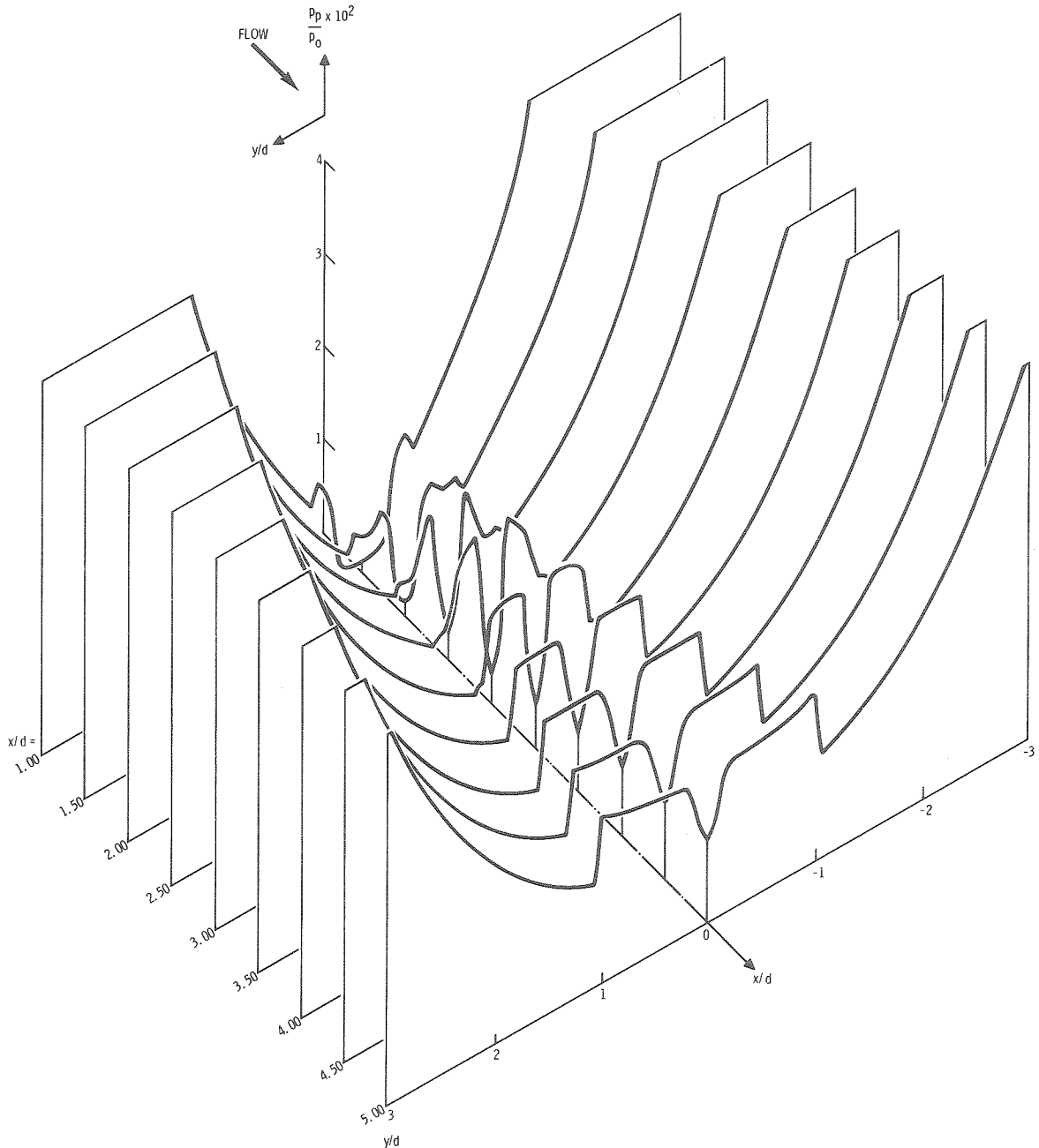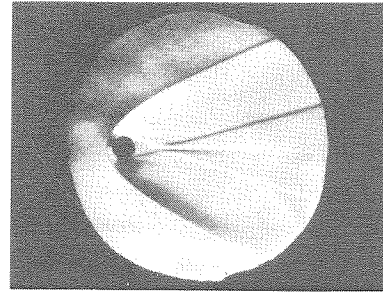
Figure 13.3a. Isoaxiometric Pitot-Pressure Traces

Model: d = 0.300 inch
p_{og} = 10.00 psig
p_{atm} = 74.36 cm Hg
T_0 = 262°F
M_∞ = 5.64
Re_d = 16.7 x 10^3

FLOW

$\frac{P_p}{P_o}$ X 10^2
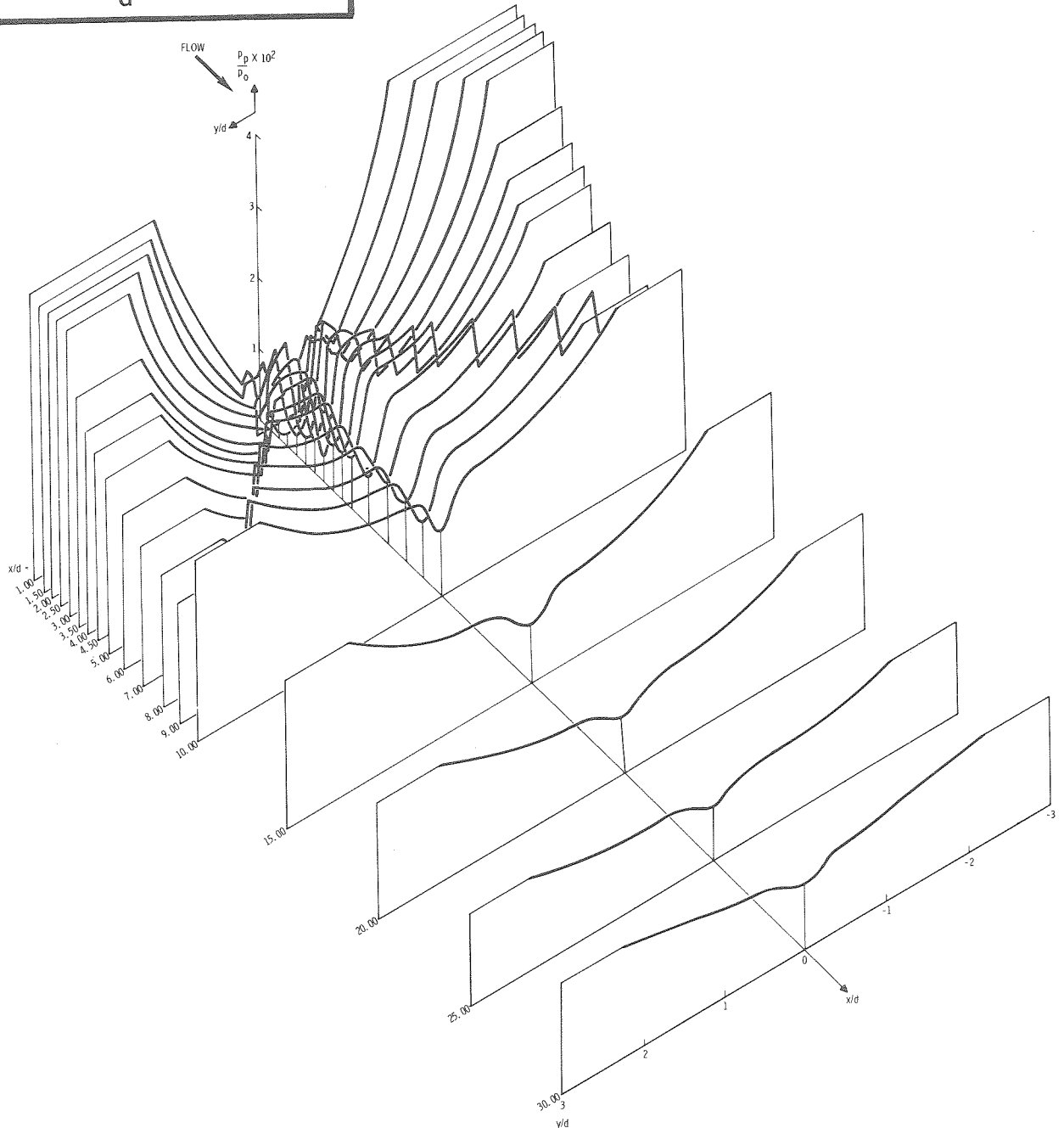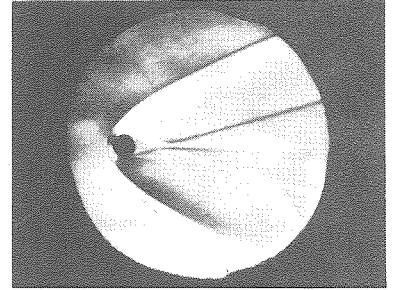
Figure 13.4. Isoaxiometric Pitot-Pressure Traces

Model: d = 0.300 inch
po$_g$ = 10.00 psig
patm = 74.36 cm Hg
t$_0$ = 262°F
M$_\infty$ = 5.64
Re$_d$ = 16.7 x 10^3

FLOW

$\frac{p_p}{p_0}$ x 10^2

y/d

x/d =
1.00
1.50
2.00
2.50
3.00
3.50
4.00
4.50
5.00

x/d

y/d
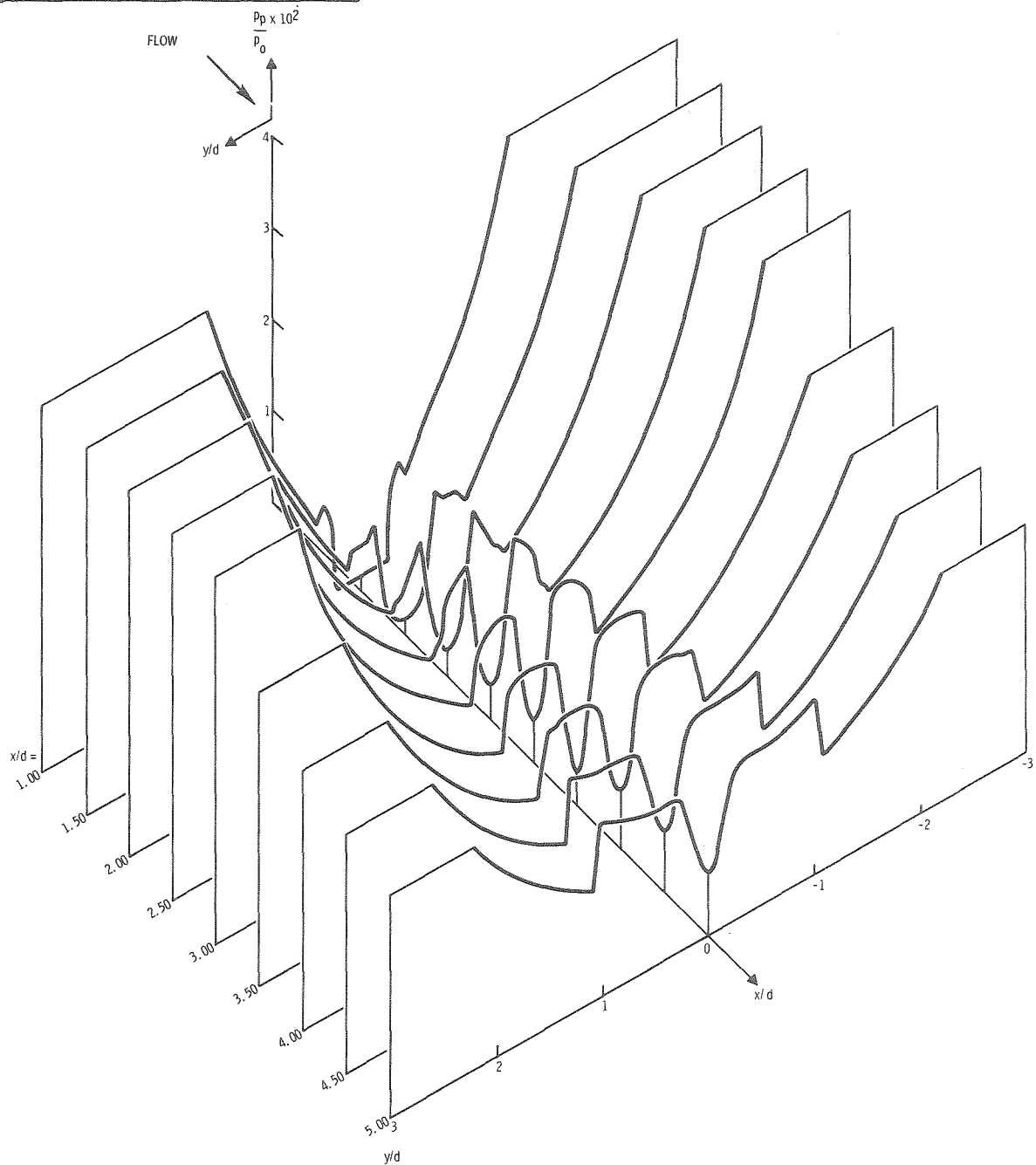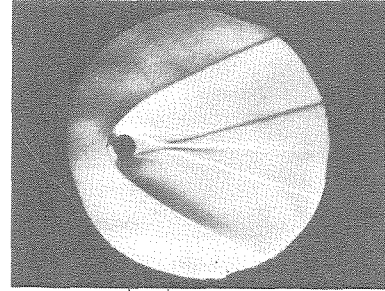
Figure 13.4a. Isoaxiometric Pitot-Pressure Traces

Model: d = 0.200 inch
p_{og} = 96.68 psig
p_{atm} = 74.44 cm Hg
T_0 = 264°F
M_∞ = 5.69
Re_d = 49.3 x 10³

FLOW
$\frac{p_p}{p_0} \times 10^2$
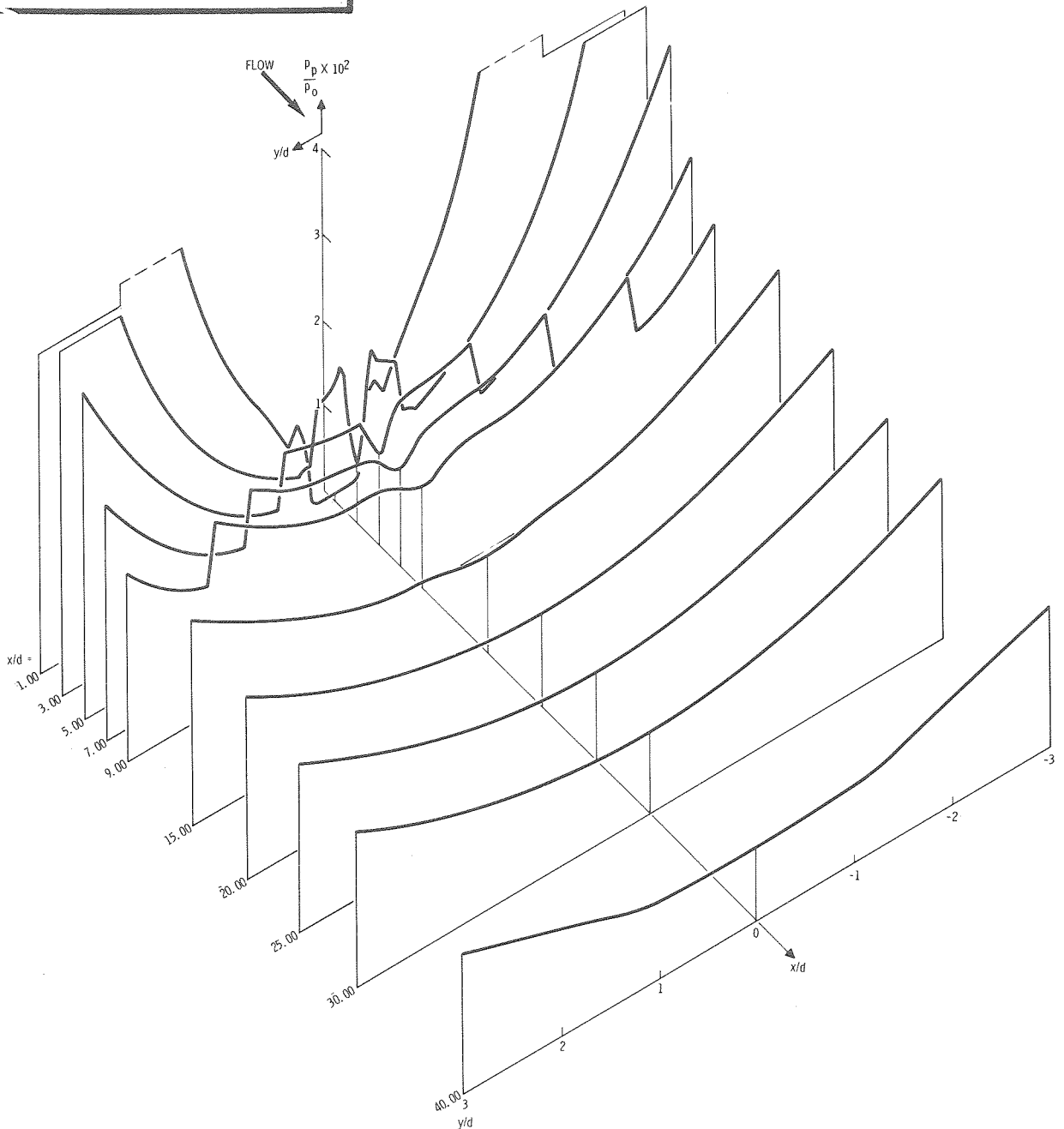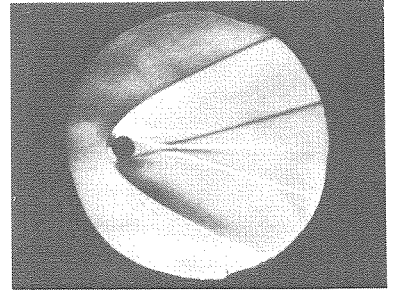
Figure 13.5. Isoaxiometric Pitot-Pressure Traces

Model: d = 0.200 inch
p_{og} = 59.48 psig
p_{atm} = 74.67 cm Hg
T_0 = 263°F
M_∞ = 5.71
Re_d = 32.7 x 10^3

FLOW

$\frac{p_p}{p_0}$ X 10^2

y/d

4

3

2

1

x/d =
1.00
3.00
5.00
7.00
9.00
15.00
20.00
25.00
30.00
40.00

-3
-2
-1
0
1
2
3

x/d

y/d
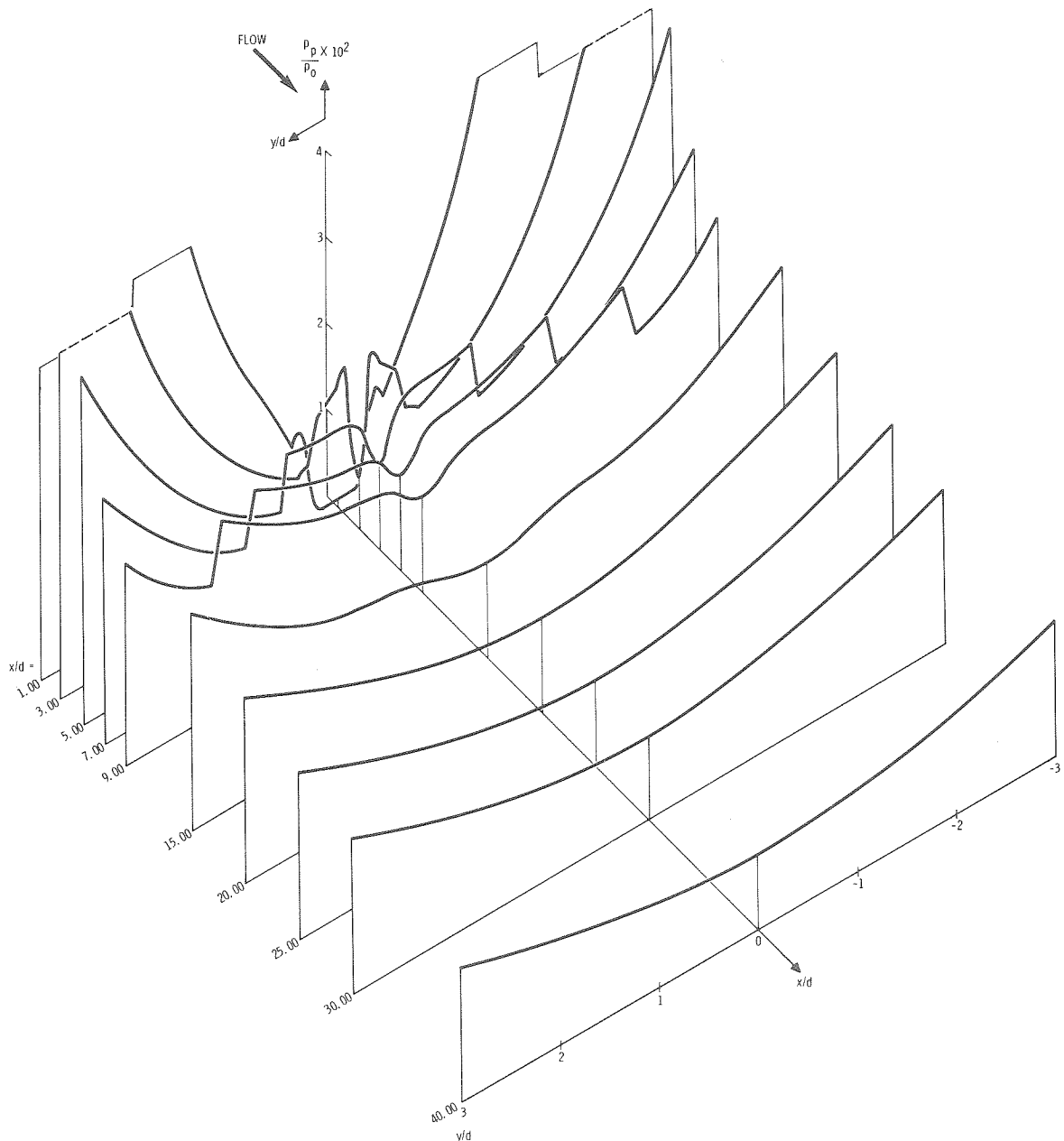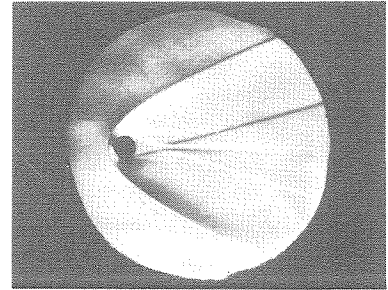
Figure 13.6. Isoaxiometric Pitot-Pressure Traces

Model: d = 0.200 inch
p_{og} = 22.48 psig
p_{atm} = 74.57 cm Hg
T_o = 262°F
M^∞ = 5.68
Re_d = 16.6 x 10^3

FLOW

$\frac{p_p \times 10^2}{p_o}$

y/d

x/d =
1.00
3.00
5.00
7.00
9.00
15.00
20.00
25.00
30.00
40.00

x/d

y/d
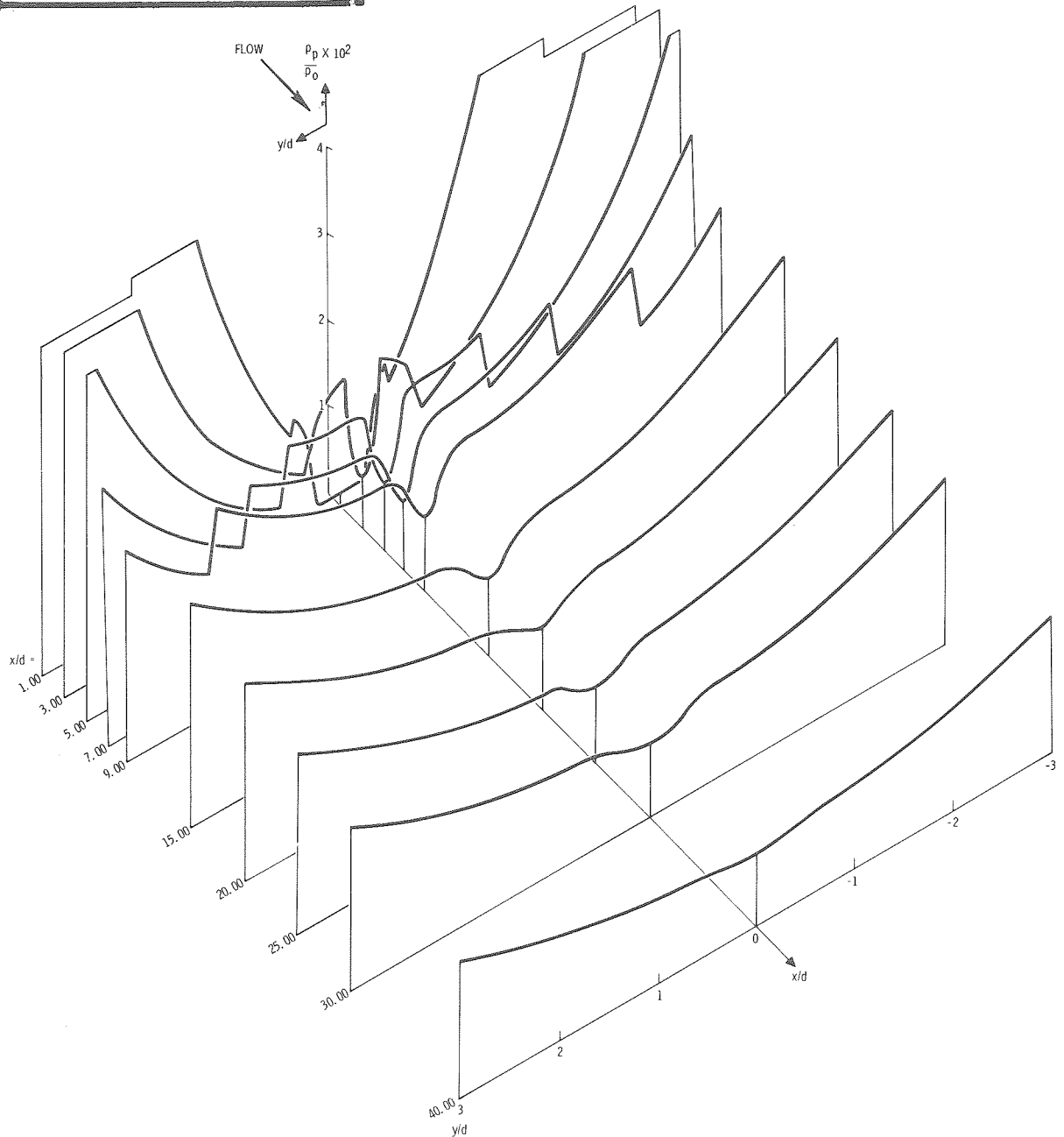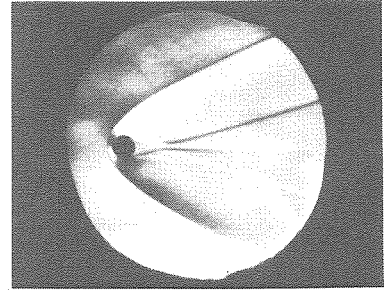
Figure 13.7. Isoaxiometric Pitot-Pressure Traces

Model: d = 0. 200 inch

p_{og} = 3. 80 psig

p_{atm} = 74. 69 cm Hg

T_0 = 260°F

M_∞ = 5. 58

Re_d = 8.58 x 10^3

FLOW $\frac{p_p \times 10^2}{p_o}$

y/d

x/d =
1.00
3.00
5.00
7.00
9.00
15.00
20.00
25.00
30.00
40.00

x/d

y/d
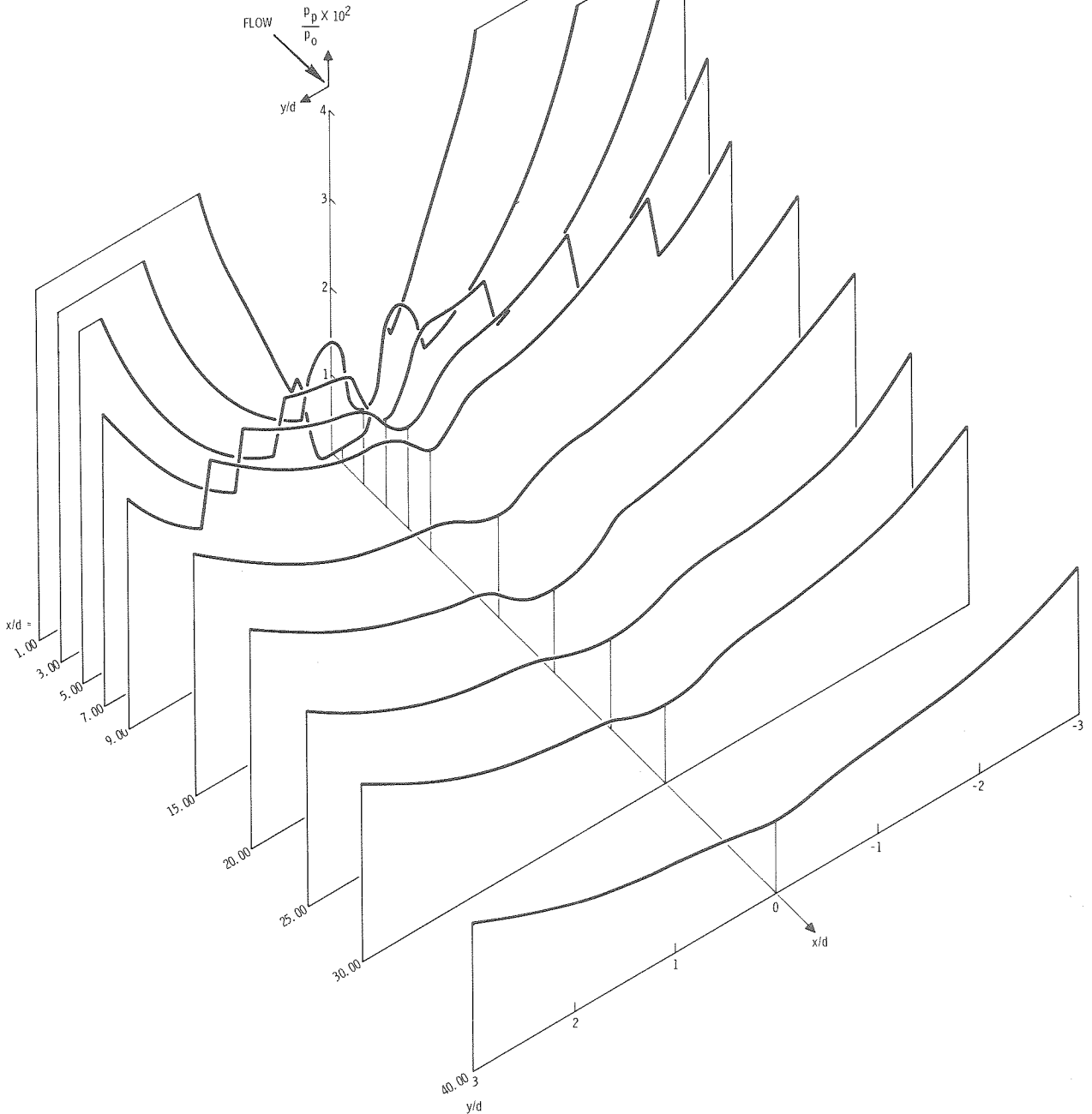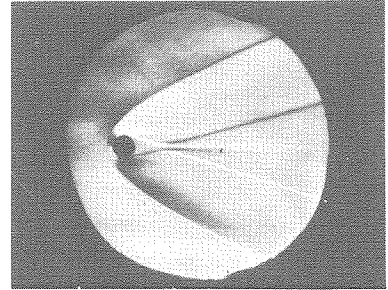
Figure 13.8.   Isoaxiometric Pitot-Pressure Traces

Model: d = 0.100 inch
p_{og} = 59.42 psig
p_{atm} = 74.54 cm Hg
T_0 = 263°F
M_∞ = 5.71
Re_d = 16.3 x 10^3
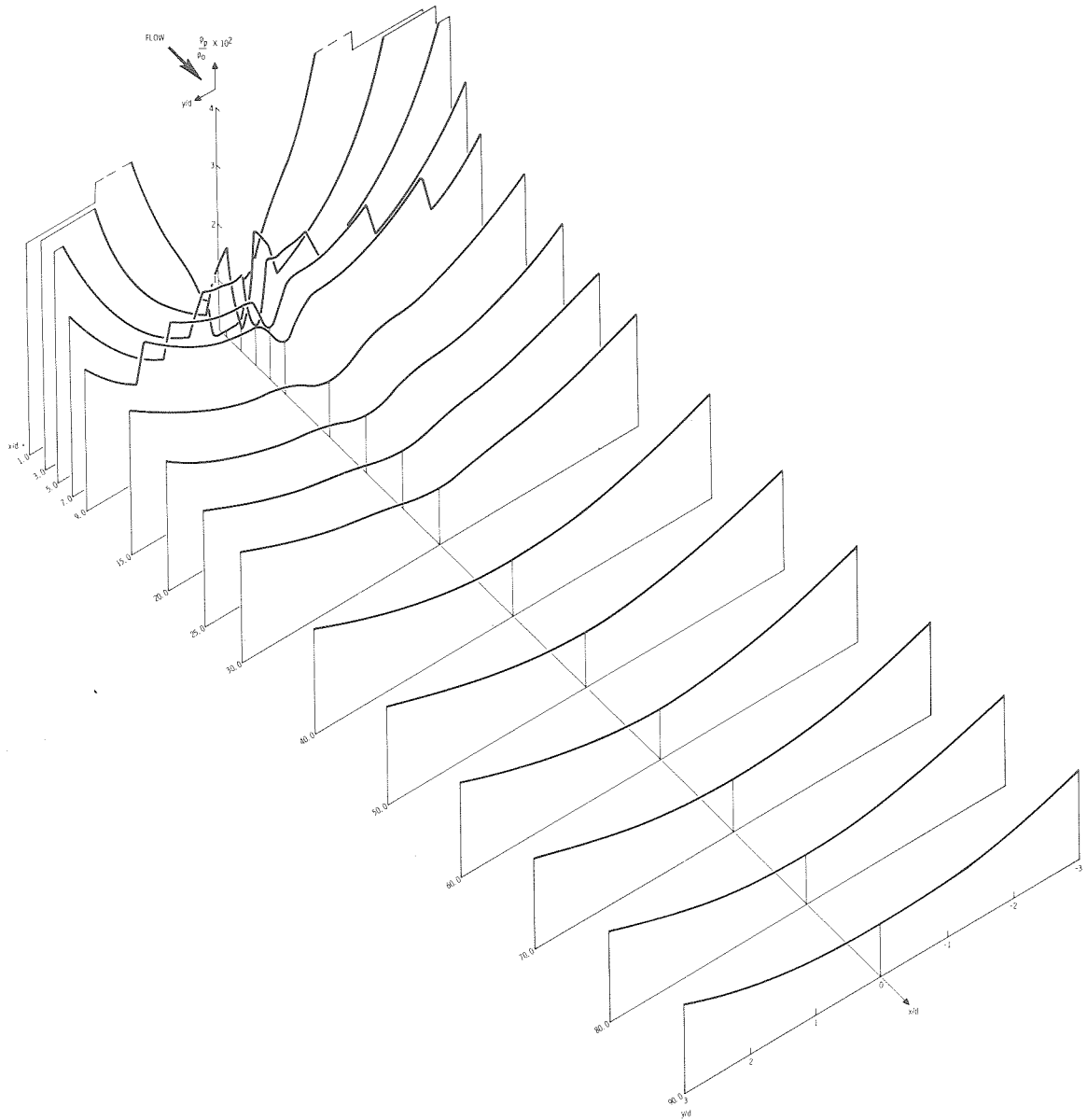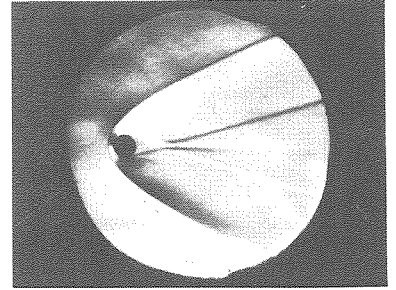
Figure 13.9. Isoaxiometric Pitot-Pressure Traces

Model: d = 0.100 inch
p_{og} = 59.42 psig
p_{atm} = 74.54 cm Hg
T_o = 263°F
M_∞ = 5.71
Re_d = 16.3 x 10^3
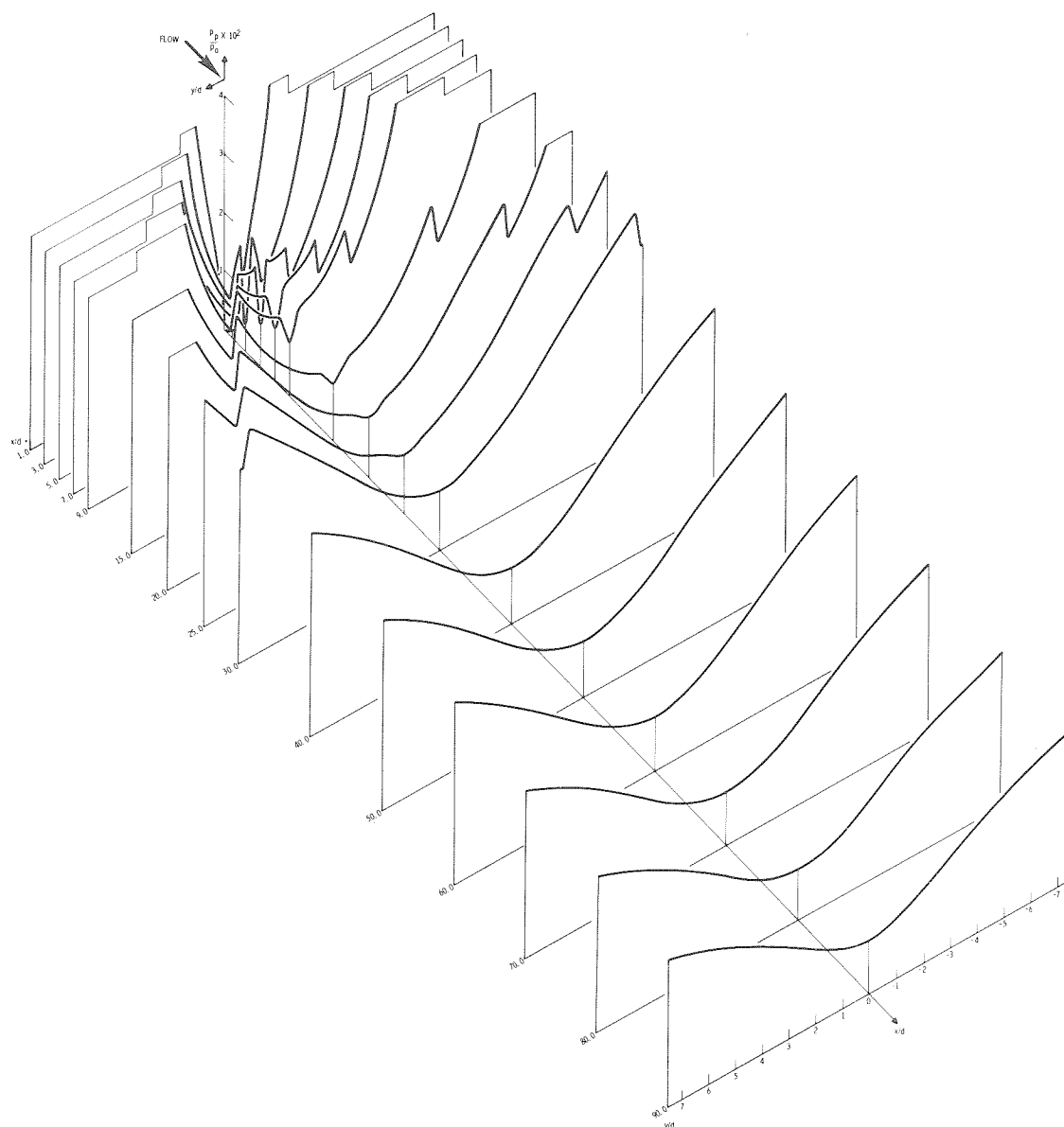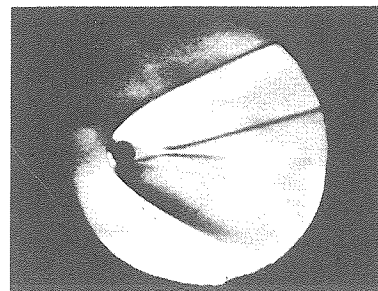
Figure 13.9a. Isoaxiometric Pitot-Pressure Traces

Model: d = 0.100 inch
p_{og} = 22.54 psig
p_{atm} = 74.56 cm Hg
T_0 = 262°F
M_∞ = 5.68
Re_d = 8.28 x 10^3
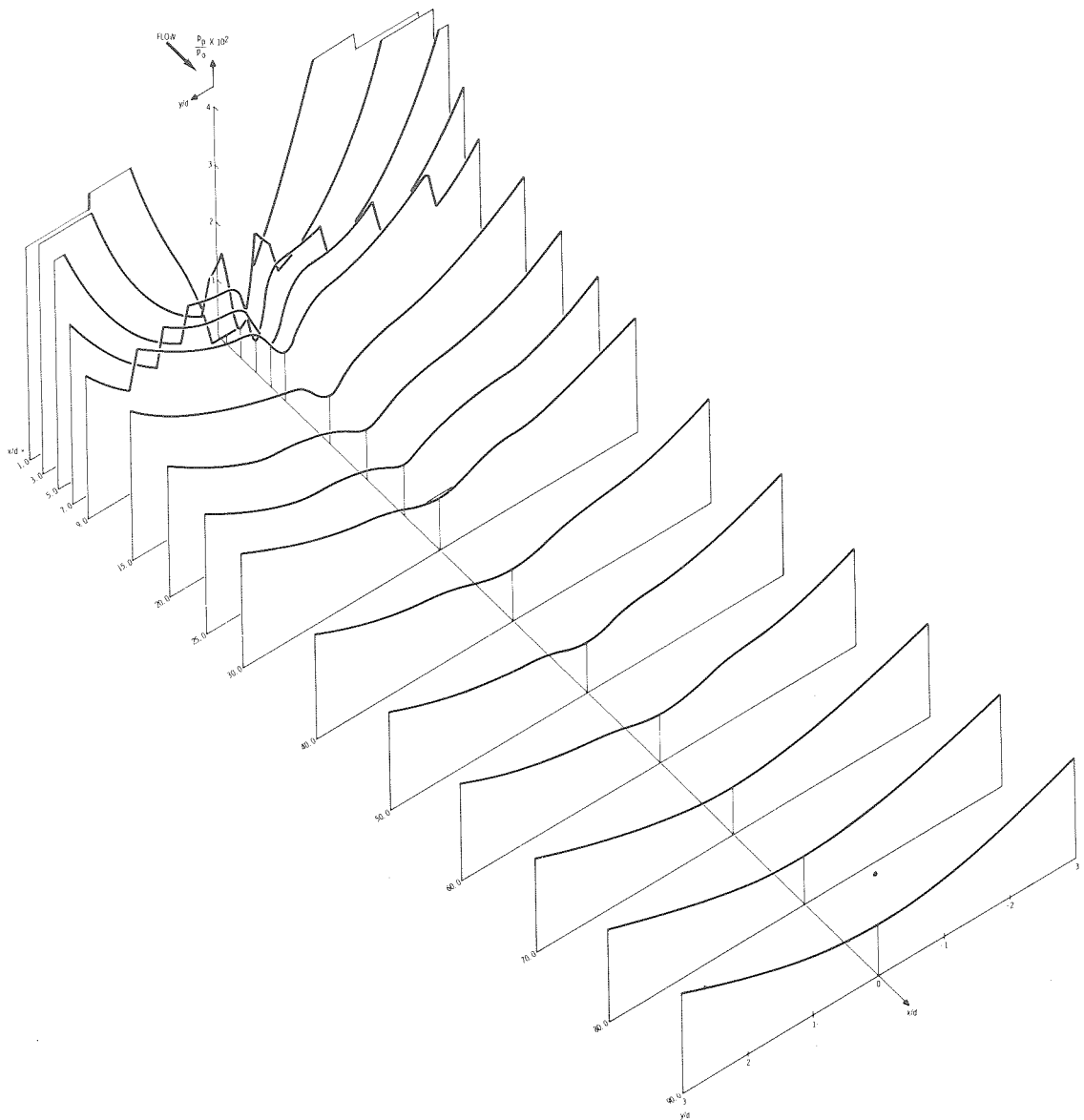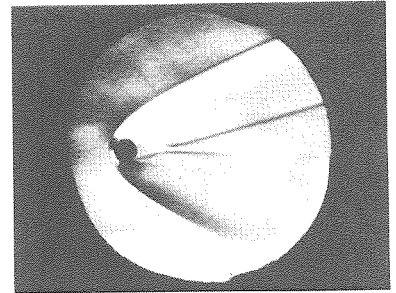
Figure 13.10.   Isoaxiometric Pitot-Pressure Traces

Model: d = 0.100 inch
P_{og} = 22.54 psig
P_{atm} = 74.56 cm Hg
T_{-} = 262°F
M_{∞} = 5.68
Re_d = 8.28 x 10³
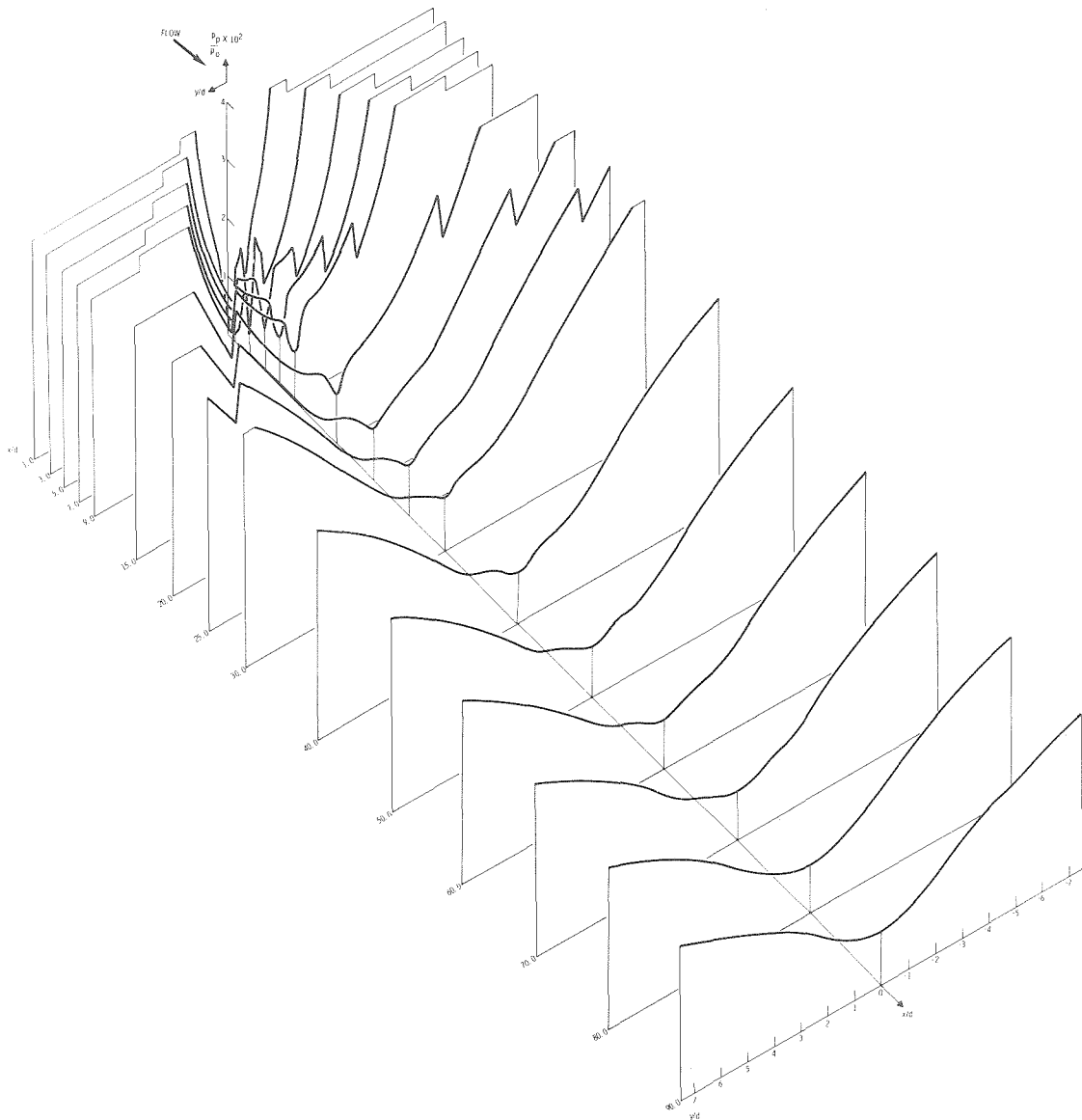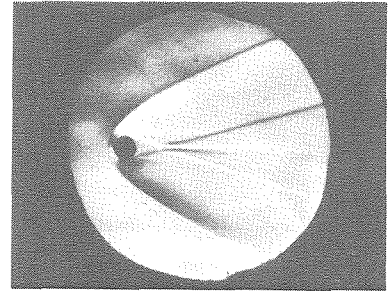
Figure 13.10a. Isoaxiometric Pitot-Pressure Traces

Model: d = 0.100 inch
p_{og} = 3.84 psig
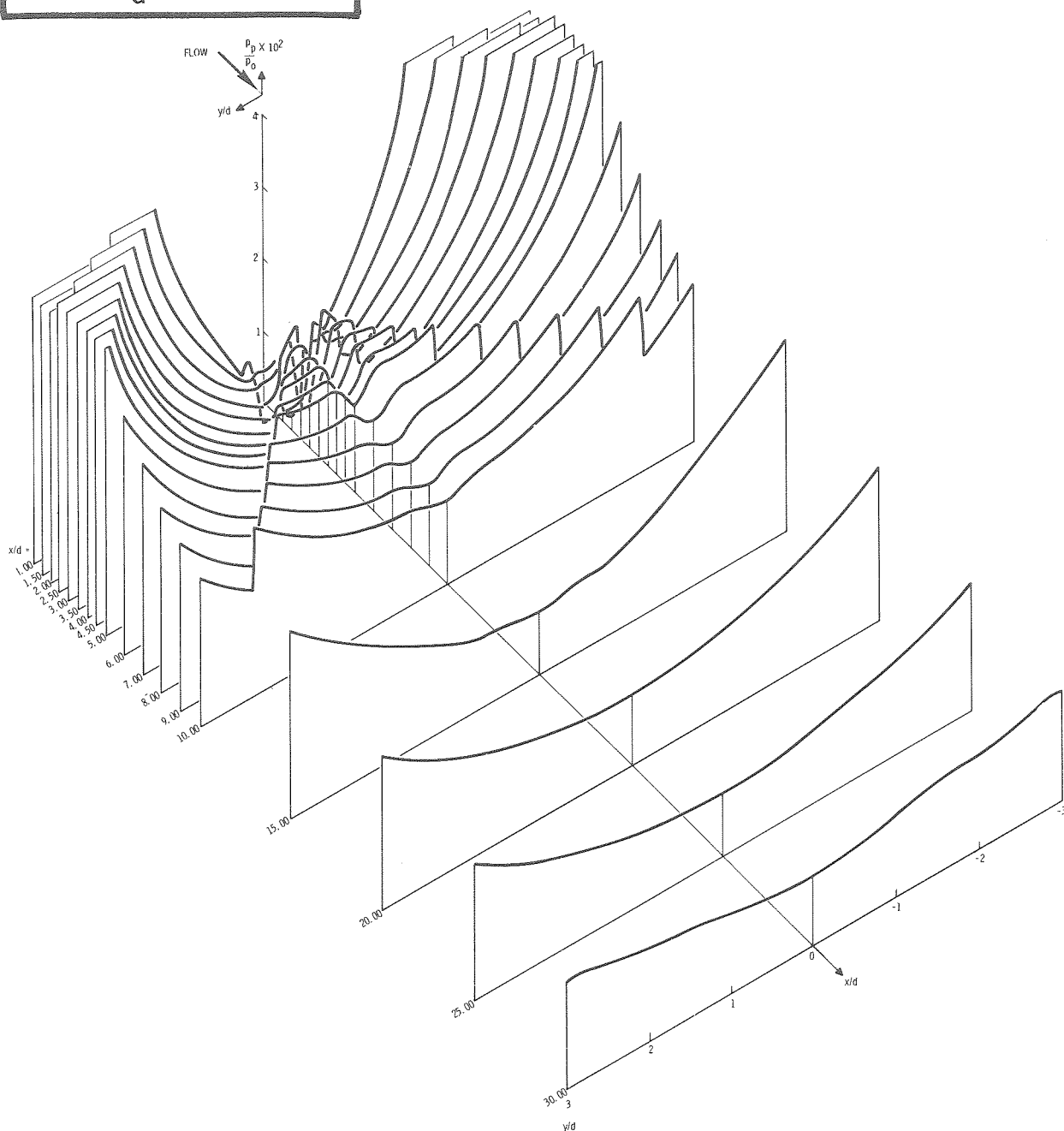p_{atm} = 74.71 cm Hg
T_0 = 260°F
M_∞ = 5.58
Re_d = 4.29 x 10³
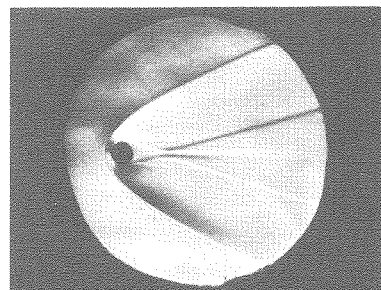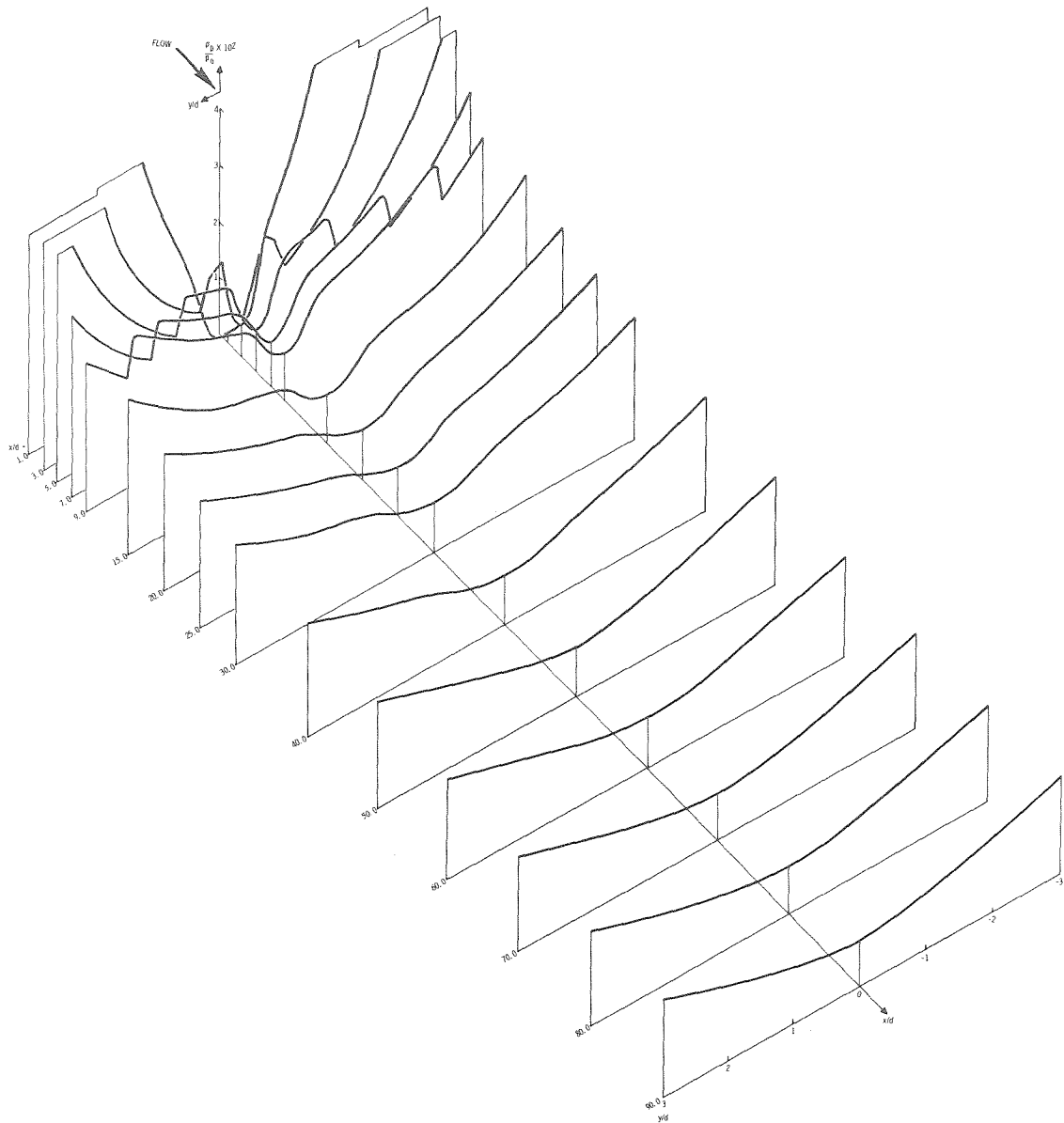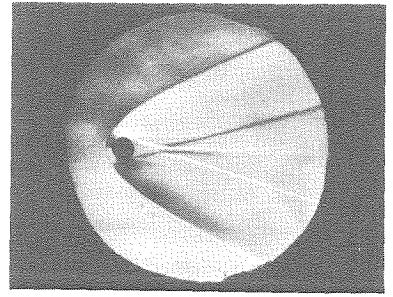

Figure 13.11. Isoaxisometric Pitot-Pressure Traces

Model: d = 0.100 inch
p_{og} = 3.84 psig
p_{atm} = 74.71 cm Hg
T_0 = 260°F
M_∞ = 5.58
Re_d = 4.29 x 10^3
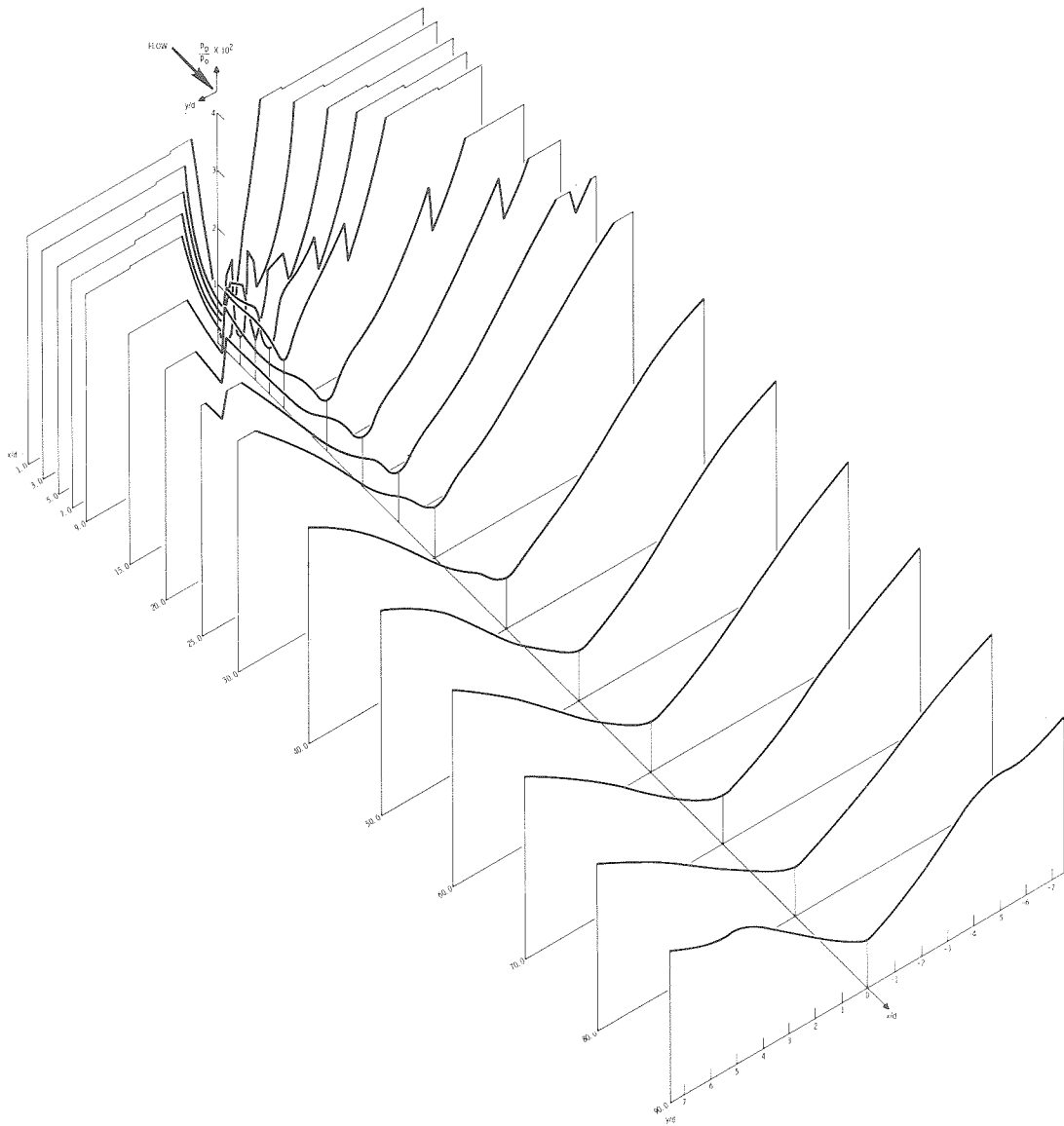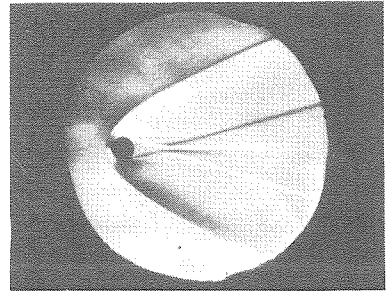
Figure 13.11a. Isoaxiometric Pitot-Pressure Traces
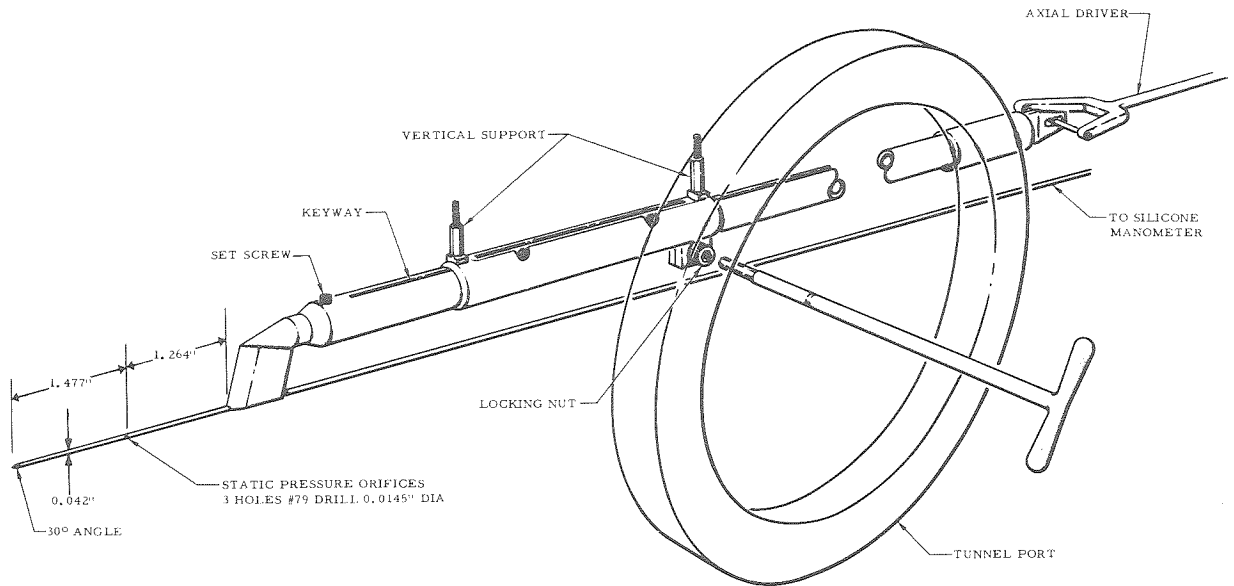
Figure 14.   Static-Pressure Probe

was designed to prevent two occurrences: the loss of silicone into the wind

tunnel and the entry of atmospheric air into the pressure-recording system.

To evacuate the entire system, two 1-hp vacuum pumps were operated

constantly for several weeks before recording final data.   The reference

pressure on the transducer was maintained at about 4.0 microns of

mercury; it was measured by a conventional Stokes gauge equipped with a

liquid-nitrogen cold trap.   As with the pitot-pressure measurements, the

static-pressure recording system was calibrated by varying the stagnation

pressure of the wind tunnel over a wide range.   The electronic circuitry

shown in Figures 7 and 8 was also used for the static-pressure recording
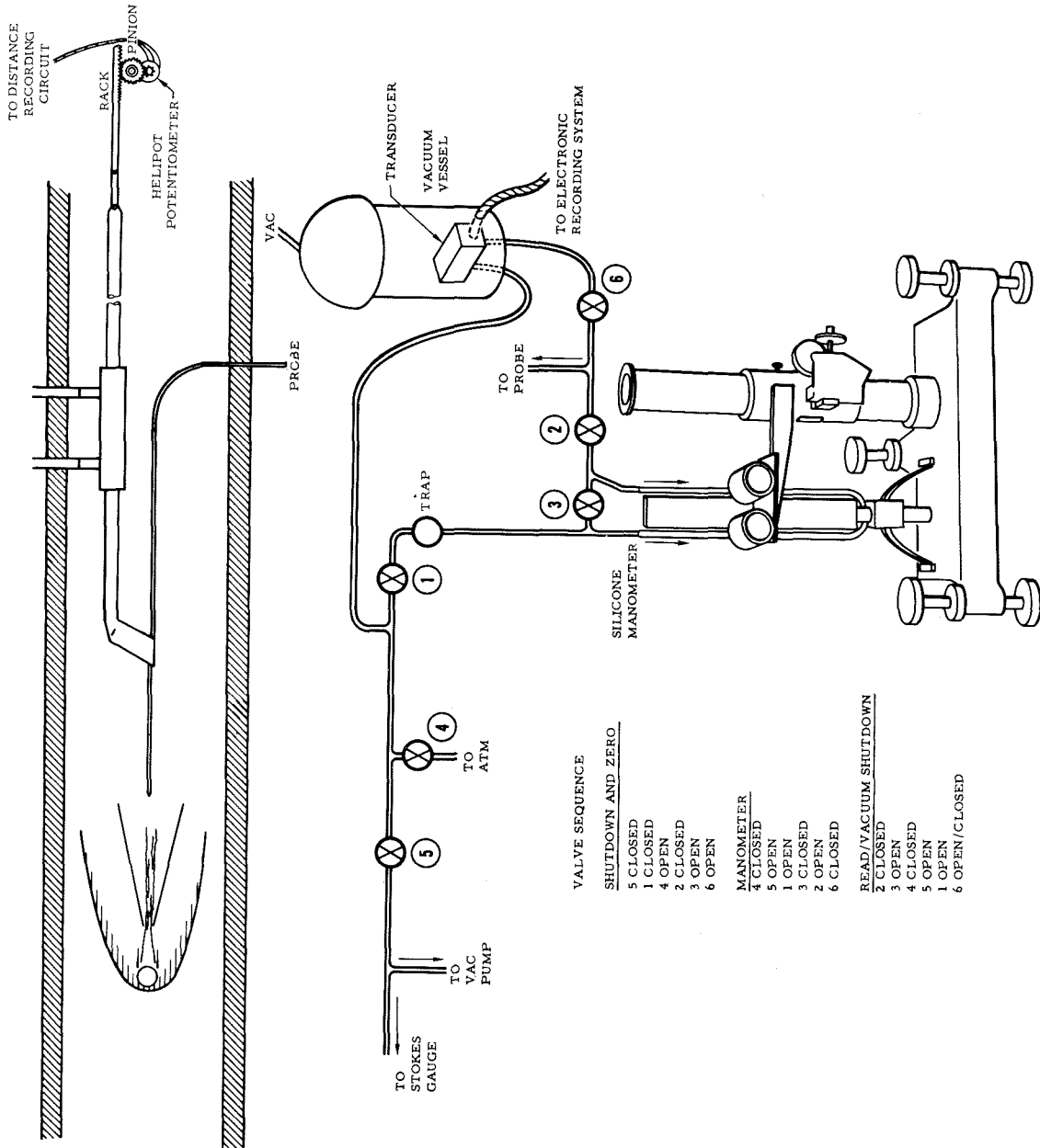
system.

Figure 15. Static-Pressure Recording System

To establish the fact that the pressure was constant across the wake, as expected from theory (discussed in Section VI of this thesis), several vertical static-pressure surveys were made for various-sized cylinders at different axial locations. A typical vertical static-pressure survey is shown in Figure 16. It should be noted that the static pressure is constant across the wake and almost constant up to the trailing shock.

To test the two-dimensionality of the flow field behind the cylindrical rod, the apparatus shown in Figure 17 was designed. Here, a conventional lathe bed was used to drive a static-pressure probe horizontally. Again, distances were converted to voltages by the electronic circuitry shown in Figures 7 and 8. Typical horizontal static-pressure traces are shown in Figure 18. Several trace surveys were made at various axial positions

The graph shows $\left(\frac{P}{P_o}\right) \times 10^3$ on the vertical axis plotted against y/d on the horizontal axis.

Conditions noted on the figure:

$d = 0.300$ IN.
$x/d = 15.00$
$P_{o_g} = 85.00$ PSIG
$P_{atm} = 74.13$ CM Hg
$T_o = 263°$ F
$Re_d = 65.0 \times 10^3$

down ← | → up
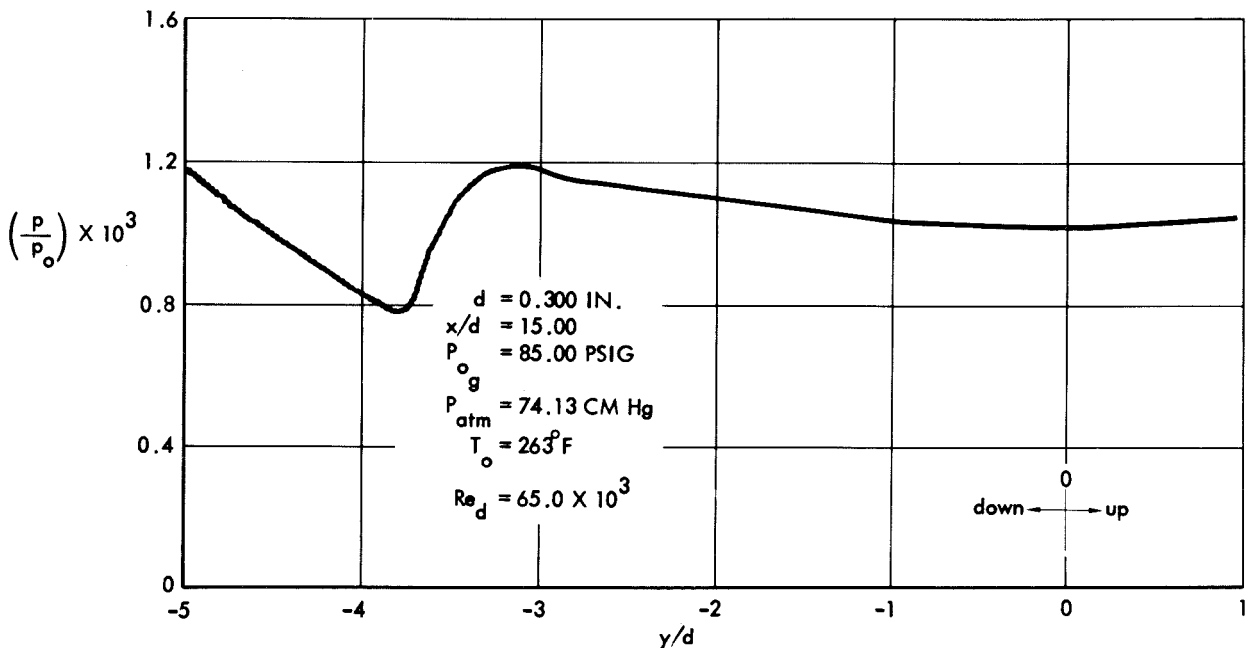
Figure 16. Typical Vertical Static-Pressure Survey
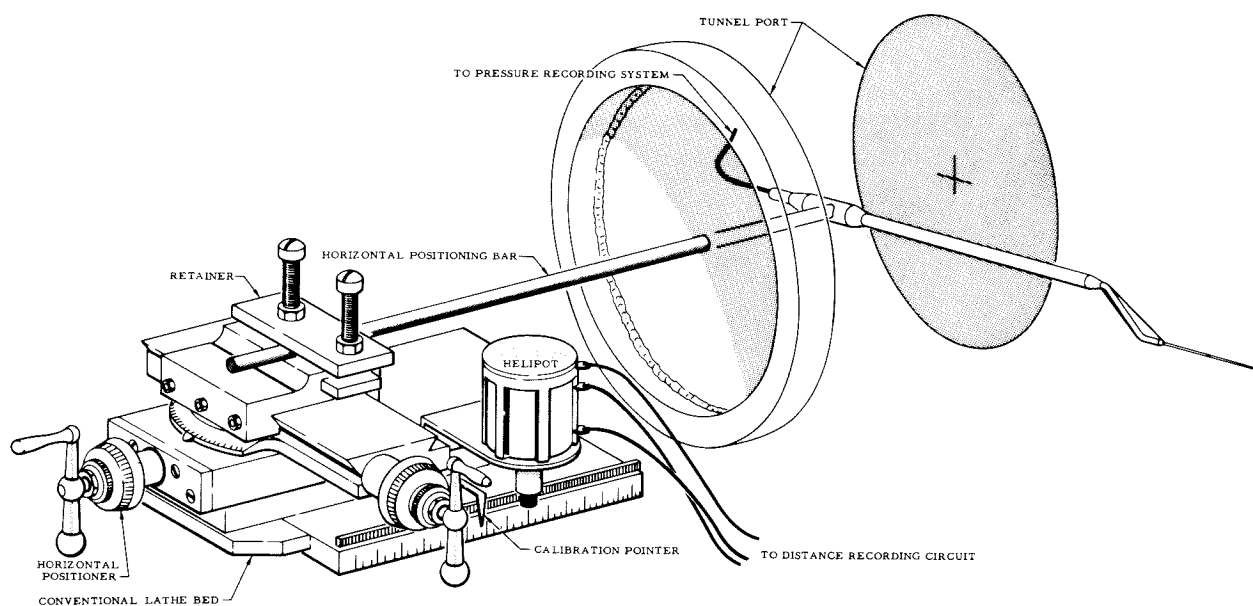
Figure 17. Horizontal Traversing Mechanism for Static-Pressure Probe

downstream of the 0.300 and 0.100-inch models. These surveys revealed

that a disturbance originated ahead of the intersection of the model with

the side walls of the wind tunnel. As a result of these tests, the limits of

two-dimensional flow (Figure 19) were identified. As noted, the distance

L_{2-D}, was a function of model size and wind tunnel stagnation pressure

(Figure 21).

As with the pitot-pressure probe, the angle-of-attack sensitivity of

the static-pressure probe was obtained through use of the mechanism

shown in Figure 11. The results of this experiment are shown in

Figure 20. Unlike the pitot-pressure measurements, however, the flow

inclination around the static-pressure probe is very nearly zero; therefore,

MODEL: d = 0.100 IN.
x = 2.00 IN.
P_{o_g} = 59.42 PSIG
P_{atm} = 73.84 CM Hg
T_o = 263°F

$\left(\dfrac{P}{P_o}\right) \times 10^3$

RIGHT ← | → LEFT (LOOKING UPSTREAM)
0
(CENTERLINE)
z-INCHES   z-INCHES

(a) 2.00 Inch Downstream Station

MODEL: d = 0.100"
x = 3.50"
P_{o_g} = 59.42 PSIG
P_{atm} = 73.82 cm Hg
T_o = 263° F

$(p/P_o) \times 10^3$

RIGHT ← | → LEFT (LOOKING UPSTREAM)
0
(CENTERLINE)
z-INCHES   z-INCHES
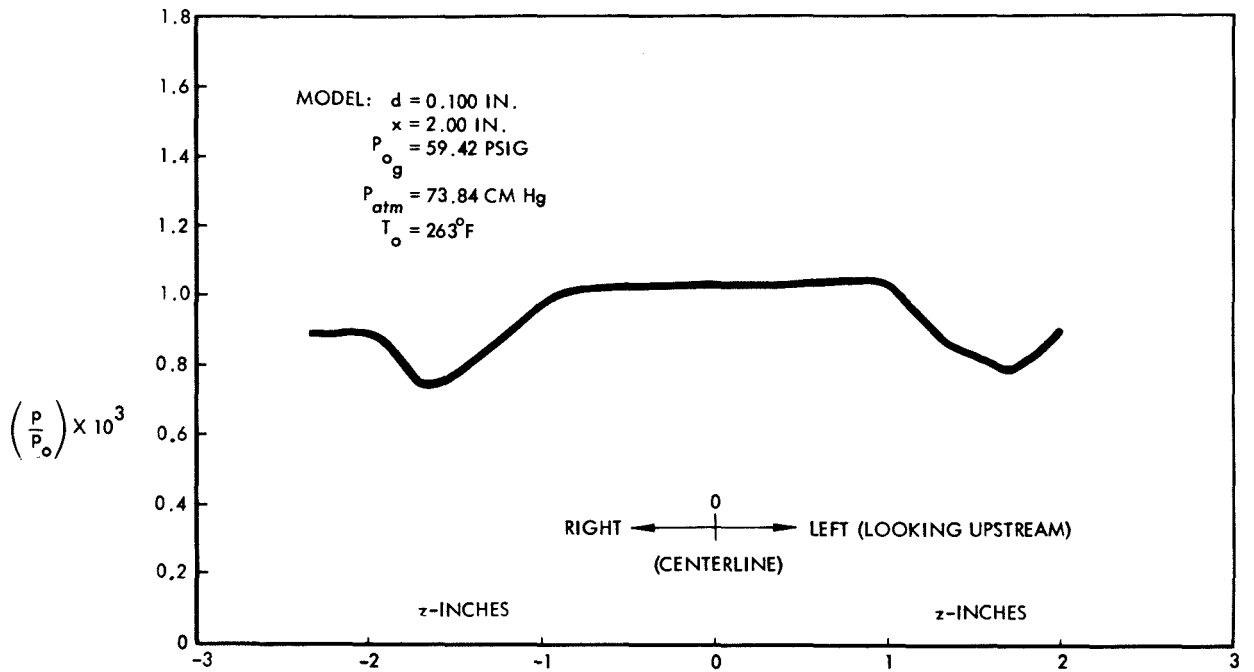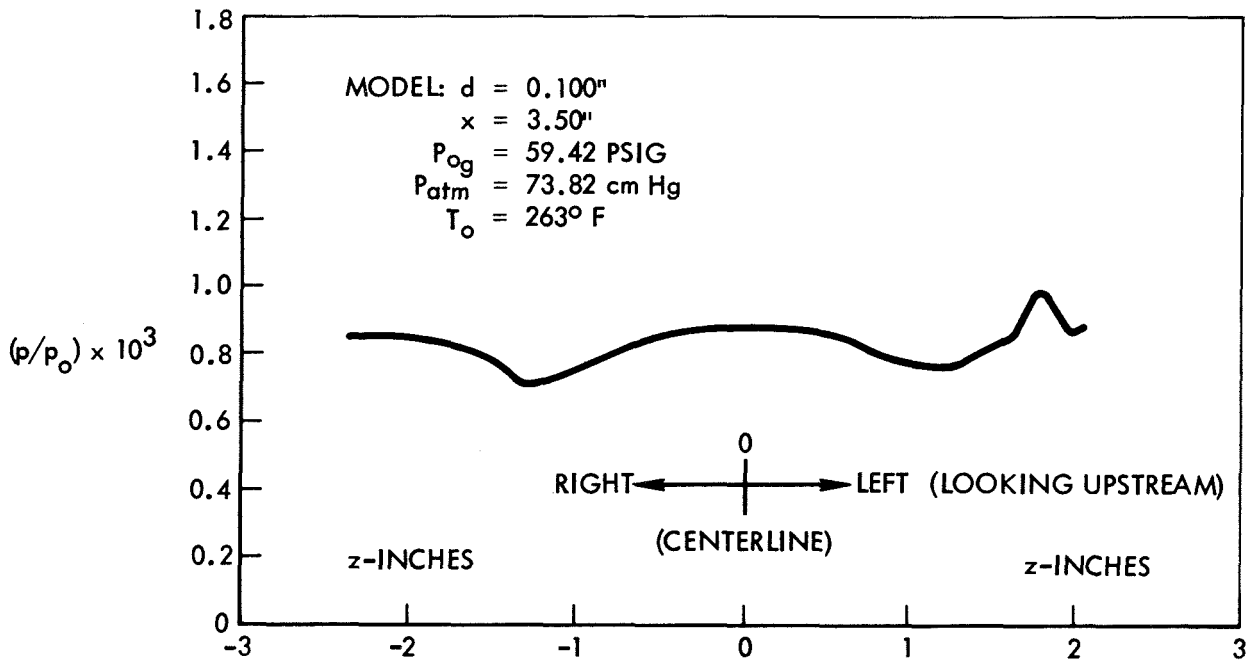
(b) 3.50 Inch Downstream Station

Figure 18. Typical Horizontal Static-Pressure Survey
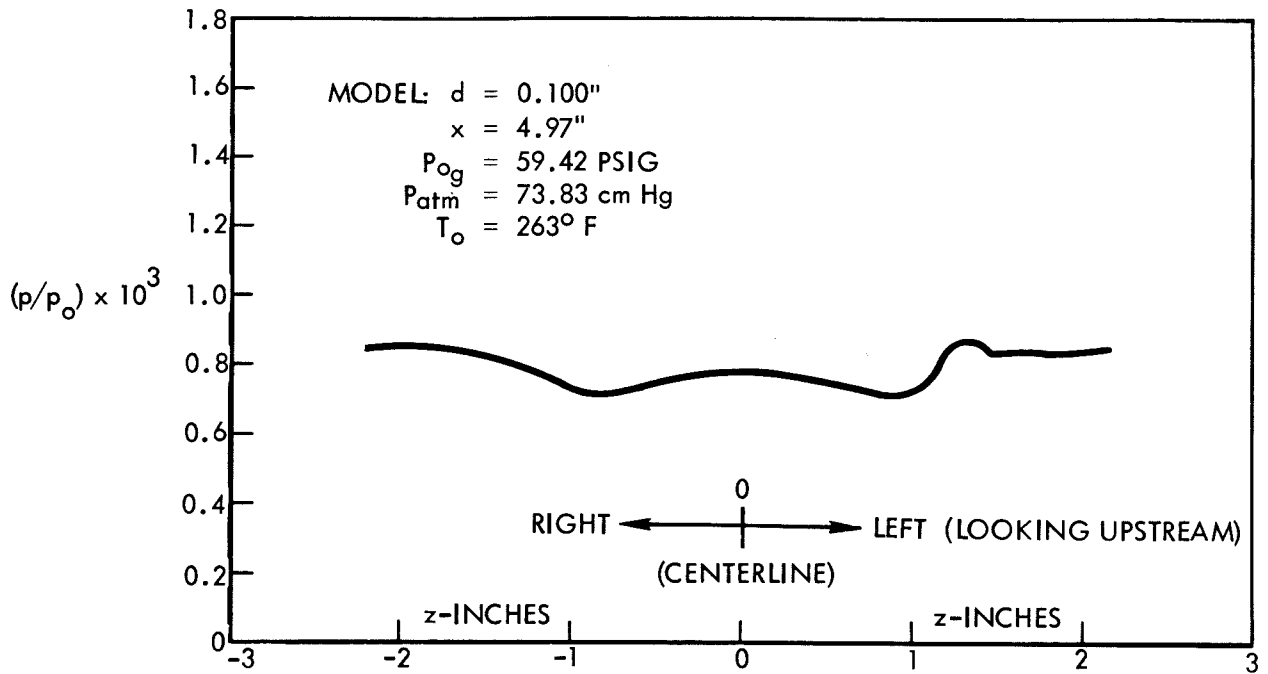
(c) 4. 97 Inch Downstream Station
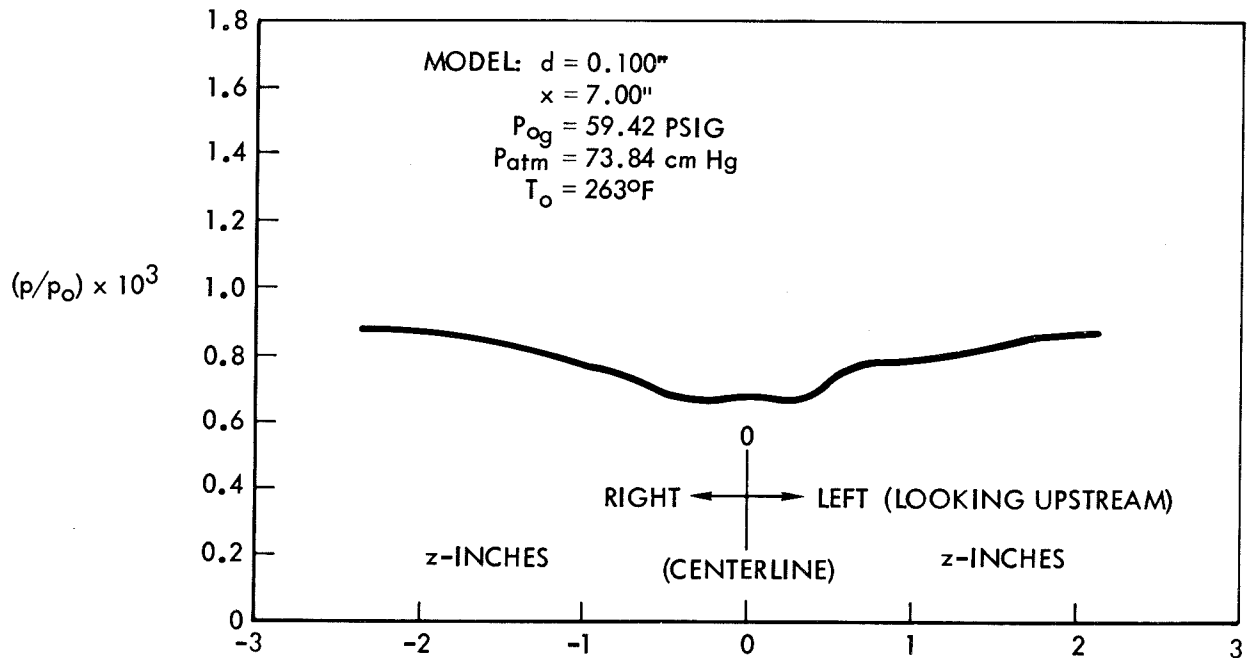
(d) 7.00 Inch Downstream Station

Figure 18. Typical Horizontal Static-Pressure Survey
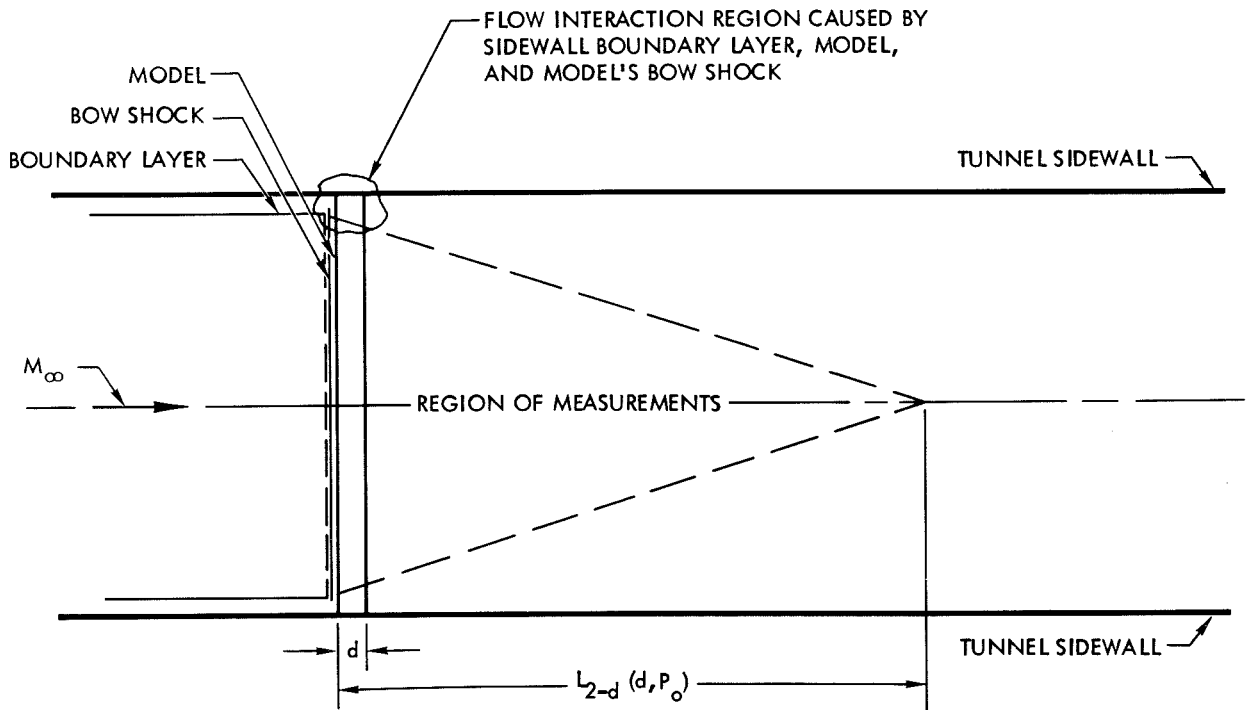
Figure 19. Two-Dimensional Region of Tests
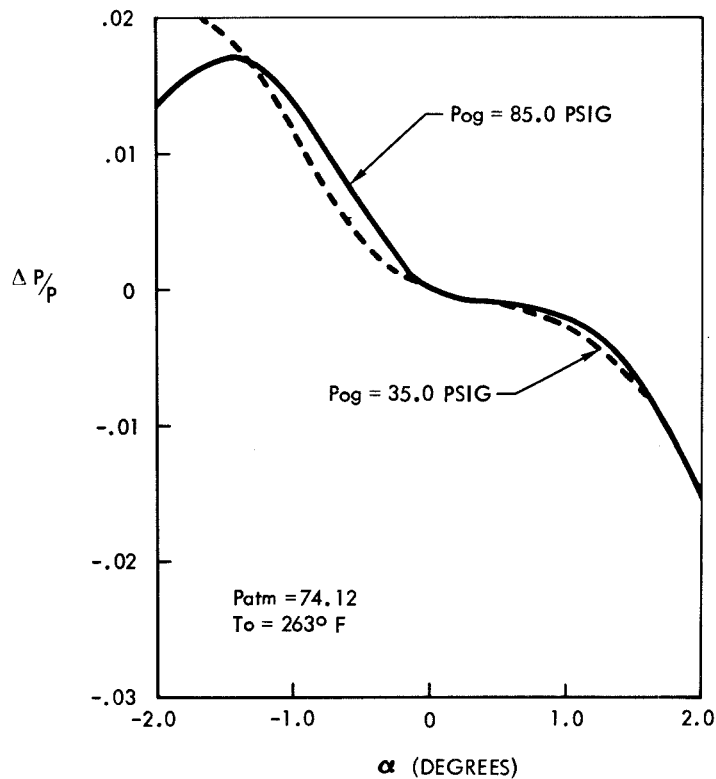
Figure 20. Angle-of-Attack Sensitivity of Static-Pressure Probe
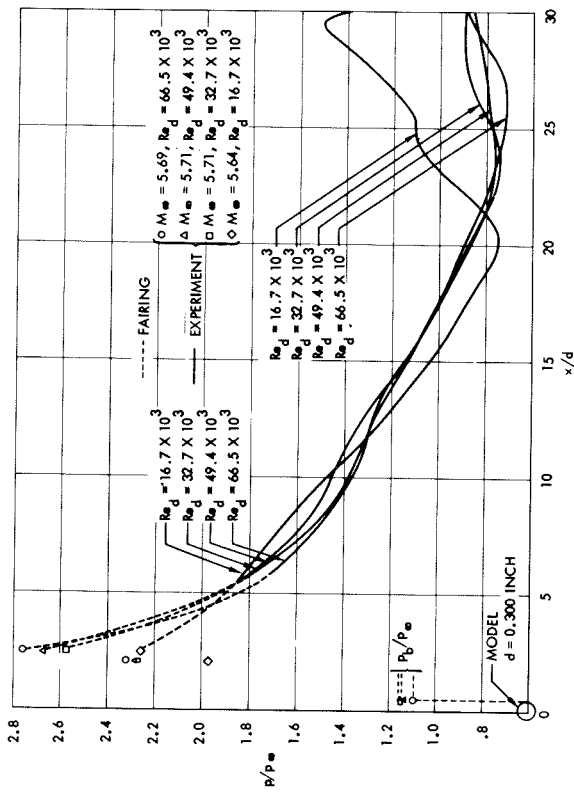
(a) 0.300 Inch Diameter Cylinder
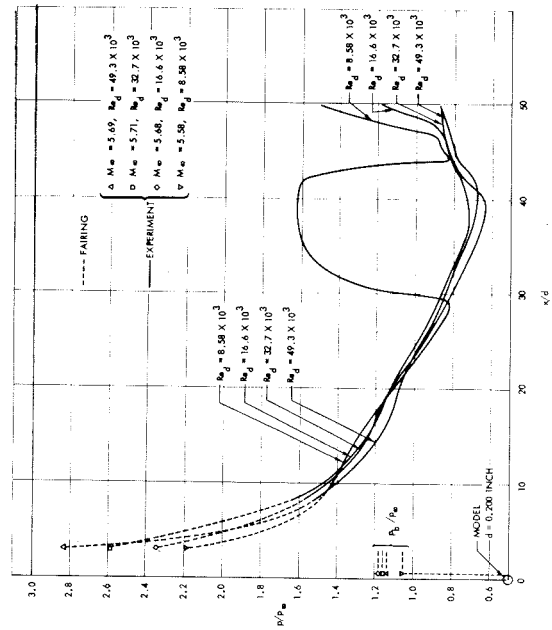
(b) 0.200 Inch Diameter Cylinder
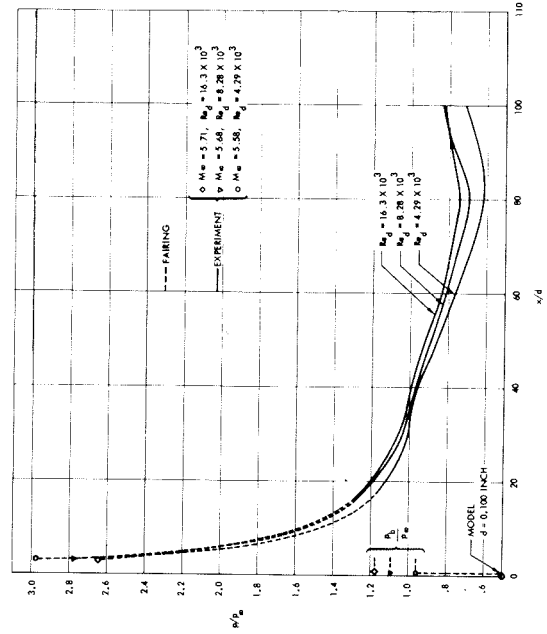
(c) 0.100 Inch Diameter Cylinder

Figure 21. Axial Static-Pressure Traces

the only error in angle of attack is due to installation which is estimated

to be accurate to less than 1 degree (the order of magnitude of the flow

uniformity). The static pressure is not a minimum at zero angle of

attack (Figure 20) because the three static-pressure holes (Figure 14)

were not symmetrical about the horizontal axis of symmetry.

After establishing that the pressure was constant across the wake —

and after identifying the boundaries of the two-dimensional region behind

the model—static-pressure traces were taken along the centerline of the

wind tunnel and behind the models for the 11 conditions cited in Table I.

The results of these tests are shown in Figure 21. As with the pitot

traces, the static-pressure traces were again checked by measuring the

pressure at several different stations on various days. Estimated

accuracy of the static-pressure measurements is $\frac{\Delta p}{p_\infty} = \pm 0.005$. As with

the pitot-pressure measurements, all axial static pressure traces were

supplemented by corresponding tunnel-empty surveys.

TOTAL-TEMPERATURE MEASUREMENTS

At first, attempts were made to measure total temperature with an

unheated thermocouple. However, this naive experiment using a bare

wire was unsatisfactory because the flow Reynolds number was very low

and varied over a wide range. Also, as shown in Figure 22, the adiabatic

wire temperature (i.e., the temperature associated with infinite aspect

ratio) is higher than the temperature measured by the thermocouple; this
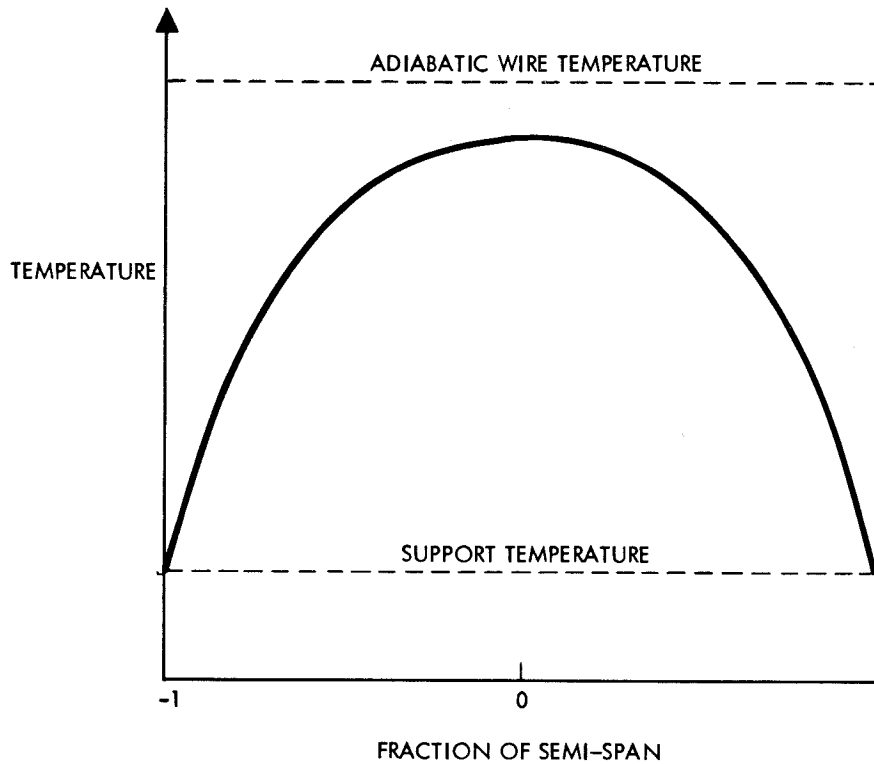
Figure 22.   Typical Temperature Distribution for Wire with
Unheated Supports

is attributable to the fact that the support temperature is lower than the

temperature at the center of the wire.   A detailed discussion of this

problem is presented by Dewey (Reference 14) wherein the end losses for

hot wires are investigated.   The correction associated with the tempera-

ture difference between the adiabatic wire temperature and the

thermocouple-measured temperature can be of the same order of

magnitude as the total-temperature differential being measured, especially

for turbulent flow.
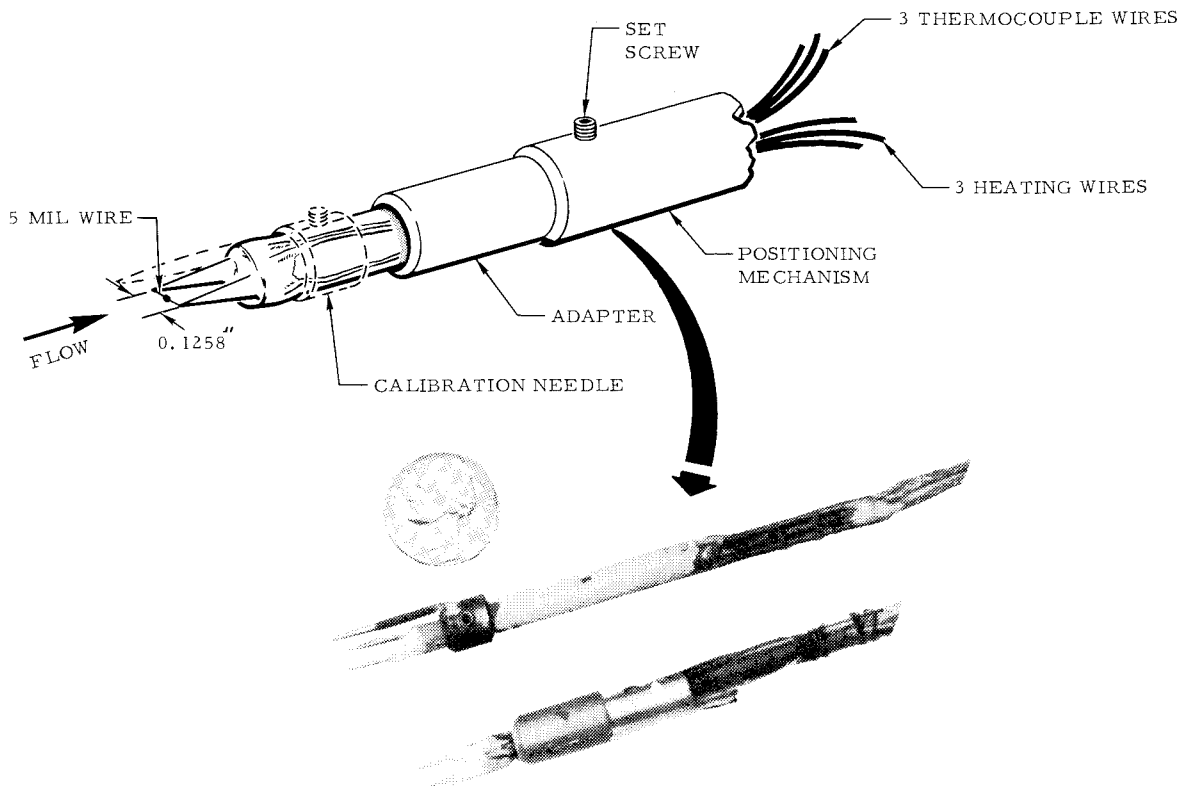
Figure 23.   Heated Thermocouple

Total temperature was ultimately measured by the heated

thermocouple shown in Figure 23, the details of which are given in

Appendix B.   Although the autograph was again used to record data, it

was employed as a potentiometer rather than a null recorder.

Because each total temperature trace required several hours, only

the traces shown in Figure 24 were taken with the corresponding tunnel-

empty data.   These traces were considered adequate for defining total-

temperature variation in the wake as a function of Reynolds number —

especially since the percentage variation of absolute temperature is small

(except in the vicinity of the neck) even for laminar flow.
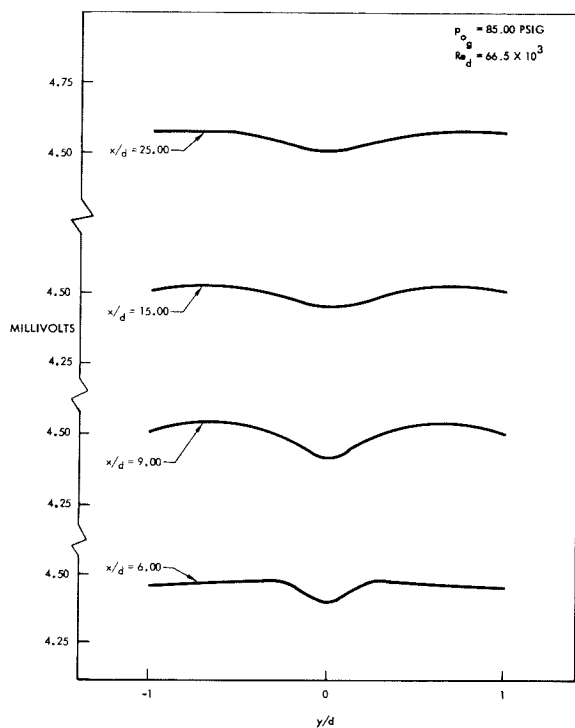
(a) P_{O_g} = 85.00 PSIG
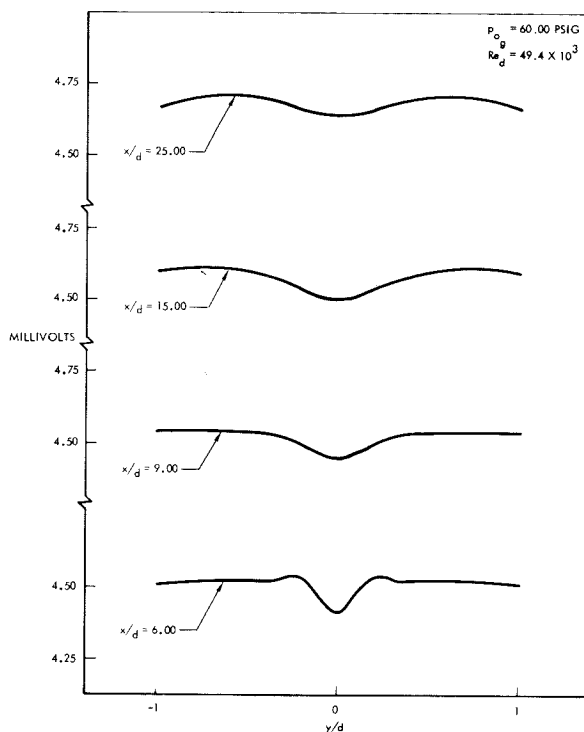
(b) P_{O_g} = 60.00 PSIG
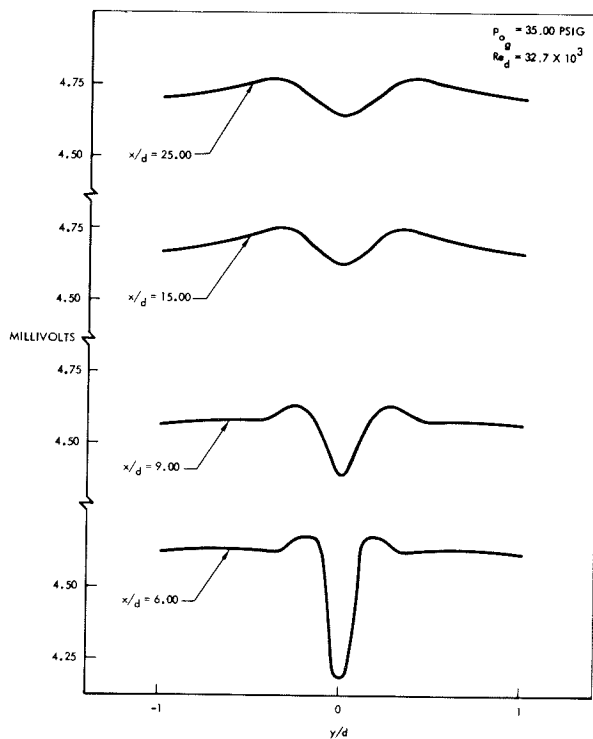
(c) P_{O_g} = 35.00 PSIG
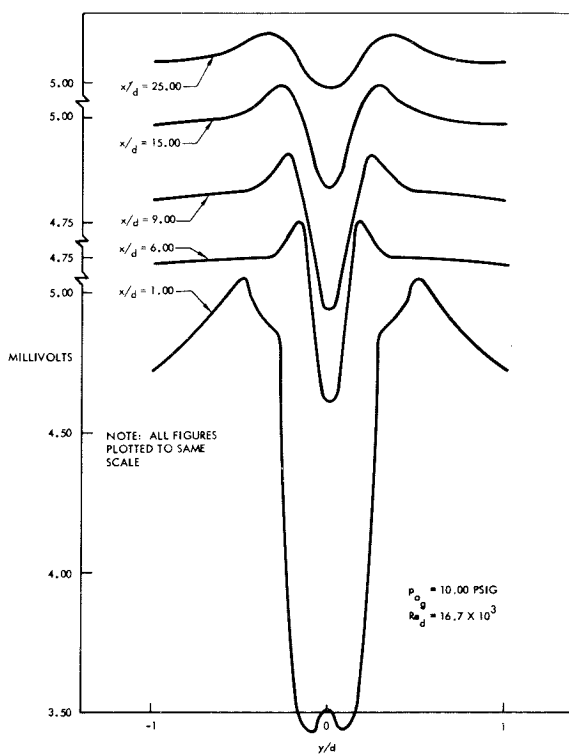
(d) P_{O_g} = 10.00 PSIG

Figure 24.   Total-Temperature Surveys

When the tunnel-empty data were reduced, they confirmed the calibration of reservoir temperature (discussed in Appendix A) to within 3 F. This difference is well within the value of $T_{aw}/T_o = 0.95 \pm 0.01$ for continuum flow given by Laufer and McClellan (Reference 24). Although the absolute level of free-stream total temperature was accurate to within 3 R, the total-temperature distributions are even more satisfactory because they represent modulated values about an absolute level. The accuracy of the thermocouple measurements is estimated at $\pm 1/2$ R.

BASE-PRESSURE MEASUREMENTS

To extrapolate the measured static-pressure traces in the wake, upstream, it was necessary to measure the base pressure of the model accurately (Section IV). The apparatus shown in Figure 25 was designed for this experiment. To obtain base-pressure measurements, the model was placed in the region of best flow—22 inches downstream of the throat. The best flow region was determined by the wind tunnel calibration discussed in Appendix A. Only the 0.300-inch diameter cylinder was used because of the finite size of the static-pressure orifices. The 0.009-inch diameter (Figure 25) was as small as practicality permitted, and it corresponded to about 3 degrees for a 0.300-inch diameter.

This experiment utilized three holes to check data duplicability; this was accomplished by blocking one or two holes. After duplicability was established, the time constant of the total system was considerably reduced by simultaneous use of the three holes. Pressure system volume was kept
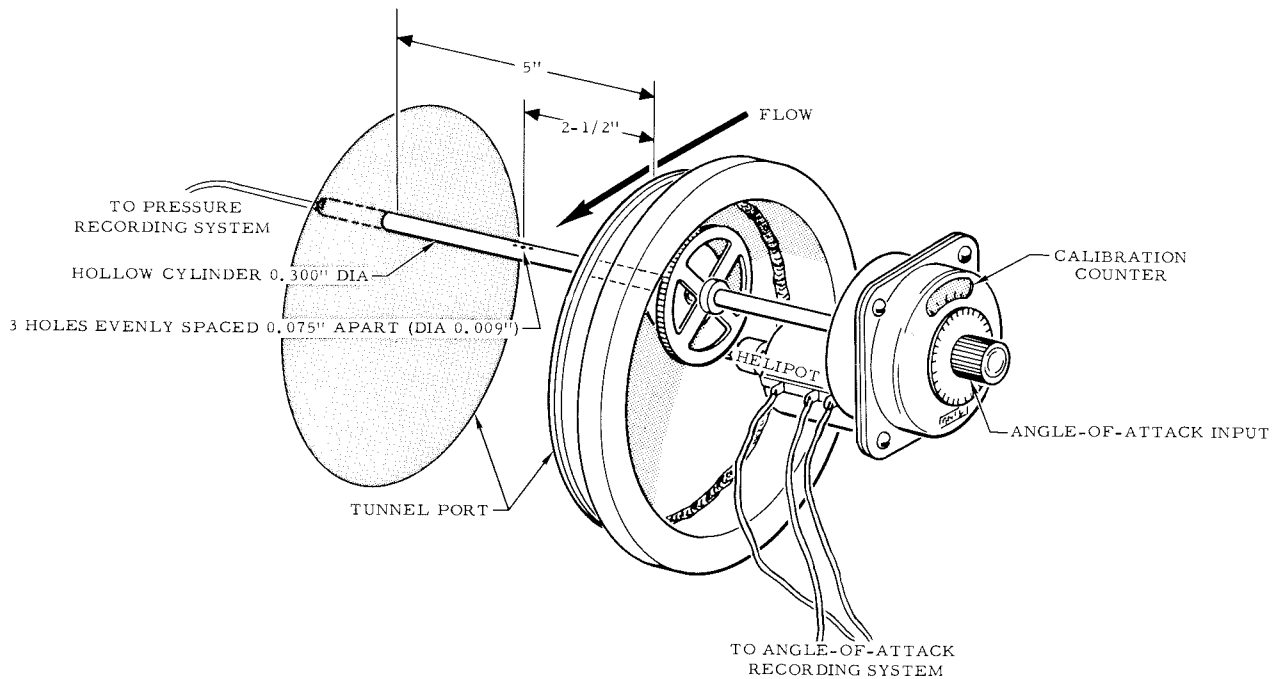
Figure 25. Apparatus for Measuring Base Pressure

to a minimum by filling the hollow cylinder with solder, leaving only a

minimum diameter outlet open. The pressure-recording system for this

experiment is identical to the system discussed earlier for static-

pressure measurements. The calibration counter (Figure 25) had a

100-to-1 turn ratio, permitting the angles to be measured to ±0.01 degree.

The base-pressure measurements determined by this experiment

are shown in Figure 26b. This figure also plots the author's best estimate

of the data of Tewfik and Giedt (Reference 25) whose experiments were

made at a much lower Reynolds number than the present tests. In

Figure 26b the region of reverse flow is evident, especially at high

stagnation pressure. Accuracy of the base-pressure measurements is
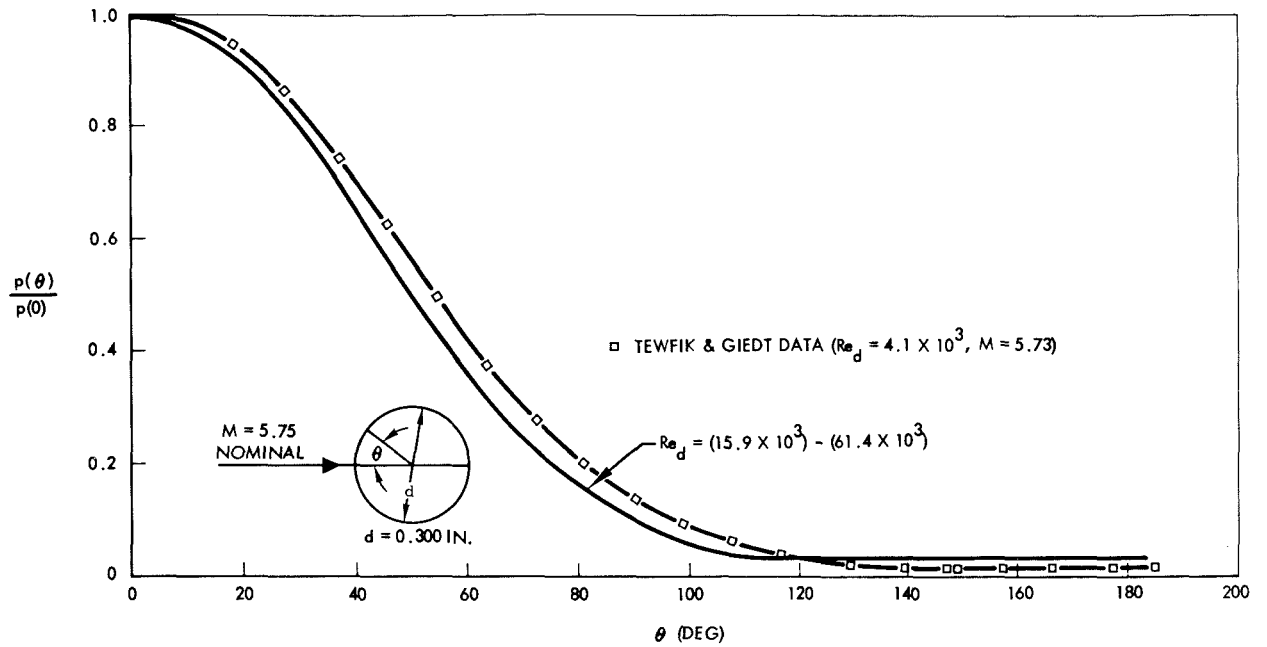
(a) Pressure Distribution on Cylinder
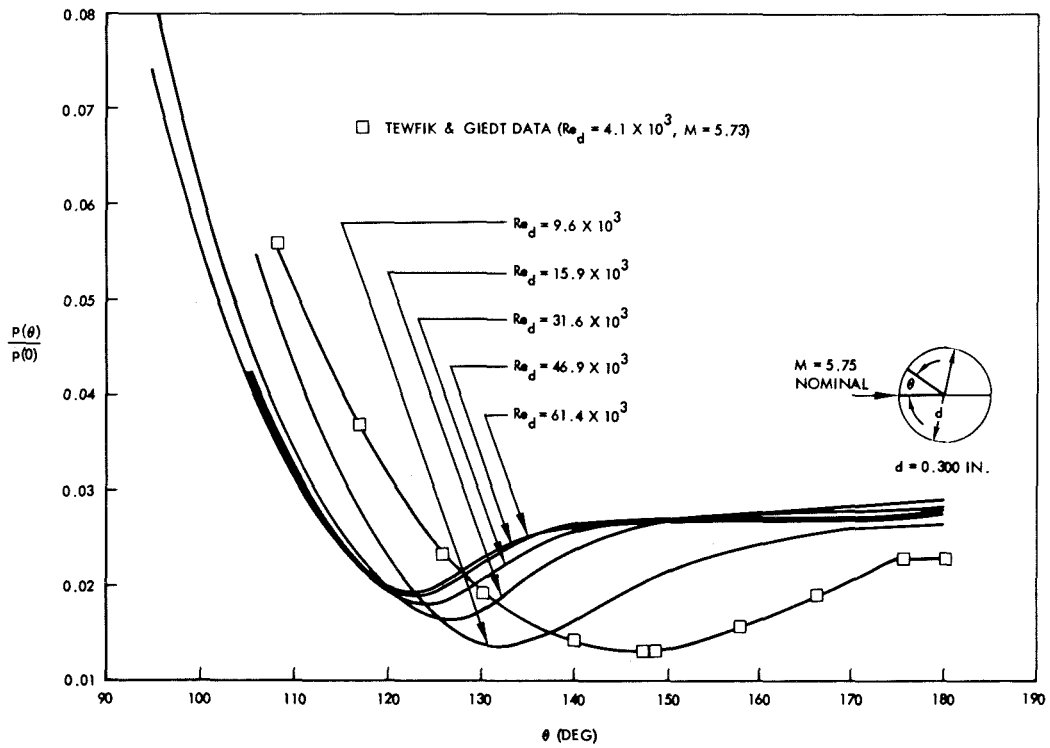
(b) Base Pressure

Figure 26. Experimental Pressure Distribution on Cylinder

estimated at $\Delta p(\theta)/p(0) = \pm 0.02$ for the lowest stagnation pressures as determined by the symmetry of the experimental data about the rear stagnation point. For the highest stagnation pressures, the accuracy is estimated at $\Delta p(\theta)/p(0) = \pm 0.01$.

In addition to the base-pressure measurements, the pressure distribution was measured over the entire surface of the cylinder with the setup shown in Figure 25. However, in this case, a conventional unbonded-strain-gage transducer was used because the sensitivity required was not large. The arrangement is shown in Figure 27. With this arrangement either atmospheric or vacuum reference could be utilized depending on the range of pressures being measured. The manometers A and B shown in Figure 27 refer to the outlets shown in Figure 7.

VALVE SEQUENCE

ATM ZERO		REAR		MANOMETER	
1	CLOSED	1	OPEN	1	OPEN
2	OPEN	2	CLOSED	2	OPEN
3	CLOSED	3	CLOSED	3	OPEN
4	OPEN	4	CLOSED	4	CLOSED
5	OPEN	5	CLOSED	5	CLOSED
6	CLOSED	6	OPEN	6	OPEN
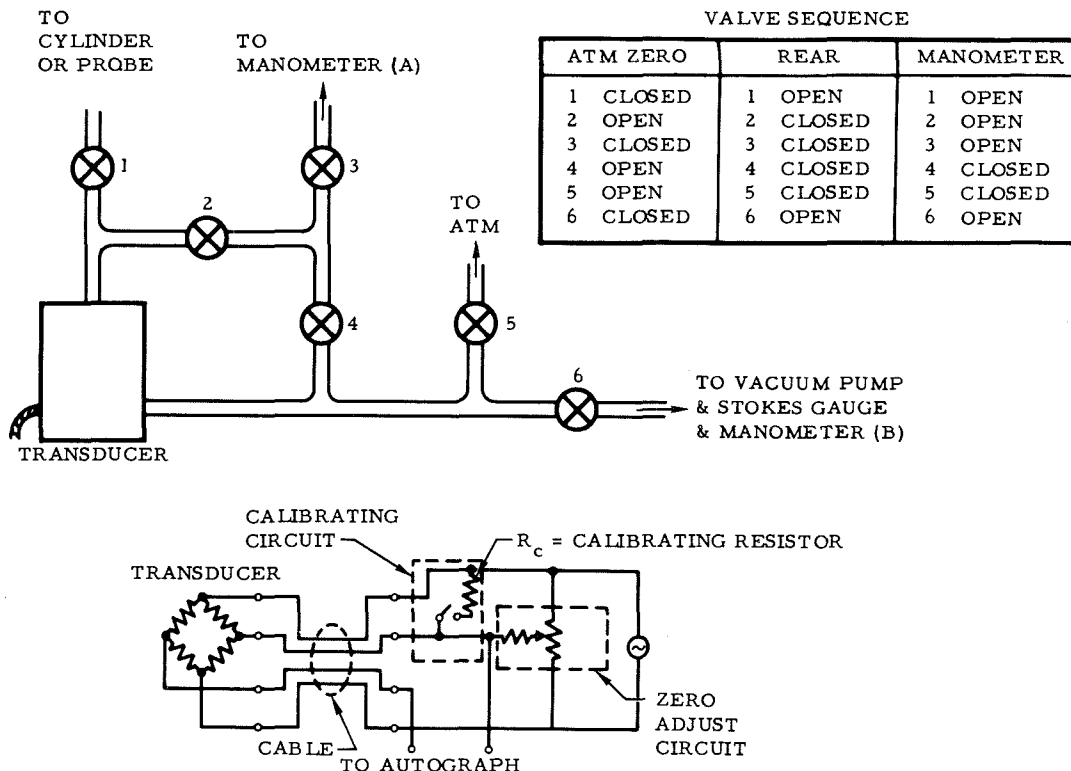
Figure 27. Transducer Circuitry for Base-Pressure Measurements

Demetriades (Reference 26) integrated the pressures obtained from this experiment and calculated a drag coefficient of 1.27 for the cylindrical rod as compared to a value of 1.2 to 1.3 as predicted by Ferri (Reference 27). The pressure distributions obtained are shown in Figure 26a. This figure also plots the values of Tewfik and Giedt (Reference 25). The accuracy of the data of Figure 26a was determined only by graphical reading error $(p(\theta)/p(0) = \pm 0.002)$.

As seen in Figure 26a, the dimensionless pressure distribution around the cylinder up to $\theta = 90°$ is practically independent of Reynolds number in the range considered. This is attributable to the fact that the effective shape of the cylinder does not change appreciably. It is obvious that the base pressure is a function of Reynolds number which will be discussed in Section IV.

III. DATA REDUCTION

PITOT PRESSURE

Reynolds number corrections to measured pitot pressures are shown

in Figure 28, which is taken from Matthews (Reference 28). For the

present tests, the outside diameter of the glass tip used for pitot measure-

ments (Figure 6) was chosen to preclude corrections when reducing the

experimental data. The outside diameter allowed sufficient resolution in

pitot pressure (Figure 9); the inside diameter was large enough to prevent

the time constant of the pressure-recording system from being noticeably

penalized. No account was taken of the effective displacement of
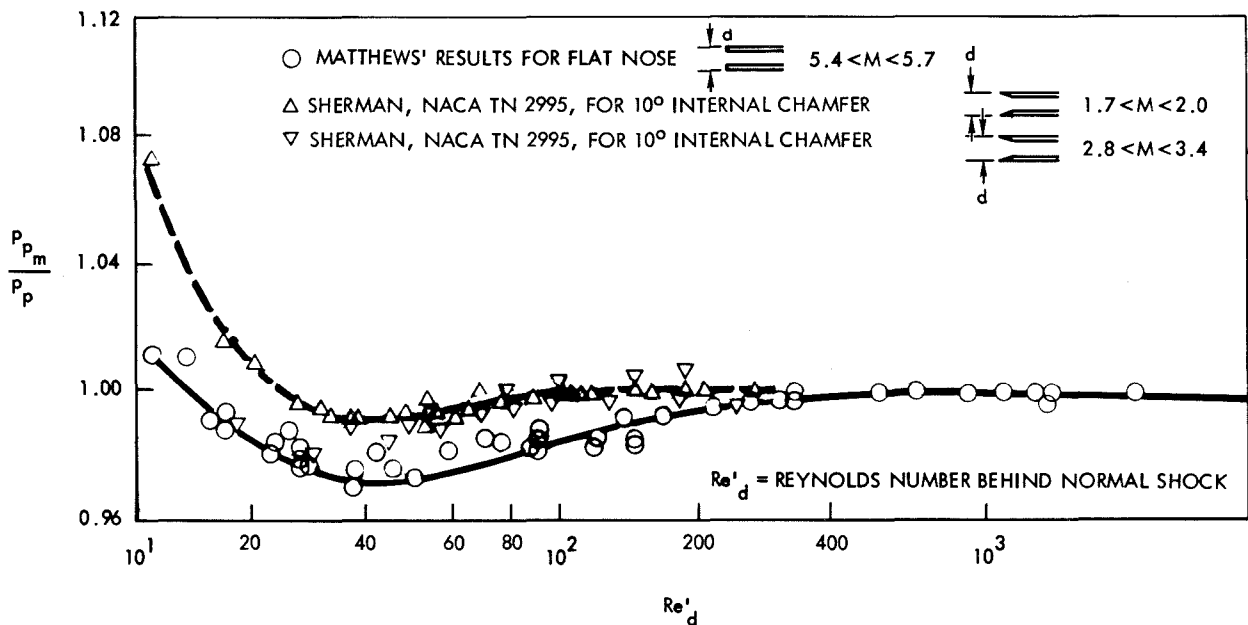
Figure 28. Variation of Measured Impact Pressure With Reynolds Number
(Figure from Reference 28)
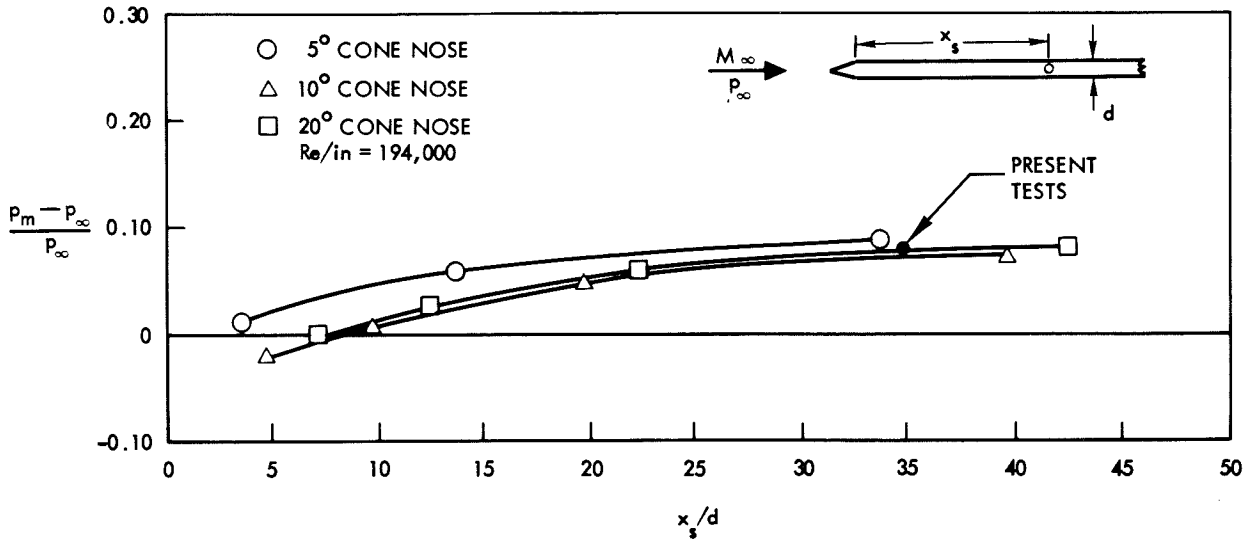
Figure 29. Pressure Distribution on Static-Pressure Probes
(Figure From Reference 28)

streamlines caused by velocity gradients present in the wake. Hill, Baron, and Schindel, (Reference 29) and Marson and Lilley (Reference 30). This correction was estimated to be less than 10 percent of the wake width for the worst case, i. e., in the vicinity of the neck. This subject is presented in greater detail in a subsequent section dealing with a discussion of accuracy.

STATIC PRESSURE

To correct the values of static pressure for boundary-layer effects as measured by the probe shown in Figure 14, Matthews' data (Reference 28) were used as shown in Figure 29. These data were

taken for static-pressure probes of the same geometry as that used for the present tests. The calibration point for the present tests is shown in Figure 29. Based on this point, a value of the viscous interaction parameter, χ, was calculated. A linear variation was then assumed for the value of measured pressure to ideal pressure as a function of the viscous interaction parameter,

$$p_m/p = 1 + 0.235 \, \chi. \tag{2}$$

as expected, this variation is less than that for an insulated flat plate as discussed by Hayes and Probstein (Reference 31, p. 349).

TOTAL TEMPERATURE

The temperature as measured by the heated thermocouple (discussed previously in Section II) is the adiabatic wire temperature associated with infinite aspect ratio. However, the adiabatic wire temperature must be corrected for Knudsen number to obtain the true total temperature. This correction was accomplished with the data shown in Figure 30 which is based on Dewey's work (Reference 14). The ordinate is normalized so that the asymptotic value for free-molecule flow is equal to one and the asymptotic value for continuum flow is equal to zero. The values for free-molecule flow and continuum flow correspond to ratios of adiabatic wire temperature to total temperature of $\frac{7}{6}$ and 0.95, respectively.

THEORETICAL LIMIT OF FREE-MOLECULE FLOW

$Kn_\infty > 10$

$T_{aw}/T_o = 7/6 \leftarrow 1.0$

$\bar{\eta}_*$

O   DEWEY'S RESULTS, MACH 5.80

LAUFER & MC CLELLAN, MACH 1.33 – 4.54 (WITHOUT END CORRECTIONS)

● LAUFER & MC CLELLAN, MACH 3.05 (WITH END CORRECTIONS)

+ SHERMAN, MACH 2.0 & 4.0

x STALDER, GOODWIN & CREAGER

$$\text{KNUDSEN NO.} = \sqrt{\frac{\gamma}{2}} \left(\frac{M_\infty}{Re_{WIRE}} \right)$$

$$Re_{WIRE} = \frac{\rho_\infty \, u_\infty \, d_{WIRE}}{\mu_\infty}$$

EXPERIMENTAL LIMIT OF CONTINUUM FLOW

$T_{aw}/T_o = 0.95 \leftarrow 0$

10^{-1} 10^0 10^1

LOG$_{10}$ KNUDSEN NUMBER
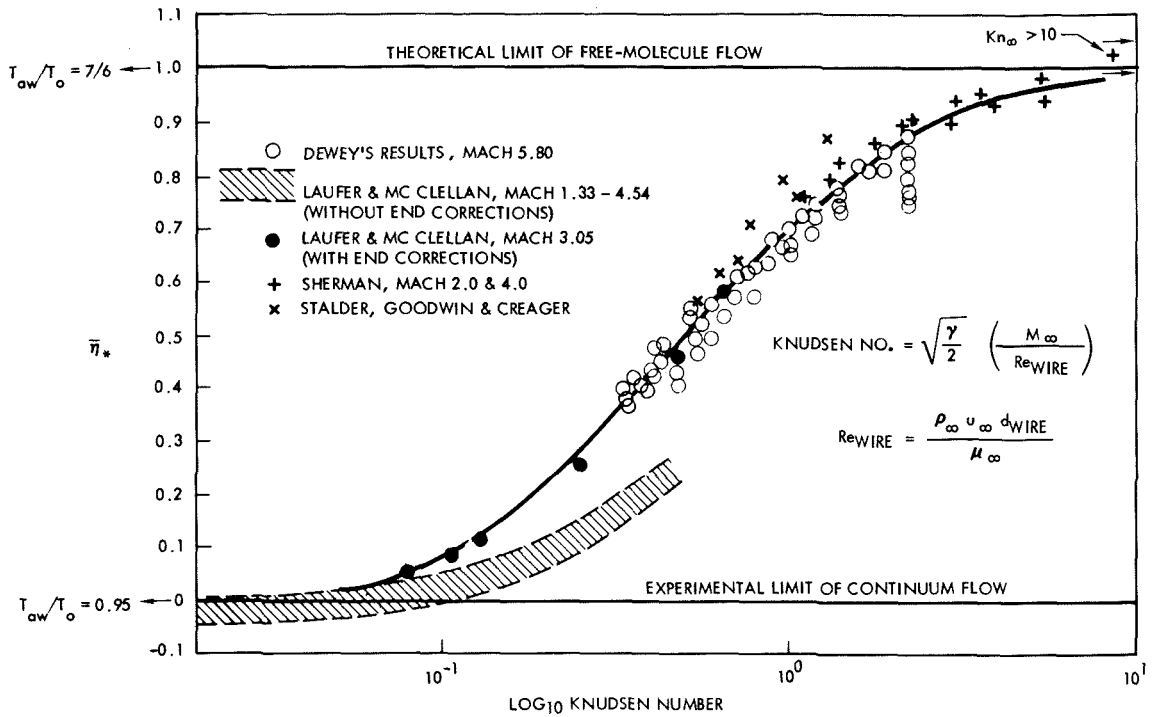
Figure 30.   Recovery Temperature Versus Knudsen Number (Figure from Reference 14)

IBM 7090 COMPUTATION

As explained previously, two iterations were necessary to reduce the experimental data. The static pressure as measured by the probe required a correction for the viscous interaction parameter, and the total temperature as measured by the thermocouple required a correction for Knudsen number. Neither the viscous interaction parameter nor the Knudsen number were known beforehand. Also, inasmuch as the laminar theory (Section V) is developed in terms of transformed coordinates which involve running integrals, it was decided to reduce the experimental data by programming them for 7090 computation.

To provide total-temperature distributions for all the cases of interest (Figure 24), all the available total-temperature measurements were first reduced. Utilizing Reynolds number correspondence, the distributions were then used as input data to the IBM program for all the cases. This procedure was considered satisfactory for two reasons: (1) data existed for both laminar and turbulent flow, and (2) the defect in total temperature was less than 3 percent in terms of absolute temperature— except for the cases upstream of the neck.

In the computations, the Mach number was then determined by standard compressible-flow techniques (Reference 32) using the corrected values of static pressure and pitot pressure. With the Mach number and the assumed value of total temperature, all other pertinent quantities could be computed. The IBM 7090 program was written so that all quantities of interest were printed out and automatically plotted by a cathode-ray tube.

DISCUSSION OF ACCURACY

As noted in the preceding portions of this section, the accuracy of each measurement was carefully identified. However, because of the many involved calculations necessary in obtaining final data, the accuracy of the final product can only be roughly estimated. To estimate the cumulative error, the following factors were considered.

All location and dimensional measurements were made to an accuracy of ±0.001 inch and all distance-measuring devices were

carefully calibrated at thermal equilibrium. A minimum of several hours was allowed for reference-pressure stabilization, and a minimum of several minutes was allowed for model surface and base static-pressure stabilization. Flow uniformity was perhaps the most critical parameter in the experimental data. This fact became evident when models were tested at various axial locations in the wind tunnel (Section II). Closely associated with flow uniformity is the region of two-dimensionality cited in the static-pressure measurements discussion in Section II. The effect of the variation of static pressure due to disturbances from the model supports is somewhat alleviated, however, because the theory (discussed later in Section V) is based on actual edge conditions.

The manner in which the wake edge was defined (discussed later in Section VI) presents a potential source of final data error; however, even at best the wake edge is an arbitrary quantity. The extrapolation of static pressure upstream in the region of the neck (a detailed discussion is presented in Section IV) is estimated to be within 5 percent. The use of Reynolds number correspondence to determine total-temperature profiles in data reduction (already cited in this section's discussion of IBM 7090 computation) is not considered a large source of error.

Although repeatability of experimental data was relatively simple to establish quantitatively, all errors associated with probes could not be determined. For example, the pitot-probe error associated with velocity gradient was not determined. As discussed by Hill, Baron and Schindel

(Reference 29) and Marson and Lilley (Reference 30), impact measurements do not reflect the pitot pressure on a streamline aligned with the probe axis; rather, these measurements reflect pitot pressure on the streamline displaced towards the regions of higher velocities. This phenomenon was not considered because reliable correction data were not available. This effect was minimized, however, by keeping the diameter of the impact-pressure probe as small as possible (Figure 6), and it is estimated that the maximum displacement due to this effect is 0.007 inch. Probe errors caused by misalignment with the flow direction were not considered significant (Figures 12 and 20) because the error in the probe angle of attack was less than 1.0 degree.

Fortunately, the machine computations do not introduce additional errors due to arithmetic. However, when the experimental data was digitized some error was accepted because only a finite number of points could be taken. As discussed previously, the methods of reducing experimental data to ideal quantities are somewhat inaccurate. In all cases however, the experimental apparatus was designed to ensure that these corrections were small; consequently, little accuracy loss was experienced.

Assuming that the edge of the wake was properly defined, it is estimated that the overall accuracy of the final experimental data is from 2 to 4 percent for the distributions of normalized velocity, static enthalpy, and total enthalpy except in the immediate region of the neck.

It is estimated that the computed absolute values of the centerline

quantities is accurate to within 5 percent.   The major source of error is

considered to be the extrapolation of static pressure upstream which is

worse in the neck region.

IV. CONDITIONS NEAR BODY

The orifices of the static-pressure probe (Figure 14) were located a fixed distance behind the apex of the probe cone; therefore, it was not possible to obtain experimental values of static pressure close to the neck. The difficulty this presents is illustrated in Figure 31 —where data between Stations 1 and 2 are undetermined. Consequently, it was necessary to estimate the static pressure in the vicinity of the neck from available data. Unfortunately, because the axial gradient in static pressure is high the extrapolation upstream of the measured data is inaccurate unless a value of the static pressure at the neck is available.

Figure 31. Experimental Static Pressure
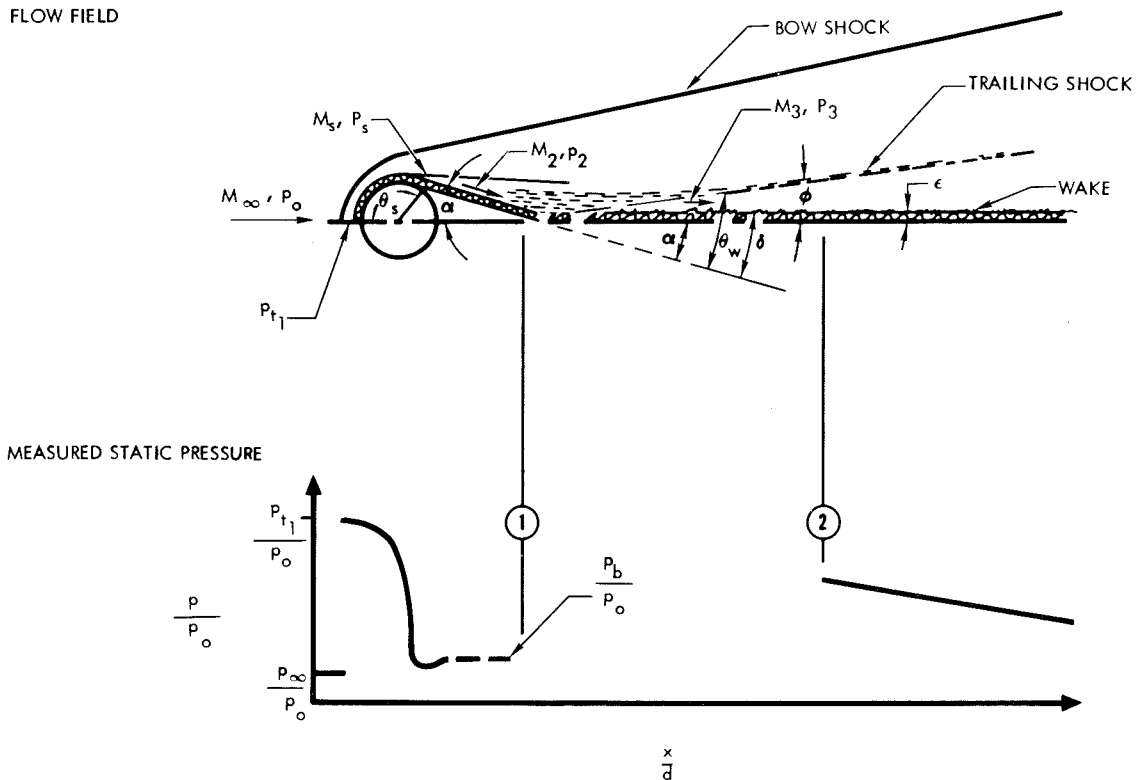
SEPARATION ON CYLINDER

The first step in estimating the static pressure at the neck was to define the conditions at separation on the cylinder. From the base-pressure measurements (Figure 26), a qualitative definition of the separation angle with Reynolds number is possible; however, the 0.009-inch diameter of the static-pressure orifices of the hollow cylinder (Figure 25) prevented the separation angle from being defined closer than 3 degrees in angle which corresponds to the orifice diameter for the 0.300-inch-diameter cylinder. The problem is further aggravated by the fact that at separation the flow turns through an angle before sliding down the shear layer.

To attack this problem, the simple schematic shown in Table II was developed to define the quantities of interest. The base-pressure measurements discussed in Section II were then exploited. From pitot-pressure surveys immediately behind the body (Figure 32), it was demonstrated experimentally that the separation shock is negligibly weak—i.e., there is no total pressure loss through it locally. Therefore, the separation shock was neglected in the simple model of Table II. The turning angle at separation was approximated by the step model shown in Figure 33. As shown by LeBlanc and Webb (Reference 33) in Figure 34, for laminar flow the pressure at separation, p_s, is halfway between the initial and final pressures. This conclusion, which is supported by experimental evidence taken from Chapman's work (Reference 34), is applicable even for finite pressure gradients.

Table II Conditions for Separation on Cylinder
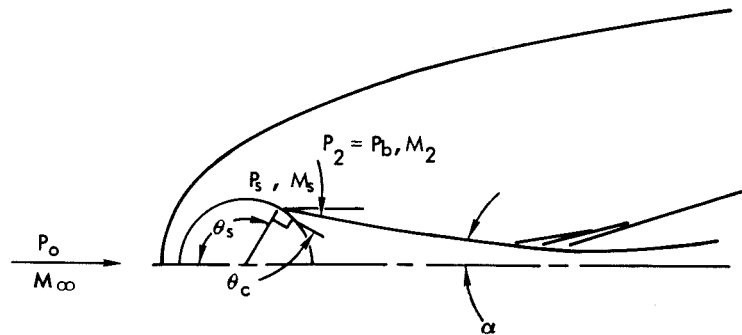
P_{og} psig	$M\infty$	Re_d $\times 10^{-3}$	θ_s degrees	M_1	M_s	M_2	θ_c degrees	α degrees	P_b/P_o $\times 10^3$
85.00	5.87	61.4	123.3	3.72	3.24	3.03	18.3	15.0	0.849
60.00	5.83	46.9	123.0	3.74	3.26	3.01	19.6	13.4	0.892
35.00	5.79	31.6	123.8	3.79	3.30	3.00	21.8	12.0	0.927
10.00	5.74	15.9	127.0	3.88	3.38	2.99	26.2	10.8	0.990
0.00	5.71	9.60	131.5	4.01	3.51	3.02	30.3	11.2	0.960
Tewfik & Giedt	5.73	4.10	147.0	4.29	3.77	3.10	38.8	18.2	0.839
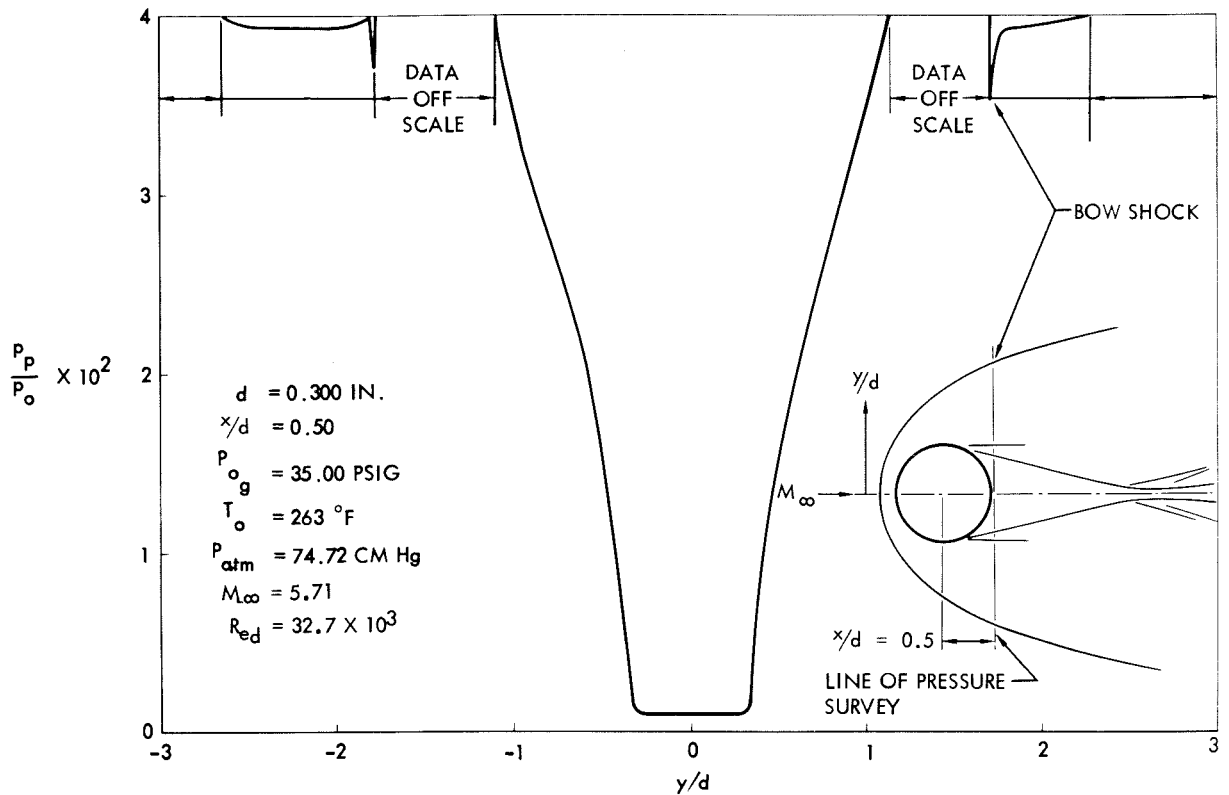
Figure 32.   Pitot-Pressure Survey Close to Model
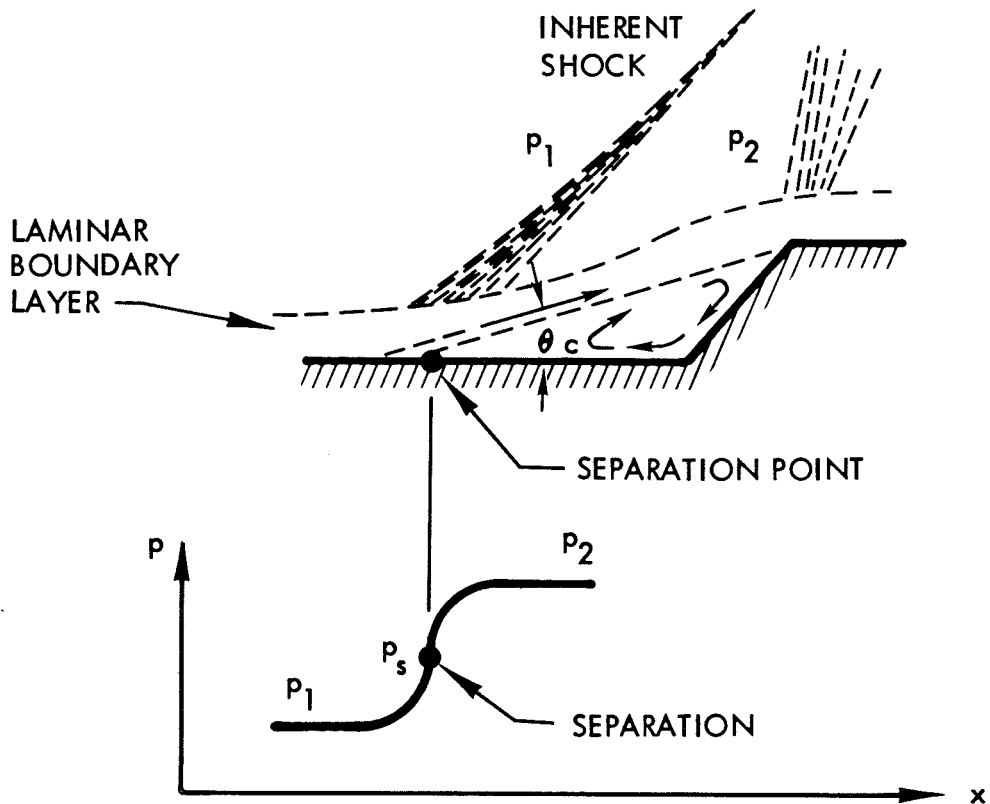
Figure 33.   Step Model
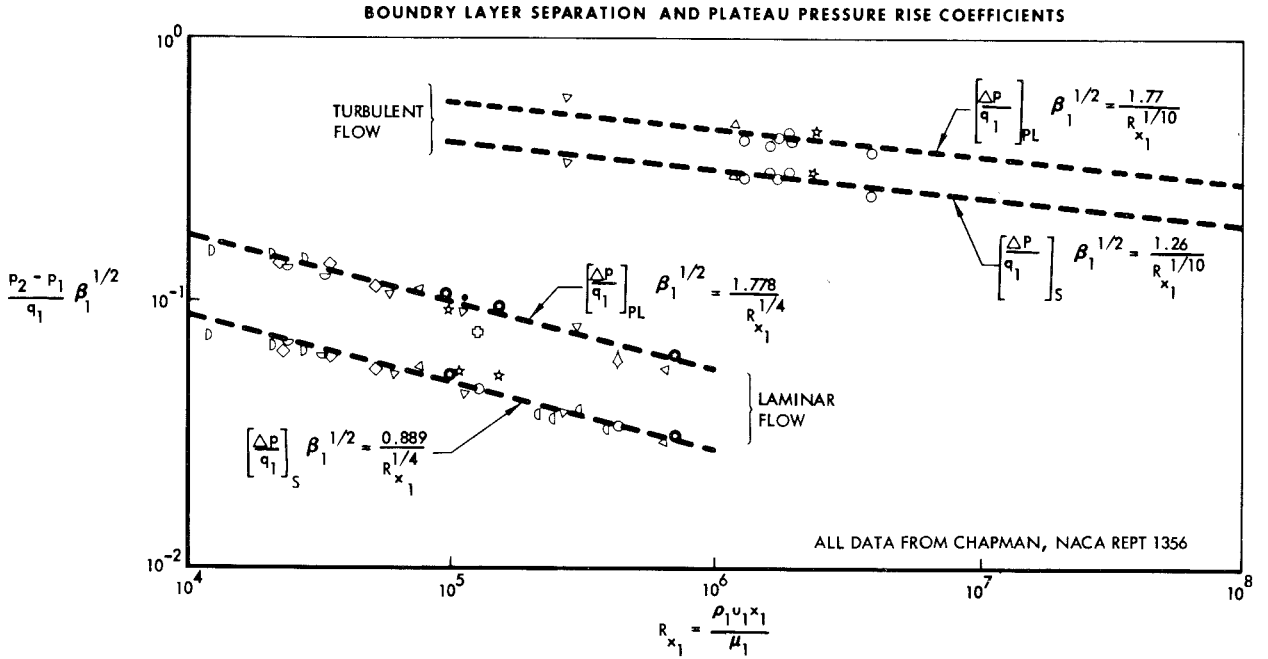
Figure 34.   Boundary Layer Separation and Plateau Pressure
Rise Coefficients
(Figure from Reference 33)

Hakkinen, Greber, Trilling and Abarbanel (Reference 35) have shown
that for the step model of Figure 33

$$C_p = C_1 \sqrt{\frac{c_{f_1}}{\beta_1}}$$ (3)

where

C_p is the pressure coefficient, $\dfrac{\Delta p}{q}$

C_1 is a constant

q is the dynamic pressure, $\dfrac{1}{2} \rho u^2$

c_f is the skin friction coefficient, $\dfrac{\tau}{q}$

β is equal to $\sqrt{M^2 - 1}$

M   is the Mach number.

Utilizing first-order perturbation theory (e. g. Reference 36, p. 92)

$$\frac{p_2 - p_1}{p_p} = \frac{\gamma M_1^2}{\beta_1} \theta_c \tag{4}$$

where

γ is the specific-heat ratio

θ_c is the turning angle

Since the skin-friction coefficient varies as (Reference 37)

$$c_f \sim \frac{1}{\sqrt{R_{e_{local}}}} \tag{5}$$

where

$R_{e_{local}}$ is the Reynolds number based on local conditions and the length of laminar run, and assuming that

$$\frac{1}{\sqrt{R_{e_{local}}}} \sim \frac{1}{\sqrt{R_{e_d}}} \tag{6}$$

where

R_{e_d} is the Reynolds number based on free-stream conditions and the model diameter,

then

$$\theta_c = C \frac{\sqrt{\beta_1}}{\sqrt{Re_d}} \tag{7}$$

$$\frac{p_2}{p_1} = 2 \frac{p_2}{p_s} = 1 + C \frac{\gamma M_1^2}{\sqrt{\beta_1} \sqrt[4]{Re_d}} \tag{8}$$

where for our case (Table II)

$$\theta_c = \theta_s - \frac{\pi}{2} - a \tag{9}$$

The assumption of Equation 6 is reasonable based on Chapman's (Reference 38) order-of-magnitude analysis of base-pressure coefficients.

It should be noted that the step model used above assumes zero pressure gradient. With finite pressure gradient, the constant, C, in Equations 7 and 8 merely changes value as shown by Greber (Reference 39). To determine the constant, C, for this case, base-pressure data were correlated with schlieren photographs from which the angle of shear layer was obtained. (It should be noted that schlieren photographs in cases where the shear layer was well defined were available only for the highest pressures.) For the circular cylinder, the value of the constant, C, in Equations 7 and 8 was found to be equal to 2.66 for the circular cylinder based on these experimental data. It is interesting to note that, as pointed out by Guman, (Reference 40) C = 1.1 for the following cases: (1) a compression corner, laminar separation upstream of the corner but downstream of the leading edge, (2) a step corner the height of which is on the order of several boundary-layer thicknesses, laminar separation upstream of the corner but downstream of the leading edge, and (3) pure laminar separation induced by an incident shock. For a compression corner with laminar leading-edge separation, a value of 2.1 checks with available experimental data.

An attempt was made to predict the angle of the shear layer by expanding the flow from 90 degrees on the cylinder to the base pressure by

simple wave mechanics. However, it was found that this procedure produced shear-layer angles approximately 4 degrees too high, based on experimental data. From these calculations, it was concluded that the expansion from parallel flow at θ = 90 degrees to the base pressure cannot be approximated by a simple wave.

Once the constant, C, was established in Equations 7 and 8, the data given in Figure 26b was then utilized to give the quantities tabulated in Table II. Final results of these calculations are shown in Figures 35, 36, and 37. In Figure 35, two methods of non-dimensionalization are used; the different curves represent the effect of the change of free-stream Mach number with wind tunnel stagnation pressure. To extend the present tests into the regime of lower Reynolds number, the data of Tewfik and Giedt (Reference 25) are also presented. The points represent the author's best interpretation of the data of Reference 25.

CONDITIONS AT NECK

Having obtained plots of separation angle, θ_s, and effective initial Mach number, M_1, as functions of Reynolds number (Figures 36 and 38) from the base-pressure measurements by means of the simple model discussed in the preceding portion of this section, these data were then used to obtain values of static pressure in the neck region. The Mach number M_1 is a fictitious quantity and can be interpreted as the Mach number that would be obtained at θ_s if separation did not occur. The quantities of interest in this analysis are shown in Table III. The shear layer was assumed to be a
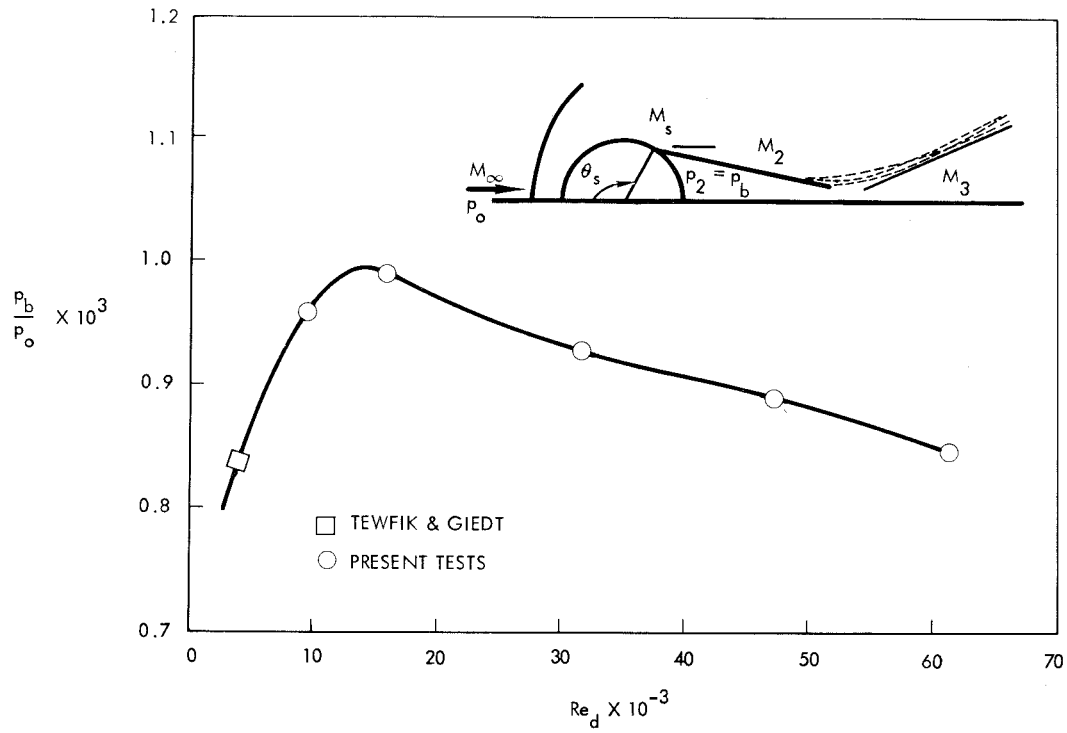
(a) Relative To Total Pressure
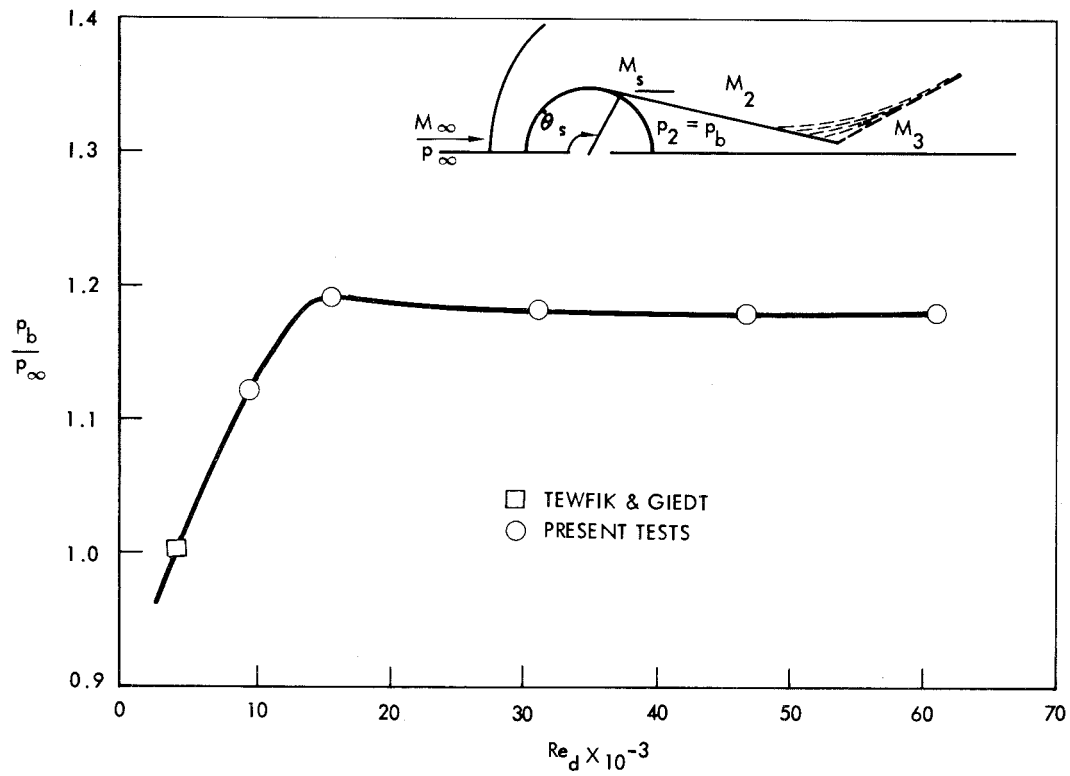
(b) Relative To Static Pressure

Figure 35. Base Pressure Versus Reynolds Number
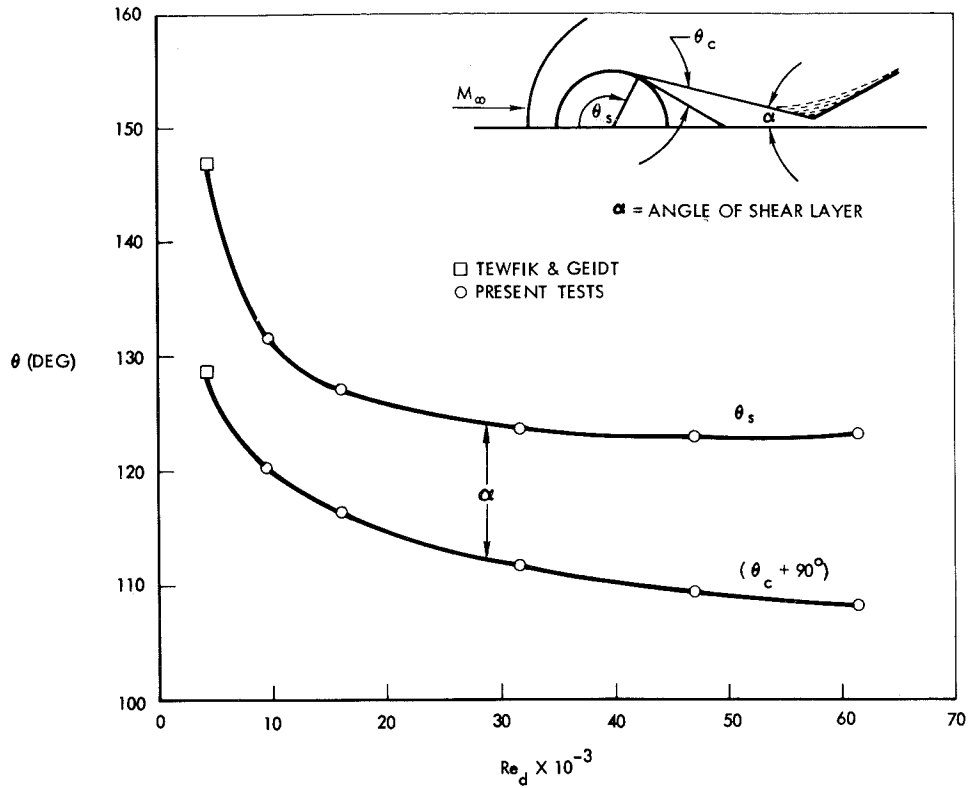
Figure 36. Separation Angle and Turning Angle Versus Reynolds Number
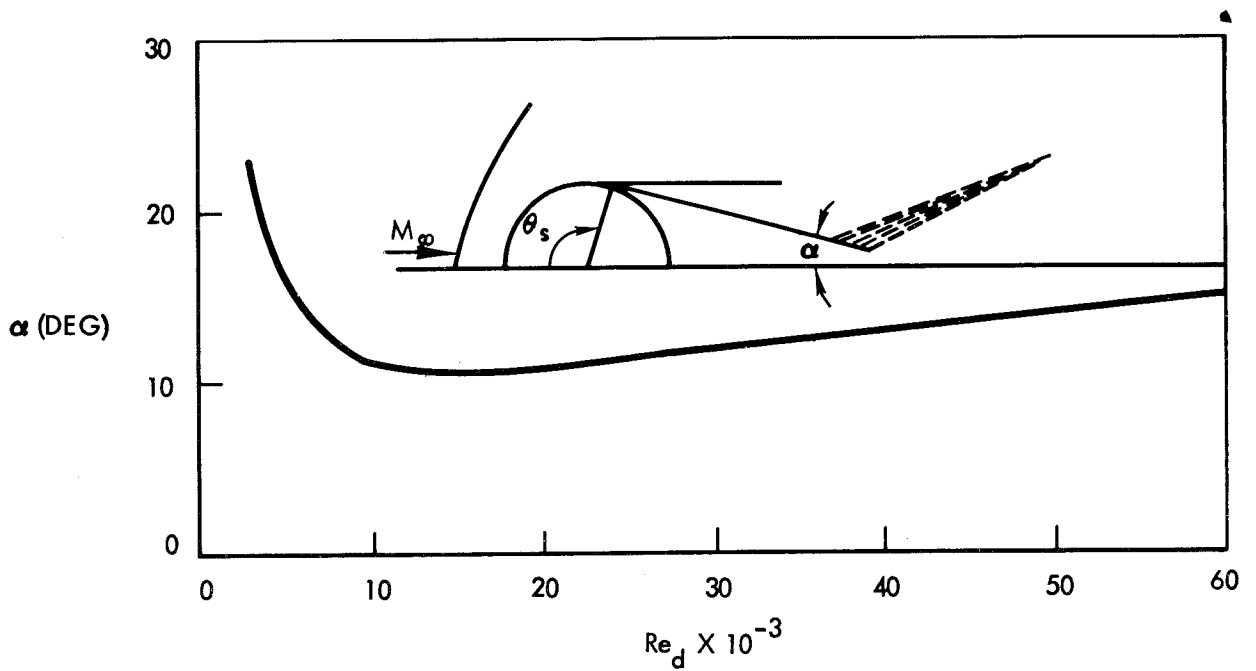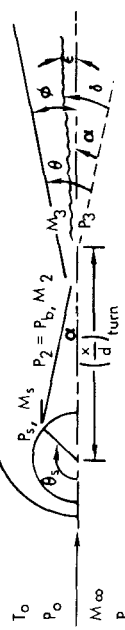
Figure 37. Angie of Shear Layer Versus Reynolds Number

Table III Conditions Around Neck

Model: d inch	P$_{og}$ psig	P$_{atm}$ cm Hg	T$_o$ °F	M∞	Re$_d$ × 10⁻³	M$_1$	M$_s$	θ$_s$ degrees	α degrees	M$_2$	P$_2$/P∞	φ degrees	ε degrees	M$_3$	P$_3$/P∞	(x/d)$_{turn}$	P$_2$/P∞ @	x/d
0.300	85.00	74.69	263	5.69	66.5	3.72	3.23	123.5	15.6	3.03	1.09	15.7	-1.3	2.32	2.99	1.77	2.75	2.50
																	2.32	2.00
0.300	60.00	74.53	263	5.71	49.4	3.73	3.25	123.0	13.6	3.00	1.14	15.6	-1.7	2.41	2.67	2.01	2.66	2.50
																	2.28	2.00
0.300	35.00	74.33	262	5.71	32.7	3.79	3.30	123.7	12.1	3.05	1.15	15.8	-1.5	2.48	2.47	2.22	2.59	2.64
																	2.27	2.14
0.300	10.00	74.36	262	5.64	16.7	3.87	3.38	126.7	10.8	2.99	1.15	15.5	-2.1	2.56	2.17	2.40	2.27	2.50
																	1.98	2.00
0.200	96.68	74.44	264	5.69	49.3	3.74	3.25	123.0	13.6	3.01	1.13	16.2	-0.9	2.39	2.78	2.01	2.82	3.00
0.200	59.48	74.67	263	5.71	32.7	3.79	3.30	123.7	12.1	3.01	1.14	15.7	-1.7	2.49	2.45	2.22	2.59	3.00
0.200	22.48	74.57	262	5.67	16.6	3.87	3.38	126.8	10.9	2.99	1.16	15.7	-1.9	2.55	2.23	2.38	2.34	3.00
0.200	3.80	74.69	260	5.58	8.58	4.04	3.54	132.9	11.6	3.03	1.06	15.7	-1.5	2.53	2.21	2.12	2.19	3.00
0.100	59.42	74.54	263	5.71	16.3	3.87	3.38	126.9	10.9	2.99	1.18	16.5	-1.0	2.50	2.40	2.38	2.65	3.00
0.100	22.54	74.56	262	5.68	8.28	4.05	3.55	133.4	11.8	3.03	1.09	17.0	-0.1	2.45	2.55	2.08	2.78	3.00
0.100	3.84	74.71	260	5.58	4.29	4.28	3.75	146.2	17.9	3.10	0.95	17.0	+0.2	2.16	3.34	1.28	2.97	3.00

line which the flow paralleled before undergoing a turn which induced the

trailing shock.   The separation angle θ_s, and the fictitious Mach number,

M_1, were used as basic quantities to define the flow.   They were thus

employed because their variation with Reynolds number was smooth

(Figures 36 and 38).   Using Equations 7 and 8 as well as the experimental

value of the trailing shock angle, ϕ, which was obtained from pitot-pressure

measurements, the quantities given in Table III can be easily calculated

through use of standard two-dimensional compressible-flow techniques.

It should be indicated that at least one redundancy is present for these

calculations (the experimental value of the pitot pressure at the neck) which

serves as a check.
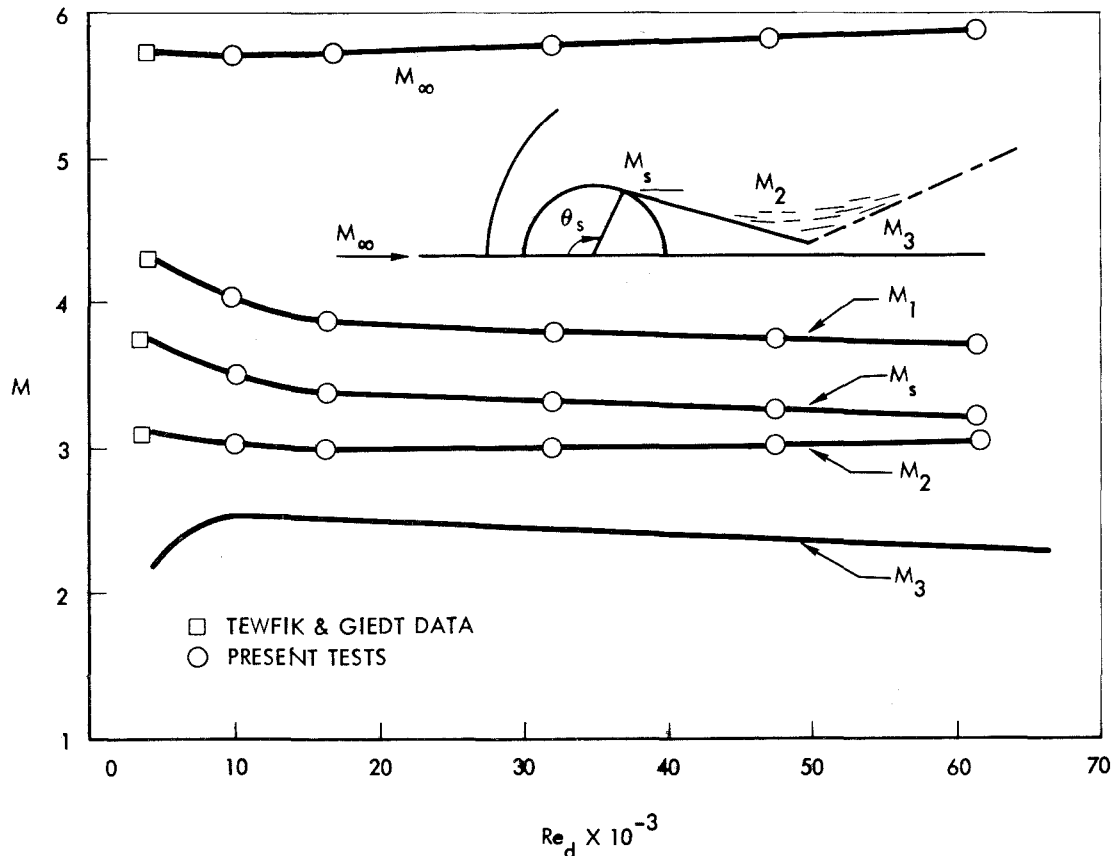
Figure 38.   Mach Number Versus Reynolds Number

Both the pitot- and static-pressure gradients are high in the neck region; however, the Mach number at the edge of the wake is relatively constant. Also, the precise axial location of the neck is unknown. Therefore, the static pressure, p_3, was obtained using the calculated value of M_3 and the experimental value of the pitot pressure at the axial stations of interest. These data were then used to obtain the extrapolated curves shown in Figure 21. In Table III, the effective wake growth at the neck, ϵ, is negative in most cases because the flow is accelerating in this region.

NECK WIDTH AND NECK DRAG

As will be discussed in Section V, the value of the momentum thickness and wake width at the neck must be known as initial conditions for theoretical analyses. Lees and Hromas (Reference 10) have estimated these quantities and shown that they should vary as $(R_{e_d})^{-1/2}$ based on estimates of skin friction around the body and the pressure rise at the neck. Experimental values are shown in Figure 58 based on the present tests. In Figure 39, 11 points are shown corresponding to the combinations of cylinder diameter and Reynolds number given in Table I. The wake width was obtained from pitot-pressure measurements and the momentum thickness was calculated from experimental data. The axial location of the neck was taken at $x/d = 2.50$ for the 0.300-inch diameter cylinder and $x/d = 3.00$ for the other models (Table III). Figure 39 shows that these quantities do vary as $(R_{e_d})^{-1/2}$. The scatter of Figure 39 is probably due to the effect of the velocity gradient on pitot measurements discussed in Section II.
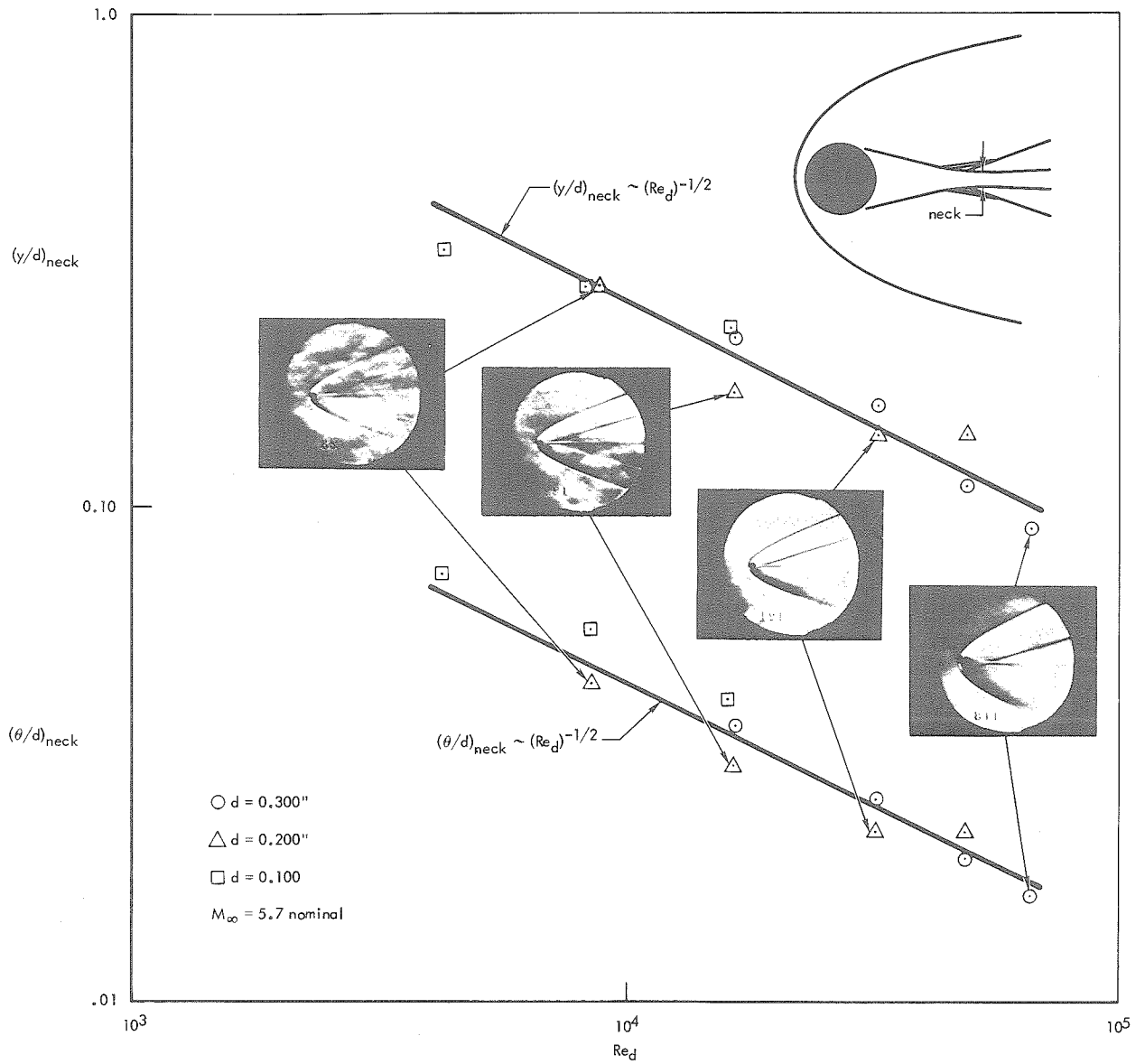
Figure 39.   Wake Width and Momentum Thickness at Neck

Marson and Lilley (Reference 30) have shown this to be on the order of

0.18 times the outside diameter of the pitot probe—approximately 0.007

inch in the case under discussion (Figure 6). Also, the exact axial

location of the neck, which varies with Reynolds number, was not known

(Table III).

V. THEORETICAL CONSIDERATIONS AND COMPARISON WITH EXPERIMENT

DEFINITION OF WAKE EDGE

Before the laminar wake can be treated theoretically, the edge conditions of the wake must be known--either from inviscid flow field calculations or from experiments (Appendix D). In the case under discussion, several exploratory computations were made to determine the best definition of the wake edge. It was finally concluded that the wake edge as seen from the pitot-pressure profiles was the best definition of this nebulous quantity.

For its determination, the intersection of the Gaussian-type, pitot-pressure profile with the inviscid outer wake was selected from the experimental data. A typical pitot-pressure profile, where this intersection is fairly well defined, is shown in Figure 9a. It was extremely difficult to define the wake edge for the turbulent wake (Figure 9b) from this program's experimental data. Therefore, the hot-wire-anemometry data of Demetriades (Reference 11) was used to define the wake edge in the turbulent region. Wake widths are shown in Figure 40. For $x/d < 6$, the wake is still undergoing internal adjustment processes; therefore, no simple similarity has yet been established. This adjustment is evident in the wake widths shown in Figure 40.
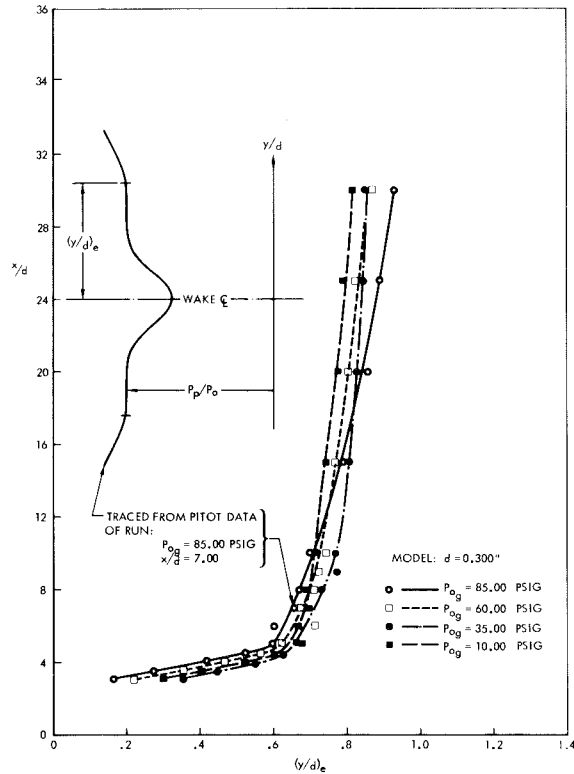
(a) 0. 300 Inch Diameter Cylinder
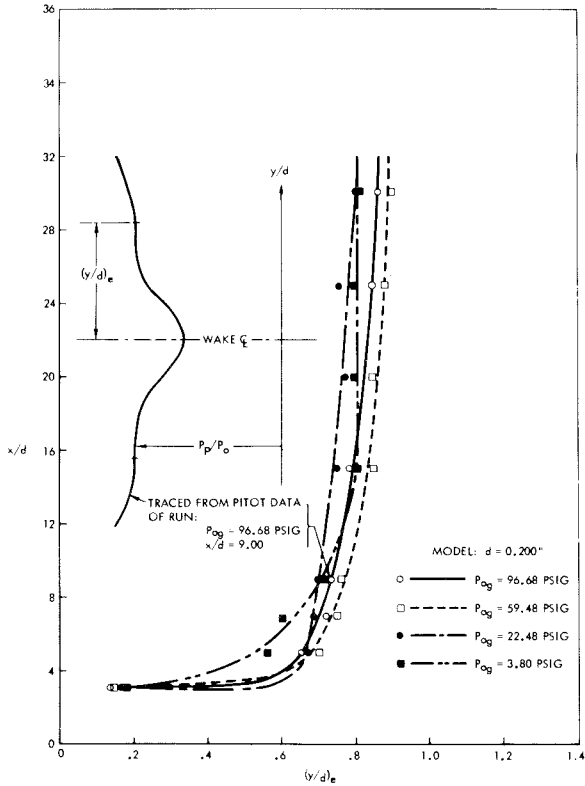
(b) 0. 200 Inch Diameter Cylinder
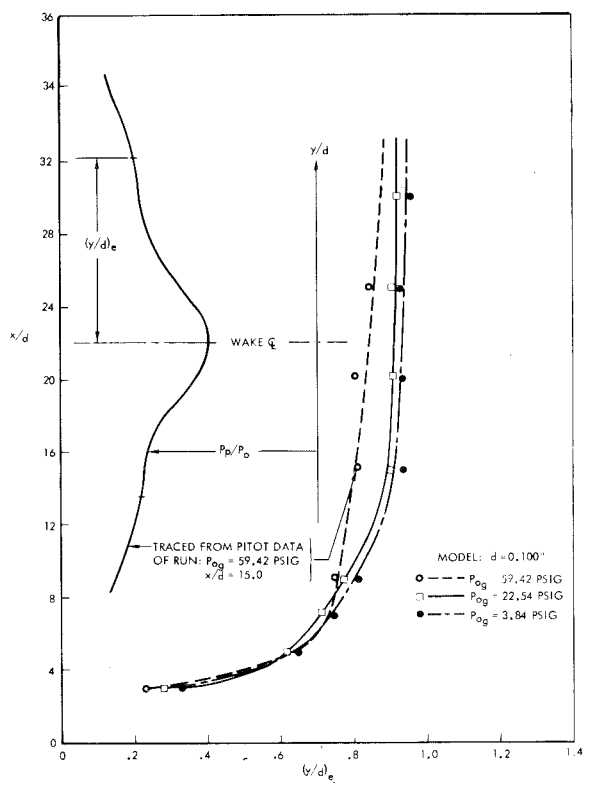
(c) 0. 100 Inch Diameter Cylinder

Figure 40.   Experimental Wake Widths

LAMINAR WAKE

As shown in Appendix C, the governing linearized equations for the static-enthalpy excess and velocity defect in a laminar wake with streamwise pressure gradient are

$$\frac{\partial}{\partial \bar{x}} \left(\frac{h}{h_e} - 1 \right) = \frac{1}{\sigma} \frac{\partial^2}{\partial \bar{y}^2} \left(\frac{h}{h_e} - 1 \right) \tag{10}$$

$$\frac{\partial}{\partial \bar{x}} \left(M_e^2 w \right) + G \frac{dM_e}{d\bar{x}} = \frac{\partial^2}{\partial \bar{y}^2} \left(M_e^2 w \right) \tag{11}$$

where the transformed coordinates are defined as

$$\bar{x} = \int_0^x \frac{\rho_e \mu_e u_e}{\rho_\infty \mu_\infty u_\infty} \frac{dx}{d} \tag{12}$$

$$\bar{y} = \frac{u_e}{u_\infty} \sqrt{Re_d} \int_0^y \frac{\rho}{\rho_\infty} \frac{dy}{d} \tag{13}$$

and the subscript $(\ )_e$ refers to the edge conditions. The static enthalpy excess can also be written in terms of the total enthalpy excess, G.

$$\frac{h}{h_e} - 1 = (\gamma - 1) M_e^2 w + \left(1 + \frac{\gamma - 1}{2} M_e^2 \right) G \tag{14}$$

where

$$G \equiv \frac{H}{H_e} - 1 \tag{15}$$

Equation 14 allows for the solution of G after the static enthalpy excess and velocity defect are known. It should be noted that the only assumption of the above analysis are the usual boundary-layer approximations and that $w \ll 1$. The Prandtl number, σ, is assumed to be constant, but it can be any value--not necessarily equal to one.

Since for our case the total enthalpy excess in the wake,

$$G \ll w \qquad (16)$$

Equation 11 can be simplified to read

$$\frac{\partial}{\partial \bar{x}} \left(M_e^2 w \right) = \frac{\partial^2}{\partial \bar{y}^2} \left(M_e^2 w \right) \qquad (17)$$

The assumption that $G \ll w$ is true only if there is little heat transfer. For actual reentry, this assumption may not be valid, and the exact integral solution given by Kubota (Reference 18) would have to be used. Equations 10 and 17 can be recognized as the simple heat diffusion equation; therefore, because the boundary conditions are homogeneous, simple closed-form solutions can be obtained if the initial conditions at the neck are assumed to be delta functions. These solutions are

$$\frac{h}{h_e} - 1 = \frac{B}{\sqrt{\bar{x}}} e^{-\frac{\sigma \bar{y}^2}{4\bar{x}}} \qquad (18)$$

$$M_e^2 w = \frac{A}{\sqrt{\bar{x}}} e^{-\frac{\bar{y}^2}{4\bar{x}}} \qquad (19)$$

It should be noted that the static-enthalpy excess is similar regardless of the value of the heat transfer. The constants A and B can be determined from the initial drag in the wake (not necessarily at the neck) and the heat transfer from the body to the fluid.

$$A = 1/2 \sqrt{\frac{Re_d}{\pi}} \left(\frac{\rho_e u_e \theta}{\rho_\infty u_\infty d} M_e^2 \right)_0 \qquad (20)$$

$$Q = 2 \rho_\infty u_\infty d \sqrt{\frac{\pi}{Re_d}} \left(\frac{B}{\sqrt{\sigma}} h_{e_0} - \frac{u_{e_0}^2}{M_{e_0}^2} A \right) \qquad (21)$$

where θ is the momentum thickness and the subscript $(\ )_0$ refers to the initial conditions (usually taken at the neck).

Experimental comparison of the simplified laminar-wake theory for the normalized distributions of velocity, static enthalpy, and total enthalpy are shown for three stations in Figure 41. It can be seen from Figure 41 that the assumption of a delta function as the initial condition affects the theoretical solutions; therefore, a satisfactory experimental check is not obtained until about 15 diameters downstream of the center of the cylinder.

The experimental check of total enthalpy is exceptionally good at $x/d = 15$ because the tail portions of the velocity and static enthalpy curves (which do not compare favorably with experiment), tend to cancel out.

Gold (Reference 41) has shown that for initial Gaussian velocity and enthalpy distributions of the form
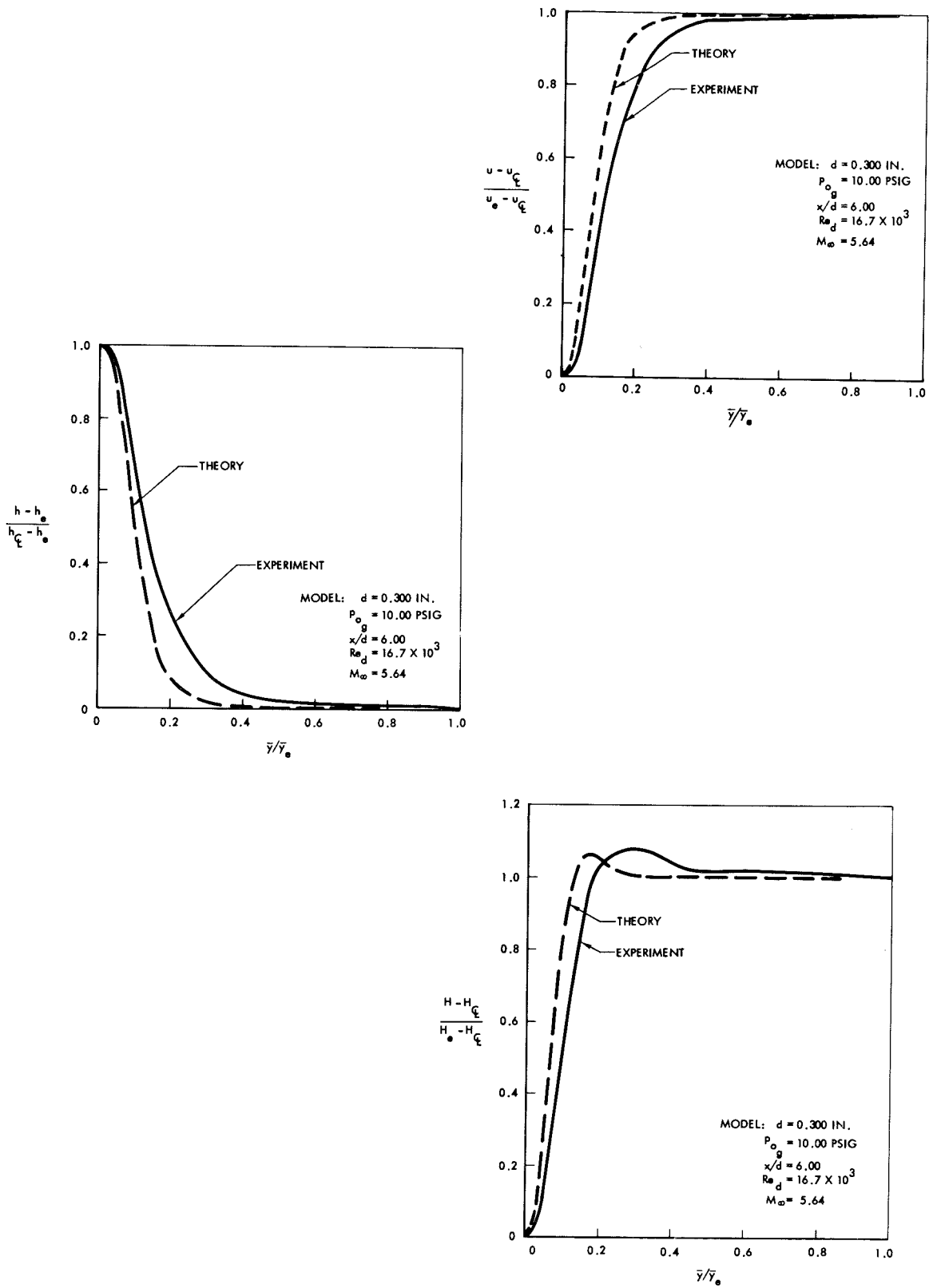
Figure 41a. Comparison of Theory and Experiment---Simplified
Laminar Theory: x/d = 6.00
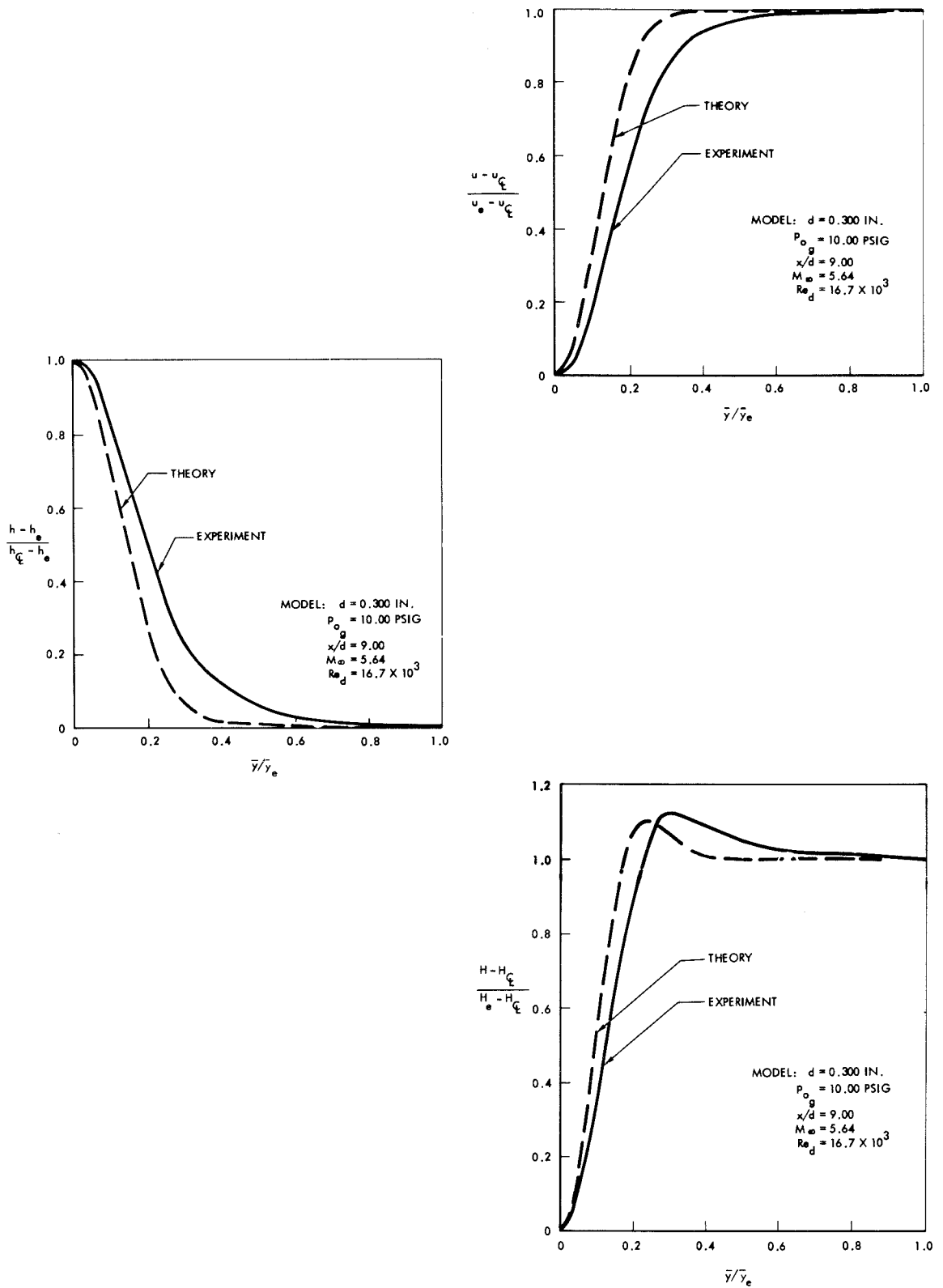
Figure 4lb. Comparison of Theory and Experiment---Simplified
Laminar Theory: x/d = 9.00
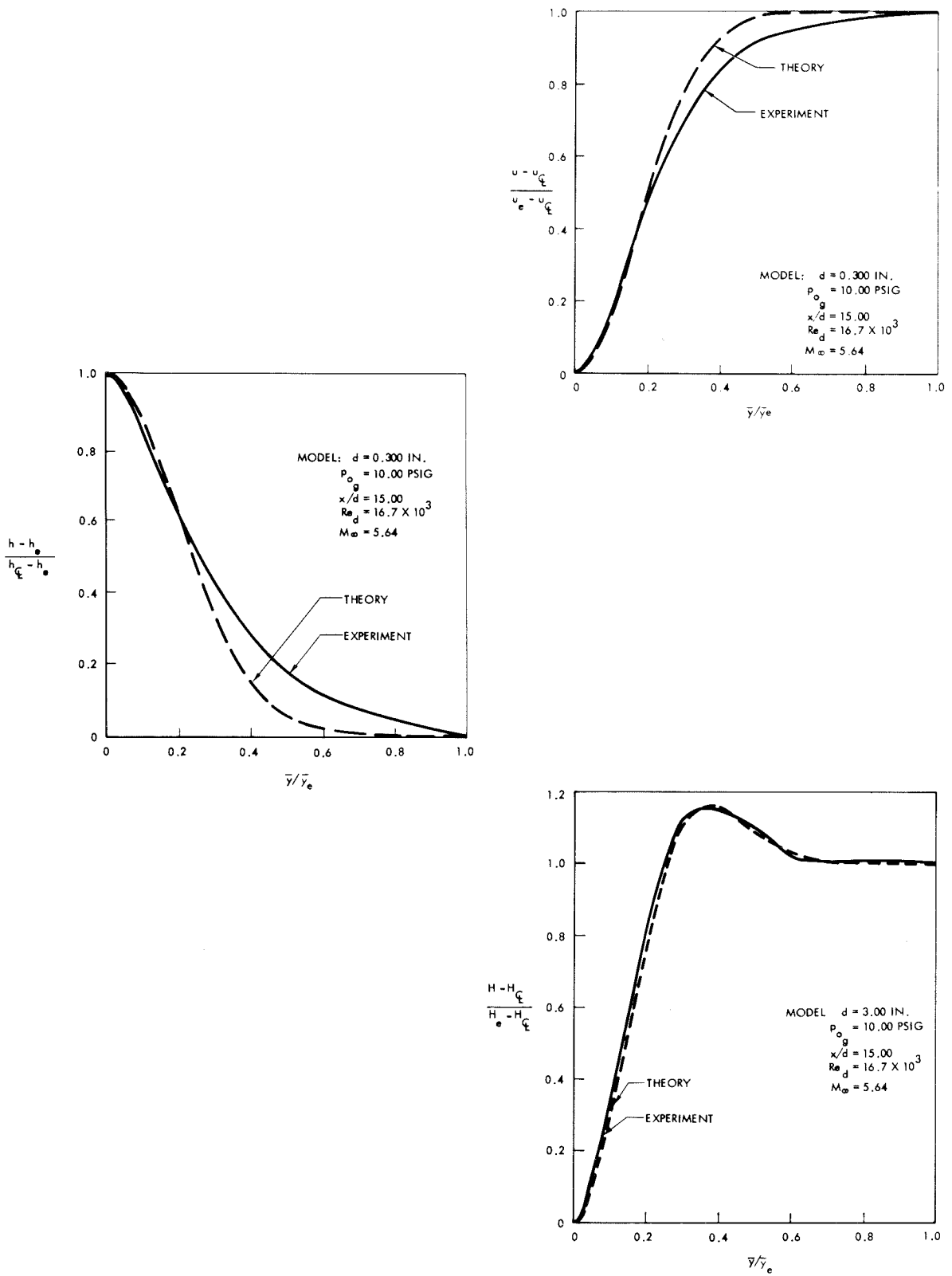
Figure 41c. Comparison of Theory and Experiment---Simplified
Laminar Theory: x/d = 15.00

$$w_0(\bar{y}) = A' e^{-\alpha \bar{y}^2} \tag{22}$$

$$\frac{h_0}{h_e} - 1 = B' e^{-\beta \bar{y}^2} \tag{23}$$

the problem of the laminar wake with streamwise pressure gradient can be dealt with theoretically by putting an initial delta function velocity distribution at a distance $\bar{x}_0 = \frac{1}{4\alpha}$ upstream of the origin and an initial delta function enthalpy distribution at a distance $\bar{x}_0 = \frac{\sigma}{4\beta}$ upstream of the origin. These results are equivalent to matching the initial distributions by suitable choice of $\bar{x}_0$.

Typical distributions of normalized static enthalpy and normalized velocity are shown in isoaxiometric form in Figure 42, where a non-zero value of $\bar{x}_0$ was used. In Figure 42 the change in shape of the normalized quantities from a Gaussian to a parabolic distribution at transition is evident. In Figure 43, a more practical scheme of non-dimensionalization, which does not depend on the wake "edge" is used for the abscissa. The results of Figure 43 are encouraging, considering the many varied inputs needed to obtain the experimental results. "Universal" curves of normalized static enthalpy and normalized velocity are indeed possible.

Values of the state properties along the wake centerline as predicted by the theory are also very good. The constants A and B were calculated according to Equations 20 and 21 for each case. Comparison of theory and experiment was within 10 percent for all cases. A typical calculation of the constants A and B is shown in Figures 44 and 45. To obtain the heat
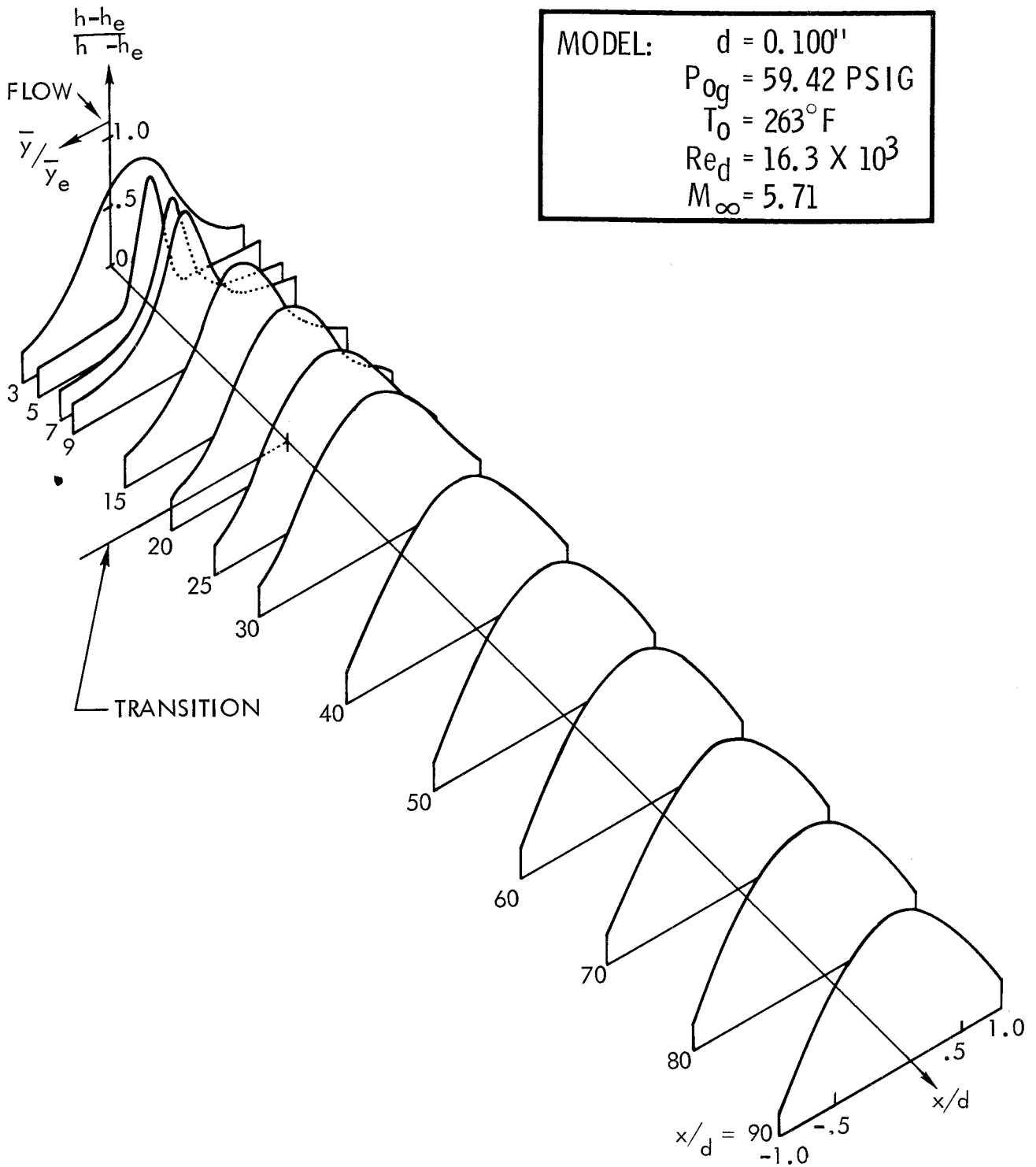
Figure 42. Typical Results
(a) Normalized Static Enthalpy
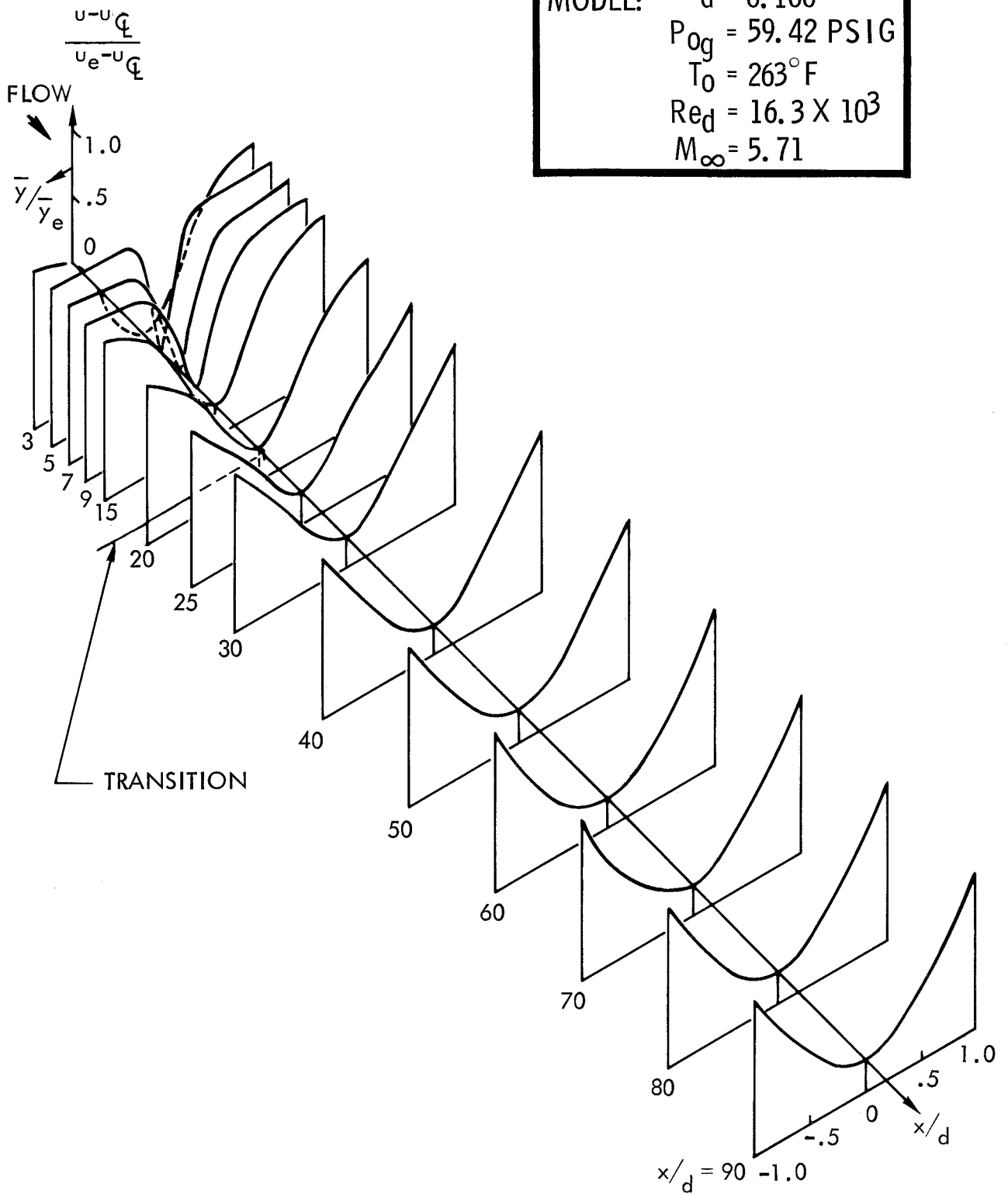
Figure 42. Typical Results
(b) Normalized Velocity
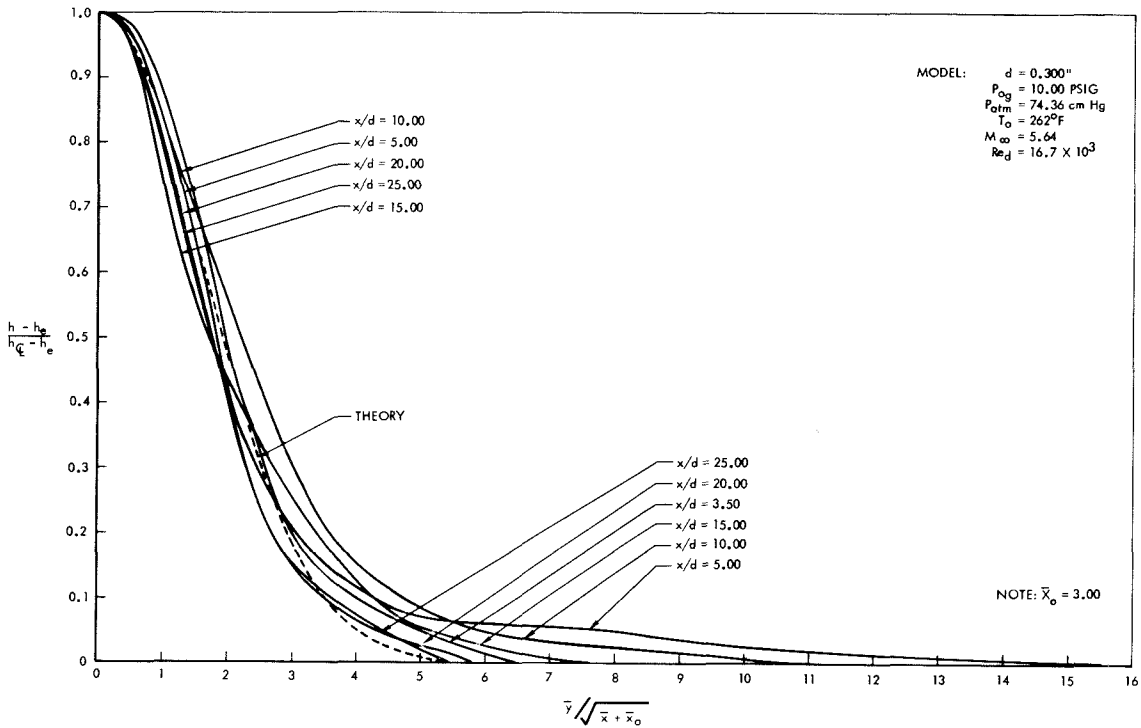
(a) Normalized Static Enthalpy, 0.300 Inch Diameter Cylinder
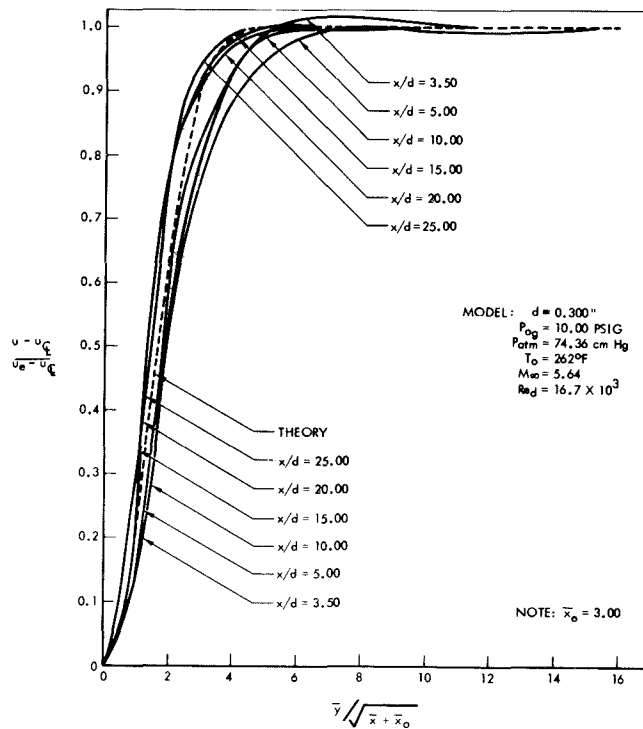
(b) Normalized Velocity, 0.300 Inch Diameter Cylinder

Figure 43. Comparison of Theory and Experiment-Laminar Theory
With Effective Origin

- 95 -
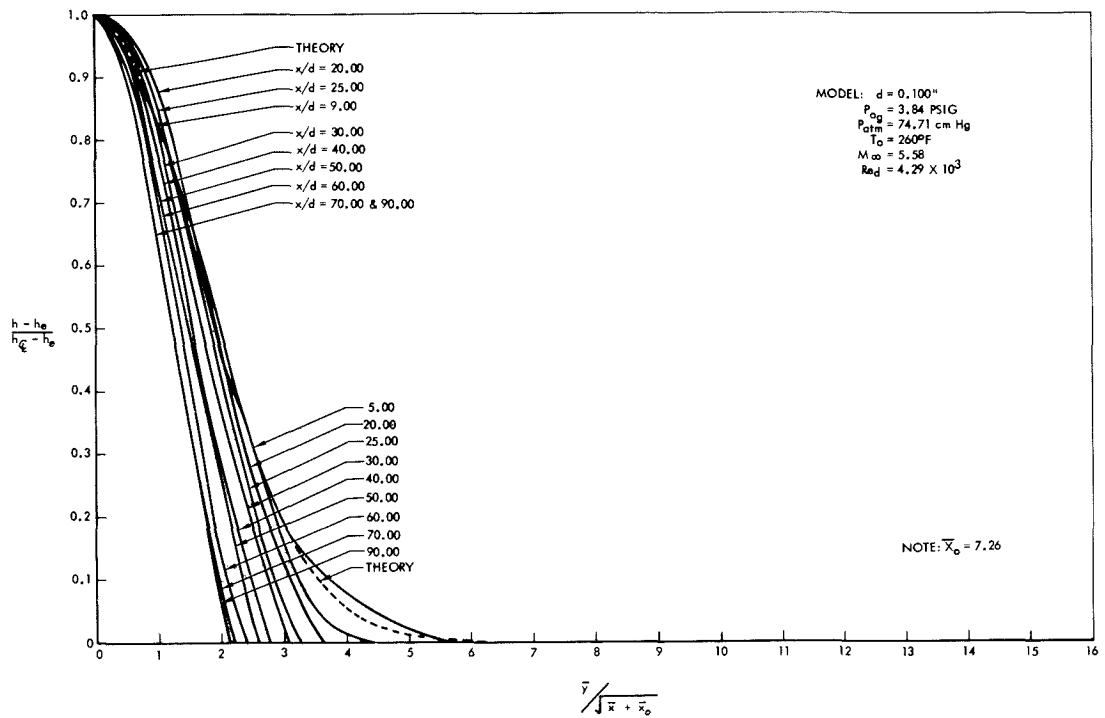
(c) Normalized Static Enthalpy, 0.100 Inch Diameter Cylinder
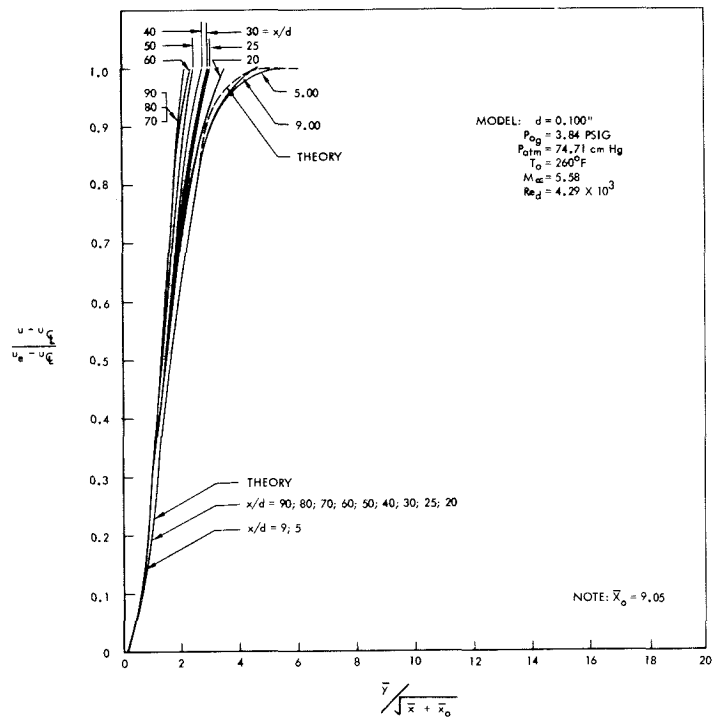
(d) Normalized Velocity, 0.100 Inch Diameter Cylinder

Figure 43. Comparison of Theory and Experiment-Laminar Theory
With Effective Origin
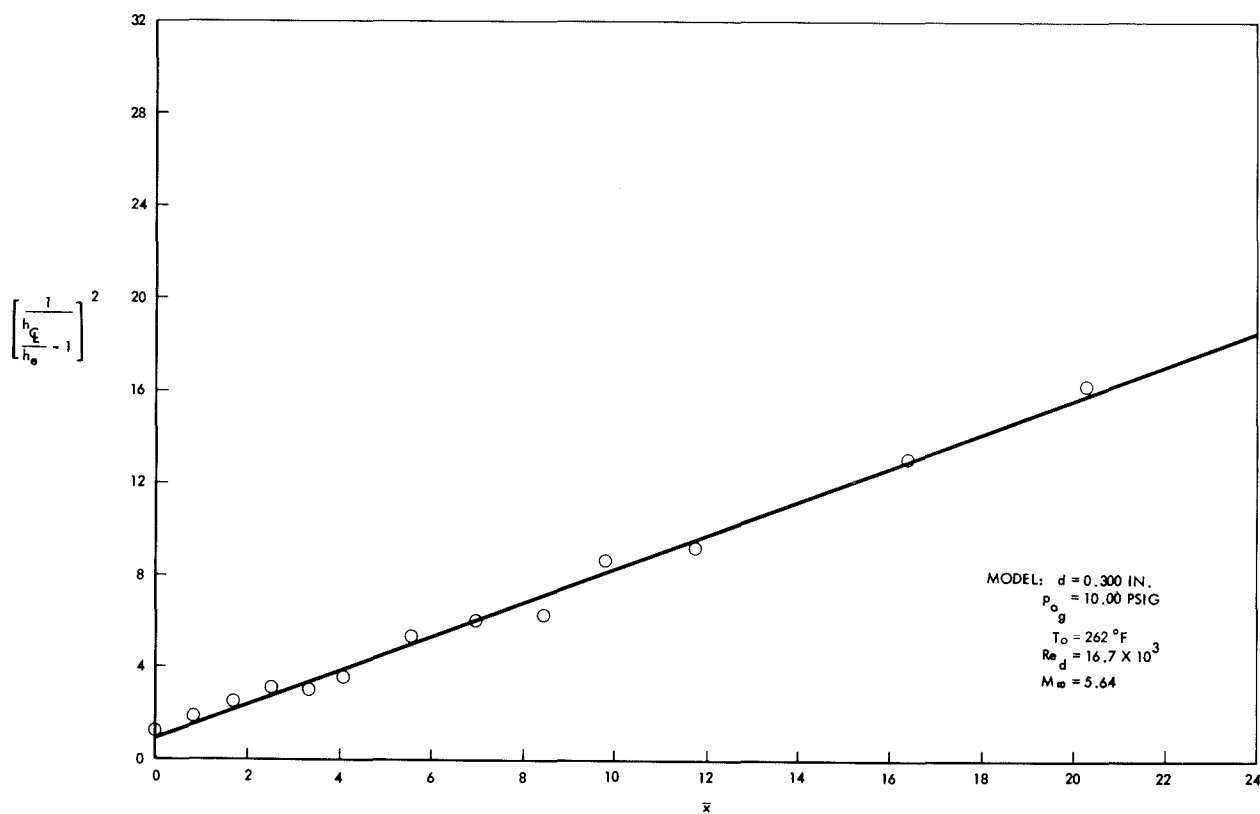
Figure 44. Axial Variation of Static-Enthalpy Excess
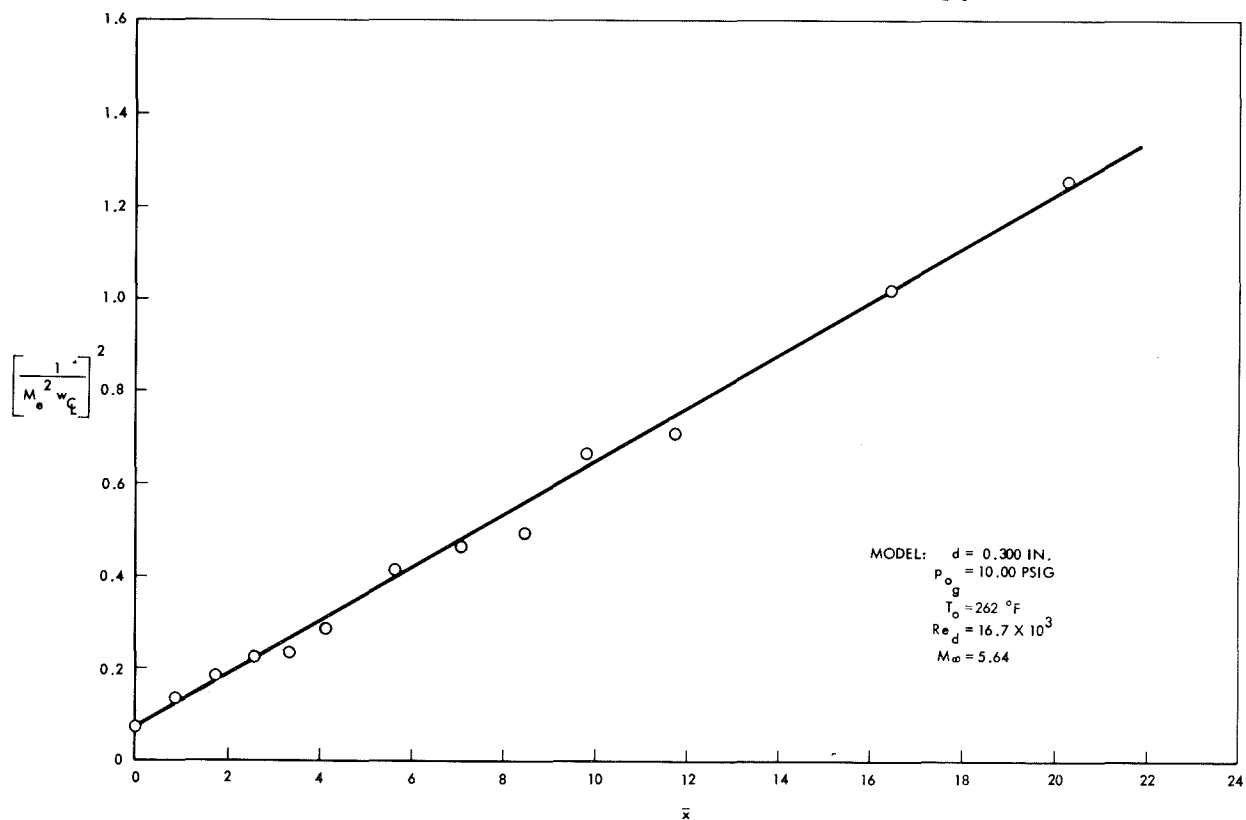
Figure 45. Axial Variation of Velocity Defect

transfer, the total enthalpy distribution was integrated across the wake.
If the centerline distributions of static-enthalpy excess and velocity defect
are plotted for all the runs of Table I, the data shown in Figures 46 and 47
are obtained.

Figures 46 and 47 show that there is definitely a Reynolds number
correspondence for the laminar theory. The two runs which do not corre-
spond with the base line are fully turbulent. It should be noted that the
static-enthalpy excess and the velocity defect for the turbulent case also
varies as $(R_{e_d})^{-1/2}$ when turbulence is fully established. Figures 46 and
47 can also be used as a measure of transition. At transition, the values
of velocity defect and static-enthalpy excess decrease much more rapidly
than for the laminar case because of the more efficient mixing processes.
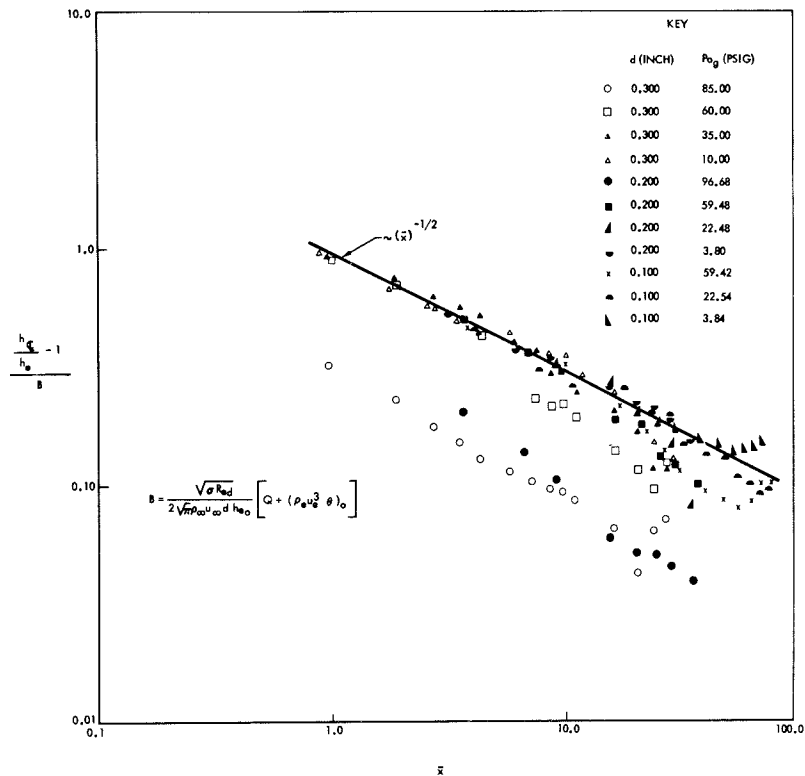
Figure 46. Static-Enthalpy Excess Along Wake Centerline
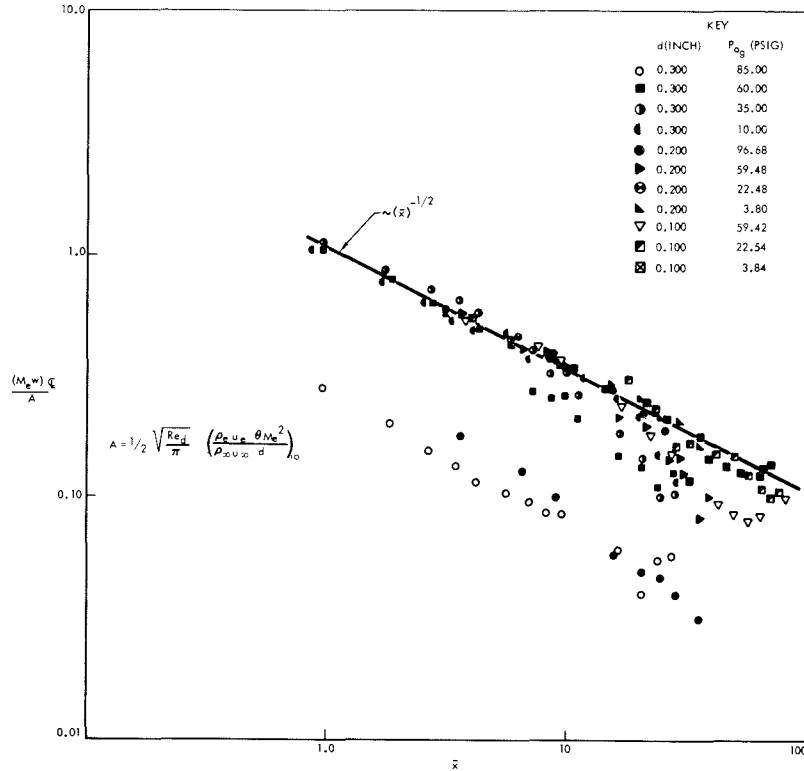
Figure 47. Velocity Defect Along Wake Centerline

Appendix D shows the momentum thickness as predicted by the

simplified theory is constant if modified by the edge conditions

$$\frac{\theta}{\theta_0} = \frac{\left(\rho_e u_e M_e^2\right)_0}{\rho_e u_e M_e^2} \qquad (24)$$

To compare this aspect of the theory with experiment, Figure 48 was

drawn where a typical laminar case is presented. The experimental point

on the extreme right is in a region of turbulent flow. As discussed in the

previous portion of this section, the wake is "adjusting" until x/d = 6.

There was no similarly satisfactory correlation of momentum-thickness

data possible for the turbulent cases.

$$\frac{\theta}{\theta_o}\left[\frac{\rho_e\ u_e\ M_e^2}{\left(\rho_e\ u_e\ M_e^2\right)_o}\right]$$
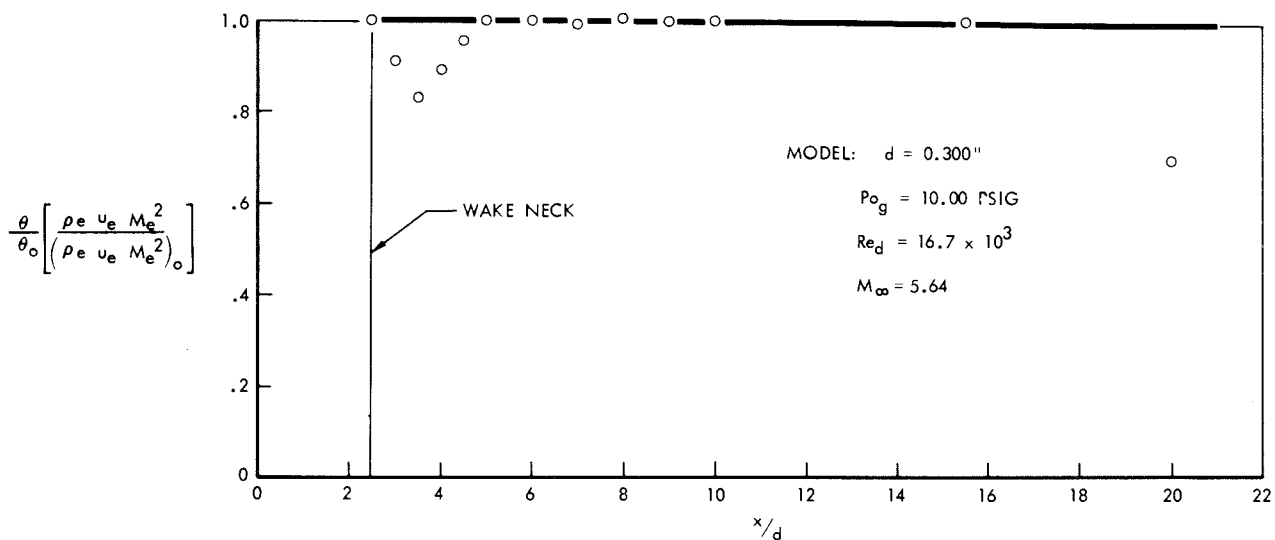
Figure 48. Momentum Thickness

Also, as discussed in Appendix D, the laminar wake width can be predicted theoretically,

$$\frac{\rho_e\ u_e}{\rho_\infty\ u_\infty}\ \frac{\delta}{d}\sqrt{R_{e_d}}\ =\ \Delta + (\gamma - 1)\left(M_e^2\ \frac{\rho_e\ u_e}{\rho_\infty\ u_\infty}\ \frac{\theta}{d}\ \sqrt{R_{e_d}}\right)_0 \qquad (25)$$

where

$$\Delta^2\ =\ \bar{x}\ \ln\frac{N}{2}\sqrt{\frac{R_{e_d}}{\pi}}\left(\frac{\rho_e\ u_e\ \theta}{\rho_\infty\ u_\infty d}\ M_e^2\right)_0 - \bar{x}\ln M_e^2\sqrt{\bar{x}} \qquad (26)$$

Comparison of experimental and theoretical laminar wake widths is shown in Figure 49. Again, the experimental point on the extreme right is in a turbulent region. N = 100 means that, for the theory, the edge of the wake
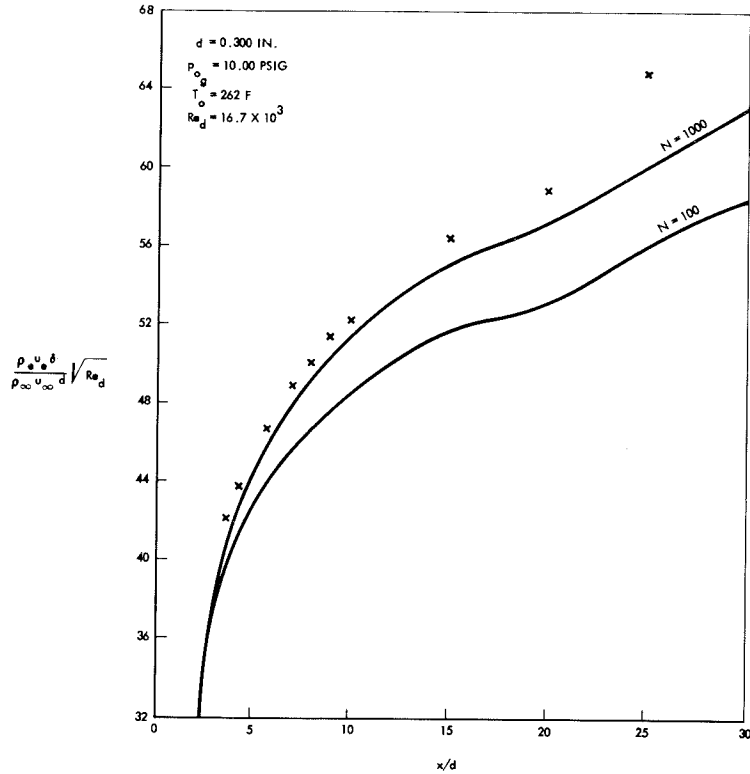
Figure 49. Theoretical and Experimental Wake Thickness

was assumed to be at the point where the wake velocity = 0.99 u_e; N = 1000

means that the wake velocity = 0.999 u_e. Comparison between theory and

experiment is surprisingly good, considering the nebulous nature of the

wake width.

TURBULENT WAKE

The turbulent wake has been adequately treated theoretically by Lees

and Hromas (Reference 10); therefore, only a few general remarks will be

made here. The theory presented in Reference 10 is depicted graphically in

Figure 50. Physically, it can be thought of as the penetration of an inviscid

static-enthalpy profile by a turbulent boundary layer with initial width and

momentum thickness.
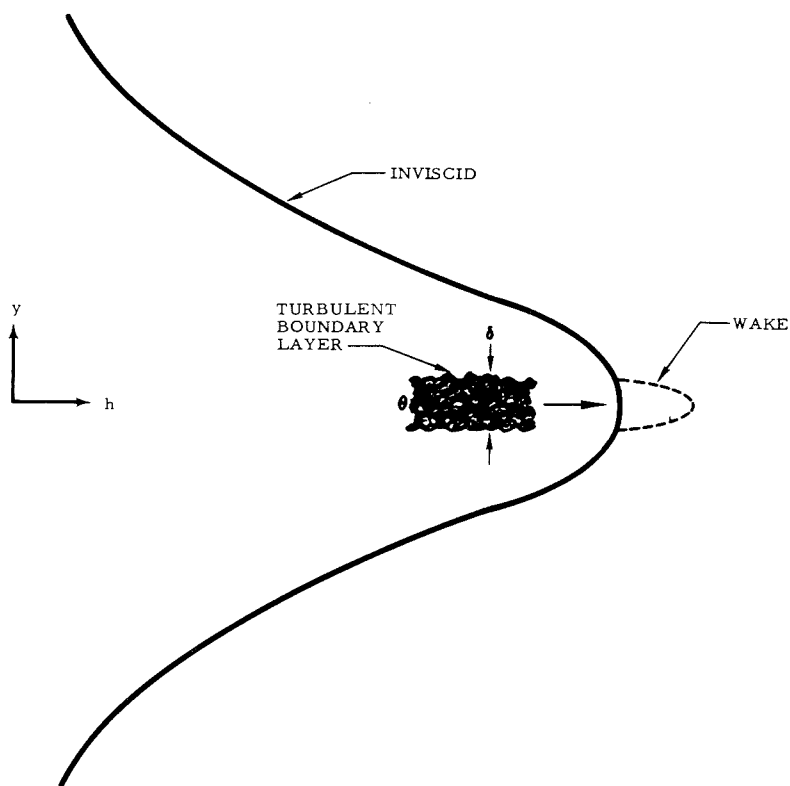
Figure 50. Theory of Lees and Hromas

Lees and Hromas (Reference 10), in order to obtain a definite inter-

section of the wake static-enthalpy profile with the static inviscid-enthalpy

profile, assume that the static enthalpy distribution in the wake is parabolic.

Integral methods are then used to solve the turbulent boundary-layer

equations; thus, any definition of the distributions--except those originally

assumed--are not products of theory. However, some assumption had to

be made concerning the turbulent diffusivity at the centerline of the wake.

They assumed that Townsend's (Reference 4) "universal" Reynolds number

for incompressible flow behind circular cylinders is also valid for the

hypersonic case. In particular, for the two-dimensional case, they

asserted a constant value across the turbulent wake for

$$R_{e_T} = \frac{\Delta u \, Y_T}{\tilde{\epsilon}_T} \tag{27}$$

where

$\Delta u = u_e - u_{\mathcal{C}}$

Y_T is the Howarth-Dorodnitsyn variable for the wake edge $\int_o^{y_e} \frac{\rho}{\rho_\infty} dy$

$\tilde{\epsilon}_T$ is the equivalent turbulent diffusivity

The total temperature in the wake was assumed to be constant in the theoretical treatment.

Comparison of the Lees and Hromas turbulent theory with the present experiments was not rewarding because experimental data were not obtained far enough downstream. The wake grew very slowly and little change in state properties was obtained. However, theoretical calculations were made for this case utilizing a program written at the Space Technology Laboratories by Hromas. Inputs to this program involve the inviscid static-enthalpy profile and initial conditions.

To obtain the static-enthalpy profile, the shock shape as obtained from schlieren photographs was approximated by the equations shown in Figure 51. As suggested by Lykoudis (Reference 17), the body was then omitted and the flow expanded from the pressure at the bow shock to the ambient pressure in the free stream. The results of this calculation are shown in Figure 51. It should be noted that the slope of the inviscid static-enthalpy profile is very steep near the axis. Also of interest is the fact that, for $x/d > 9$, the static-enthalpy profile obtained in this manner checked satisfactorily with experiment and with inviscid-flow calculations.

EMPIRICAL $\begin{cases} y/d = 1.58\,(x/d)^{0.500} \; ; \; x/d \le 1 \\ y/d = 1.58\,(x/d)^{0.564} \; ; \; x/d \ge 1 \end{cases}$

EXPERIMENT

CYLINDER ₵ AT x/d = 0.720

x/d	y/d
0	0
0.0241	0.2191
0.0723	0.4130
0.1205	0.5354
0.2169	0.7301
0.3133	0.8824
0.4337	1.040
0.5542	1.177
0.6747	1.295
0.8193	1.430
0.9639	1.555
1.205	1.746
1.446	1.925
1.928	2.263
2.410	2.566
3.133	2.986
3.855	3.376

MODEL: d = 0.300 IN.
P_{O_g} = 85.00 PSIG
P_{ATM} = 74.69 CM Hg
T_O = 263°F
M_∞ = 5.69

(a) Shock Shape

$g = \dfrac{\dfrac{h}{h_\infty} - 1}{\dfrac{h_{₵}}{h_\infty} - 1}$

$Y_L = \int_0^{\frac{y}{d}} \dfrac{\rho}{\rho_\infty} \, d\left(\dfrac{y}{d}\right)$
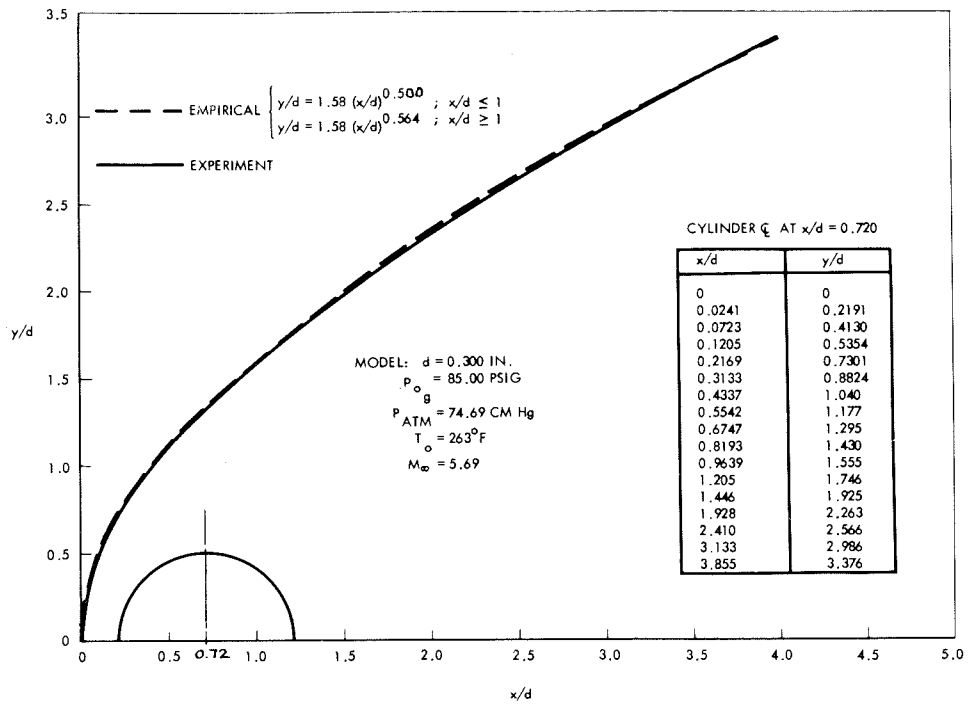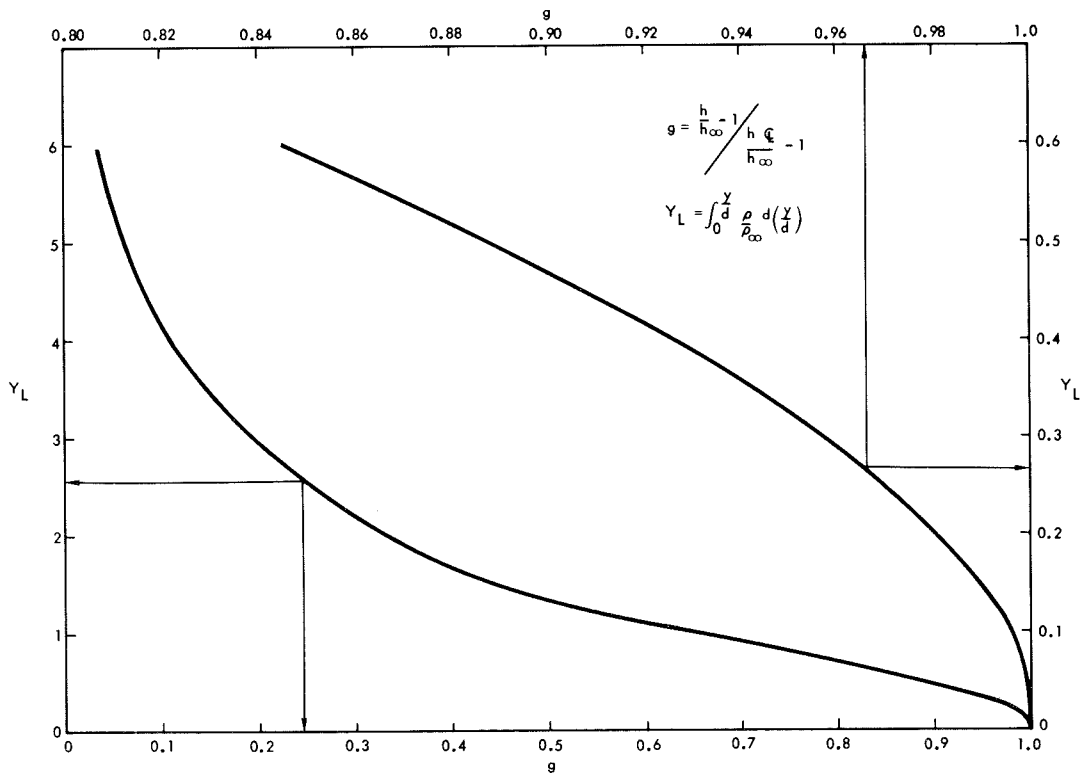
(b) Inviscid Static Enthalpy Profiles

Figure 51. Experimental Shock Shape With
Derived Static-Enthalpy Profiles
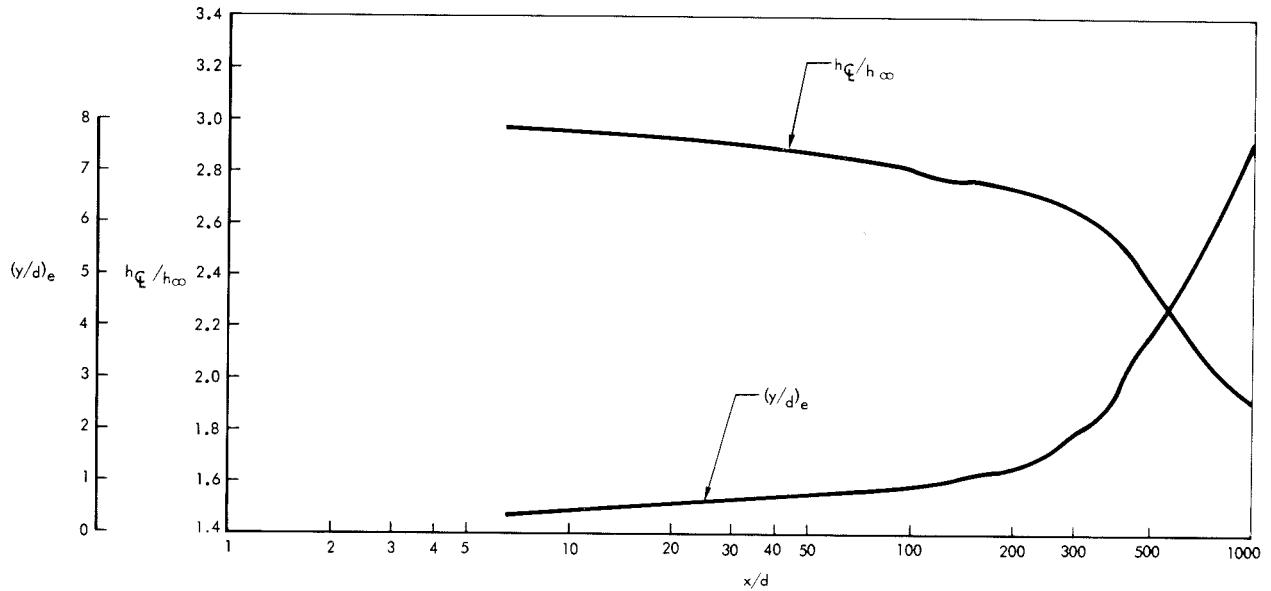
Figure 52. Theoretical Turbulent Wake Growth

The results of the Hromas program are shown in Figure 52 which plots the static-enthalpy ratio and wake width. Figure 52 shows that the swallowing process does not become effective until about 300 diameters downstream of the body because of the nature of the inviscid static-enthalpy profile. This result was predicted by Lees and Hromas (Reference 10) based on an approximate form of their final results.

VI.   TRANSITION

"UNIVERSAL" TURBULENT REYNOLDS NUMBER

As discussed in the previous section, Lees and Hromas (Reference 10) assumed the Townsend value of "universal" turbulent Reynolds number of 12.5 for the centerline conditions in the turbulent wake.   To investigate this assumption experimentally, consider the momentum equation

$$\rho\, u \frac{\partial u}{\partial x} + \rho v \frac{\partial u}{\partial y} = -\frac{\partial p}{\partial x} + \frac{\partial}{\partial y} \left(\rho \epsilon_T \frac{\partial u}{\partial y} \right) \tag{28}$$

at the centerline

$$\rho_{\mathbb{C}}\; u_{\mathbb{C}} \left(\frac{\partial u}{\partial x} \right)_{\mathbb{C}} + \frac{\partial p}{\partial x} = \rho_{\mathbb{C}} \left(\epsilon_T \right)_{\mathbb{C}} \left(\frac{\partial^2 u}{\partial y^2} \right)_{\mathbb{C}} \tag{29}$$

With

$$w = 1 - \frac{u}{u_e} \tag{30}$$

then

$$-\rho u_{\mathbb{C}}\, u_e \left(\frac{\partial u}{\partial x} \right)_{\mathbb{C}} + \frac{\partial p}{\partial x} = -\rho \left(\epsilon_T \right)_{\mathbb{C}} u_e \left(\frac{\partial^2 w}{\partial y^2} \right)_{\mathbb{C}} \tag{31}$$

To obtain $\dfrac{\partial^2 w}{\partial y^2}$ experimentally without the employment of doubtful means would be very inaccurate, because this quantity involves two
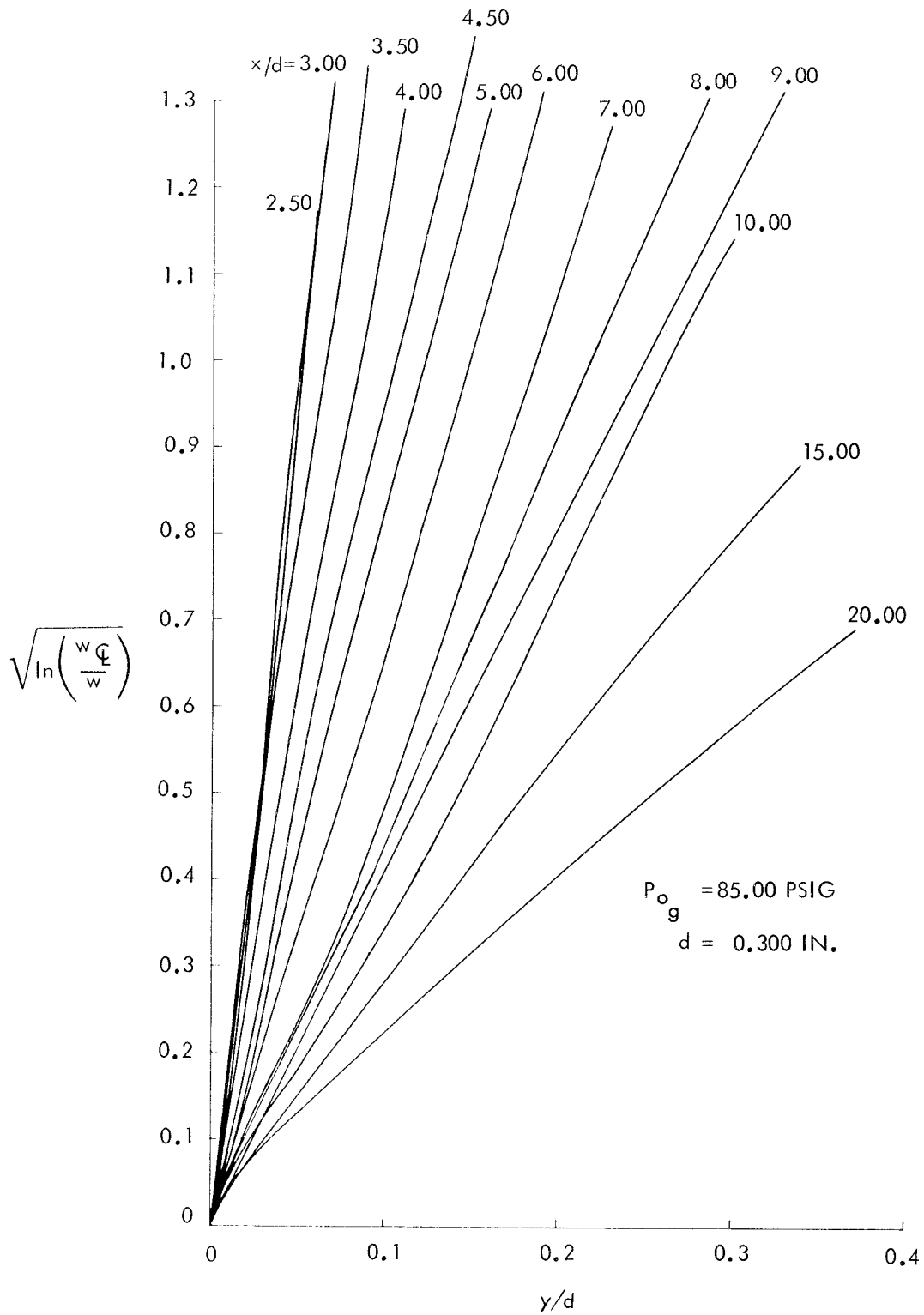
Figure 53. Diffusivity Parameter Variation

differentiations of experimental data. Therefore, the method first proposed by Kingsland (Reference 13) to reduce diffusion measurements was used. Assuming

$$\frac{w}{w_{\text{\pounds}}} = 1 - a y^2 + - - - \tag{32}$$

then

$$\frac{\partial^2 w}{\partial y^2} = - 2 a w_{\text{\pounds}} + - - - \tag{33}$$

and expanding the logarithm of Equation 31.

$$\frac{\ln \frac{w}{w_{\text{\pounds}}}}{y^2} = - a \tag{34}$$

giving

$$\left(\frac{\partial^2 w}{\partial y^2} \right)_{\text{\pounds}} = - \frac{2 w_{\text{\pounds}}}{D_N} \tag{35}$$

where the diffusivity number is defined by

$$D_N = \lim_{y \to o} \frac{y^2}{\ln \frac{w_{\text{\pounds}}}{w}} \tag{36}$$

The experimental plots of the diffusivity parameter $\sqrt{\ln \frac{w_{\text{\pounds}}}{w}}$ versus vertical distance are remarkably good (Figure 53). From these data, it was then possible to obtain the slope of the diffusivity parameter versus distance to calculate the diffusivity number discussed above. The diffusivity parameter was plotted in terms of transformed coordinates, but,

as expected, the results for the turbulent case became worse and those

for the laminar case better. (The transformed diffusivity number was

also used to give another indication of transition.)

To obtain experimental values of the Townsend Reynolds number via

Equation 31, it is necessary to differentiate two experimental quantities

which subtract from each other as well as the diffusivity number

discussed above. Therefore, the determination of this quantity is crude

at best. Other means of obtaining quantitive values of "universal"

Townsend turbulent Reynolds number would be more desirable, e. g.,

diffusion measurements. In any case, the tentative value, $Re_T = 10 \pm 5$,

was obtained. This value agrees very well with that used by Lees and

Hromas in their theoretical treatment ($Re_T = 12.5$). The results also

compare favorably with those of Kingsland (Reference 13) where he

estimated the value, $Re_T \cong 12$.

EXPERIMENTAL DETERMINATION OF TRANSITION

As indicated in the foregoing discussion, a qualitative definition of

transition could be obtained from plots of centerline state properties.

Another definition is possible by calculating the Townsend Reynolds

number discussed in this section.

Perhaps the best definition, however, is obtained from plots of

transformed diffusivity number versus axial distances (Figure 54). It

should be noted in Figure 54 that the value of transformed diffusivity

(a) Turbulent Case

MODEL:
$d = 0.300''$
$P_{og} = 85.00$ PSIG
$T_o = 263°F$
$Re_d = 66.5 \times 10^3$
$M_\infty = 5.69$

$$\overline{D}_n = \frac{(\overline{y})^2}{Ln\left(\frac{W_\mathbb{C}}{W}\right)}$$

(b) Transition Case

TRANSITION

MODEL:
$d = 0.300''$
$P_{og} = 35.00$ PSIG
$T_o = 262°F$
$Re_d = 32.7 \times 10^3$
$M_\alpha = 5.71$

$$\overline{D}_n = \frac{(\overline{y})^2}{Ln\left(\frac{W_\mathbb{C}}{W}\right)}$$

(c) Laminar Case

MODEL:
$d = 0.200''$
$P_{og} = 3.80$ PSIG
$T_o = 260°F$
$Re_d = 8.58 \times 10^3$
$M_\infty = 5.57$

$$\overline{D}_n = \frac{(\overline{y})^2}{Ln\left(\frac{W_\mathbb{C}}{W}\right)}$$
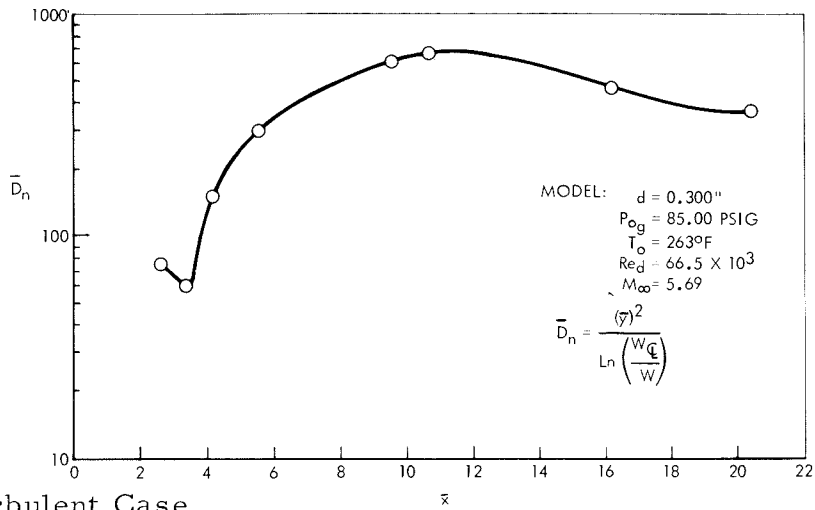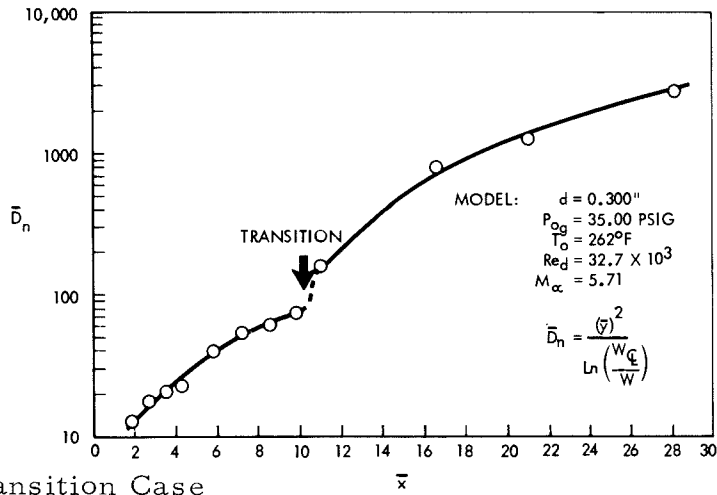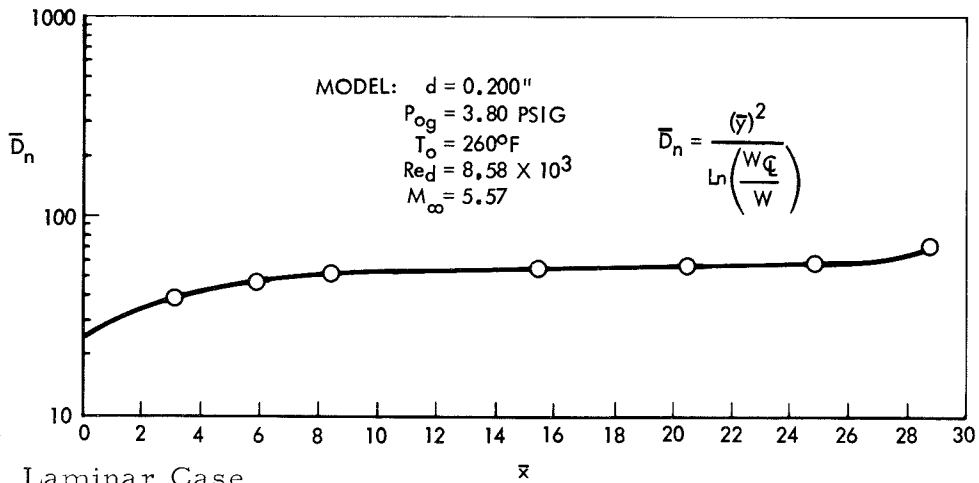
Figure 54.   Transformed Diffusivity Number
Versus Transformed Axial Distance

number in the turbulent region is much higher than for the laminar case. (In Figure 54a, Demetriades, Reference 11, found transition for these conditions near the neck, but no data point was claimed here.)

Using all available inputs, the results for these tests are superimposed on those of Demetriades (Reference 11) in Figure 55. For the 11 runs shown in Table I, seven transition points could be obtained—two cases being fully laminar and two cases fully turbulent. The comparison with Demetriades' data is surprisingly good. Since the edge properties could be determined with the present measurements, it was possible to define a transition Reynolds number based on local conditions and distance from an effective origin. Its value was calculated as 85,000.

Some question may arise as to the mechanism of transition, because some difficulty has been experienced in obtaining laminar flow by other investigators. In anticipated rebuttal, it should be pointed out that Demetriades' data (shown in Figure 55) is a combination of several different-sized cylinders at several different axial locations in the wind tunnel. In addition, the regimes were confirmed by Kingsland's data (Reference 13) wherein diffusion measurements were employed to investigate a fully turbulent and a fully laminar wake. Demetriades (Reference 26) has also successfully correlated the data of Slattery and Clay (Reference 42) on the present plot.

Conclusive proof of the self-induced nature of the transition in the wake would be presented by the experimental investigation of the
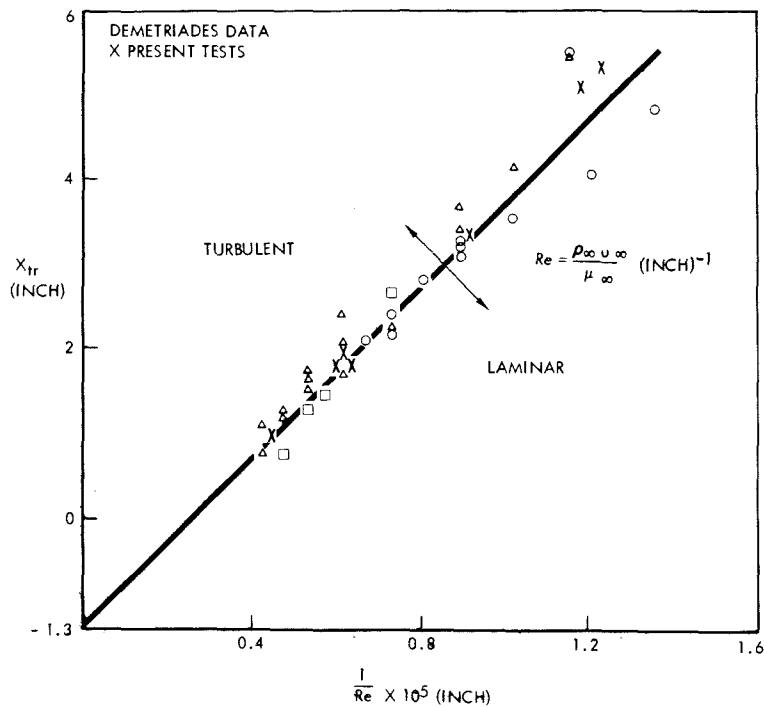
Figure 55. Transition

character of the boundary layer on the wind tunnel's side walls. This was

not done for the nozzle used in the testing reported here; however,

since the present program was initiated, a new nozzle has been installed

in Leg 1 of the GALCIT hypersonic wind tunnel; also, the boundary layer

on the wind tunnel's side walls has been surveyed for p_{o_g} = 35 psig.

The results of this survey show that transition of the boundary

layer on the side walls does not take place until 25 inches downstream

of the throat (Figure 3). In this respect, the previous nozzle should be

better than the new nozzle, because it was considerably shorter. In

the present tests, for the wind tunnel stagnation pressure of 35 psig,

transition took place 23. 1 inches downstream of the nozzle throat.

VII CONCLUSIONS AND SUGGESTIONS FOR FUTURE WORK

An experimental investigation has been made of the flow behind a circular cylinder at a nominal free-stream Mach number of 5.7. The Reynolds number was varied by changing both the diameter of the cylinder and the stagnation pressure of the wind tunnel -- the former over a three-fold range and the latter over a six-fold range. Enough measurements were made to completely define the flow field as far downstream as 90 diameters for the smallest cylinder and 30 diameters for the largest cylinder.

From these measurements, transition from laminar to turbulent flow was defined in the wake and successfully correlated with other data. A "universal" Reynolds number for transition based on edge conditions and the laminar length of the run was determined as 85,000.

Correlation of the experimental data with Kubota's theory (Reference 18) for laminar flow was then made. The theoretical prediction of center-line values of static enthalpy and local velocity based on this theory were in excellent agreement with the experimental results. Distributions of static enthalpy, and local velocity in the wake agree with the theory if provision is made for an "effective" origin based on the wake width at the neck. The theoretical predictions of wake width and momentum thickness are also in close agreement with the theory.

Because of the nature of the tests conducted, it was not possible to correlate the experimental data with the turbulent theory of Lees and Hromas (Reference 10) since only very small differences in state properties were available in the turbulent flow regime. However, a qualitative experimental value of the Townsend Reynolds number for turbulent flow on which the theory of Lees and Hromas is based was obtained. Its value was determined as $Re_T = 10 \pm 5$. In order to study the turbulent regime in more detail, it is necessary to either heat or cool the body. This project has already been started at GALCIT.

It is suggested that the theory be extended to account for real-gas and relaxation effects. Experimental verification could then be accomplished in facilities such as the hotshot and shock tunnel for the two-dimensional case. The laminar theory should then be extended to three-dimensions so that the wake properties behind an arbitrary body of revolution can be predicted with confidence for actual reentry conditions.

REFERENCES

1.   Goldstein, S. (editor), Modern Developments in Fluid Dynamics, Vol. II, Chapter XIII, Oxford University Press, London, 1938.

2.   Schlichting, H., Boundary Layer Theory, 4th Ed., McGraw-Hill Book Company, Inc., New York, 1960.

3.   Birkhoff, G. and Zarantonello, E.H., Jets, Wakes, and Cavities, Academic Press, Inc., New York, 1957.

4.   Townsend, A.A., The Structure of Turbulent Shear Flow, Cambridge University Press, London, 1956.

5.   Roshko, A., On the Drag and Shedding Frequency of Bluff Cylinders, NACA TN 3169, July 1954.

6.   Cooper, R.D. and Lutzky, M., Exploratory Investigation of the Turbulent Wakes Behind Bluff Bodies, The David W. Taylor Model Basin, Research and Development Report 963, October 1955.

7.   Jacchia, L.G., The Descent of Satellite 1957 Beta One, Special Report No. 15, Optical Satellite Tracking Program, Smithsonian Institution Astrophysical Observatory, July 20, 1958.

8.   Slattery, R.E. and Clay, W.G., Width of the Turbulent Trail Behind a Hypervelocity Sphere, Report 35 G-0004, M.I.T. Lincoln Laboratory, 6 June 1961.

9.   Dana, T.A. and Short, W.W., Experimental Study of Hypersonic Turbulent Wakes, Report ZPh-103, Convair, San Diego, May 29, 1961.

10.   Lees, L. and Hromas, L., Turbulent Diffusion in the Wake of a Blunt-Nosed Body at Hypersonic Speeds, Aerodynamics Department Report 50, Space Technology Laboratories, Inc., July 1961. Also, Institute of Aerospace Sciences paper No. 62-71, presented at the IAS 30th annual meeting, New York, New York, January 22-24, 1962.

11. Demetriades, A., Some Hot-Wire Anemometer Measurements in a Hypersonic Wake, Proceedings of the 1961 Heat Transfer and Fluid Mechanics Institute, Stanford University Press, 1961.

12. Mohlenhoff, W., Experimental Study of Helium Diffusion in the Wake of a Circular Cylinder at M = 5.8, GALCIT Hypersonic Research Project, Memorandum No. 54, May 20, 1960.

13. Kingsland, L., Jr., Experimental Study of Helium and Argon Diffusion in the Wake of a Circular Cylinder at M = 5.8, GALCIT Hypersonic Research Project, Memorandum No. 60, June 1, 1961.

14. Dewey, C. F., Jr., Hot-Wire Measurements in Low Reynolds Number Hypersonic Flows, GALCIT Hypersonic Research Project, Memorandum No. 63, September 15, 1961. Also, American Rocket Society Journal, pp 1709-1718, December, 1961.

15. GALCIT Hypersonic Research Project, Semi-Annual Status Report, April 1962.

16. Feldman, S., On Trails of Axi-Symmetric Hypersonic Blunt Bodies Flying Through the Atmosphere, AVCO-Everett Research Laboratory, Research Report No. 82, December 1959. Also, Journal of the Aerospace Sciences, Vol. 28, No. 6, pp 433-448, 470, June, 1961.

17. Lykoudis, P. S., Theory of Ionized Trails for Bodies at Hypersonic Speeds, The RAND Corp., Report No. RM-2682-1-PR, May 29, 1961, revised October 5, 1961.

18. Kubota, T., Laminar Wake With Streamwise Pressure Gradient, GALCIT Internal Memo, April 1962.

19. Baloga, P. E. and Nagamatsu, H. T., Instrumentation of GALCIT Hypersonic Wind Tunnels, GALCIT Memorandum No. 29, July 31, 1955.

20. GALCIT Hypersonic Research Project, Quarterly Status Report No. 19, April 1 to July 1, 1960.

21. Lilley, G. M. and Morton, D., The Response Time of Wind Tunnel Pressure Measuring Systems, College of Aeronautics, Cranfield, Report No. 141, November, 1960.

22. Smotherman, W. E. , A Miniature Wafer-Style Pressure Transducer, Arnold Engineering Development Center, Report No. AEDC-TR-60-11, October 1960.

23. Nodelman, H. M. and Smith, F. W. , Mathematics for Electronics, McGraw-Hill Book Company, Inc. , New York, 1956.

24. Laufer, J. and McClellan, R. , Measurements of Heat Transfer from Fine Wires in Supersonic Flows, J. Fluid Mech. , Vol. 1, No. 3, pp 276-289, September 1956.

25. Tewfik, O. K. and Giedt, W. H. , Heat Transfer, Recovery Factor and Pressure Distributions Around a Cylinder Normal to a Supersonic Rarefied Air Stream, Part I, Experimental Data, University of California, Berkeley, Technical Report HE-150-162, 30 January 1959. Also, Journal of the Aerospace Sciences, Vol. 27, No. 10, pp 721-729, October, 1960.

26. Demetriades, A. , Private Communications 1961-2.

27. Howarth, L. (editor), Modern Developments in Fluid Dynamics, High Speed Flow, Vol. II, p. 684; Clarendon Press, Oxford, 1953.

28. Matthews, M. L. , An Experimental Investigation of Viscous Effects on Static and Impact Pressure Probes in Hypersonic Flow, GALCIT Hypersonic Research Project, Memorandum No. 44, June 2, 1958.

29. Hill, J. A. F. , Baron, J. R. and Schindel, L. H. , Mach-Number Measurements in High-Speed Wind Tunnels, MIT Naval Supersonic Wind Tunnel, Technical Report 145, January 1956.

30. Marson, G. B. and Lilley, G. M. , The Displacement Effect of Pitot Tubes in Narrow Wakes, College of Aeronautics, Cranfield, CoA Report No. 107, October 1956.

31. Hayes, W. D. and Probstein, R. F. , Hypersonic Flow Theory, Academic Press, New York, 1959.

32. Ames Research Staff, Equations, Tables, and Charts for Compressible Flow, NACA TR 1135, 1953

33. LeBlanc, L. P. and Webb, H. G. , Jr. , Boundary Layer Separation in a Supersonic Stream, North American Aviation, Inc. , Report No. SID 61-72, 29 March 1961.

34. Chapman, D.R., Kuehn, D.M. and Larson, H.K., Investigation of Separated Flows in Supersonic and Subsonic Streams with Emphasis on the Effect of Transition, NACA Rep. 1356, 1958.

35. Hakkinen, R.J., Greber, I., Trilling, L. and Abarbanel, S.S., The Interaction of an Oblique Shock Wave With a Laminar Boundary Layer, NASA Memo 2-18-59W, March 1959.

36. Liepmann, H.W. and Roshko, A., Elements of Gas Dynamics, John Wiley & Sons, Inc., New York, 1957.

37. Eshbach, O.W., Handbook of Engineering Fundamentals, 2nd Ed., p. 7-121; John Wiley & Sons, Inc., New York, 1952.

38. Chapman, D.R., An Analysis of Base Pressure at Supersonic Velocities and Comparison With Experiment, NACA TN 2137, July 1950.

39. Greber, I., Shock-Wave Laminar-Boundary-Layer Interaction on a Convex Wall, NASA TN D-512, October 1960.

40. Guman, W.J., On The Plateau and Peak Pressure of Regions of Pure Laminar and Fully Turbulent Separation in Two-Dimensional Supersonic Flow, Journal of the Aerospace Sciences, Readers' Forum, Vol. 26, No. 1, p. 56, January 1959.

41. Gold, H., Laminar Wake with Streamwise Pressure Gradient for Arbitrary Initial Velocity and Enthalpy Distributions, GALCIT Internal Memo, May, 1962.

42. Slattery, R.E. and Clay, W.G., Experimental Measurement of Turbulent Transition, Motion, Statistics and Gross Radial Growth Behind Hypervelocity Objects, M.I.T. Lincoln Laboratory Preprint JA-1891, April 1962.

43. Wood, R.D., An Experimental Investigation of Hypersonic Stagnation Temperature Probes, GALCIT Hypersonic Research Project, Memorandum No. 50, July 15, 1959.

44. Gorecki, J., An Investigation of Temperature Fluctuations on Bluff Bodies, PhD Thesis Department of Aeronautical Engineering, California Institute of Technology, 1960.

45. Hirschfelder, Bird, Curtiss, and Spotz, The Transport Properties of Gases and Geseous Mixtures from the Princeton Series on High Speed Aerodynamics and Jet Propulsion, Vol. I, Thermodynamics and Physics of Matter, Rossini, F. D. (editor), Princeton University Press, 1954.

46. Keyes, F. G., The Heat Conductivity, Viscosity, Specific Heat and Prandtl Numbers for Thirteen Gases, Project Squid, TR 37, MIT, 1 April 1952.

47. Graves, J. C., Quiel, N. R. and Nagamatsu, H. T., Impact Pressure and Total Temperature Interpretation at Hypersonic Mach Number, GALCIT Memorandum No. 20, July 26, 1954.

48. NBS-NACA Tables of Thermal Properties of Gases, National Bureau of Standards, 1949 with later additions.

APPENDIX A

FLOW CALIBRATION AND VISUALIZATION

The calibration of the Tate-Emery gauge used to control the reservoir pressure was checked against a mercury manometer and found to be within the accuracy of automatic control (±0.02 psig). Atmospheric pressure was measured by a conventional precision mercury barometer to an accuracy of ±0.01 cm mercury. The calibration of the reservoir temperature was checked using the iron-constantan thermocouple shown in Figure 56, employing conventional apparatus.

The thermocouple was located just upstream of the throat at the centerline of the wind tunnel. It was found that the dial setting was high because the thermocouple used for automatic temperature control was located about 12 inches upstream of the throat, consequently, losses through a section of the wind tunnel walls were present before expansion through the nozzle. This fact accounts for the odd nominal temperature of 262 F selected for the tests and the slight variation with pressure. The dial setting for reservoir temperature was maintained constant throughout the tests, and it was calibrated for the full range of reservoir pressures available (Table I).

In the calibration of wind tunnel reservoir temperature, the recovery factor of the iron-constantan thermocouple was assumed equal to one
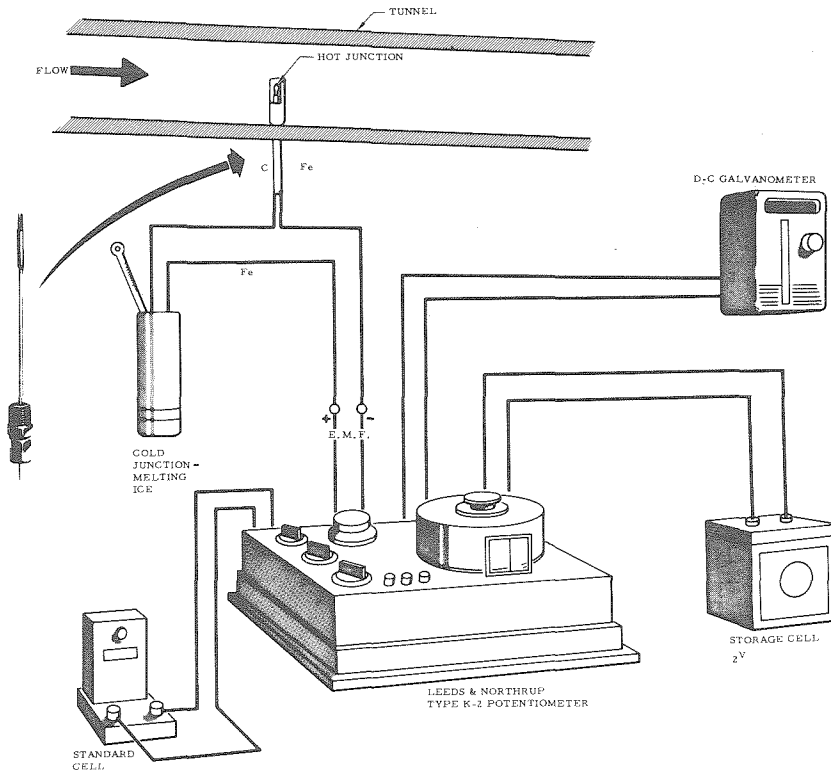
Figure 56. System for Calibrating Wind Tunnel Reservoir Temperature

because the hot junction was located in a subsonic region of high pressure.
The time constant of the temperature measuring system was very short
because of the relatively high-pressure air engulfing the thermocouple.
The accuracy of the temperature calibration was well within the capability
of the automatic control system (± 1.0 F). The results of these measure-
ments agree with those conducted by Wood (Reference 43) and Dewey
(Reference 14) as well as with the wind tunnel empty measurements made
by the author in conjunction with the wake surveys using a chromel-alumel
heated thermocouple (Section II).

To calibrate the wind tunnel, a conventional rake shown in Figure 57
was used. The rake was connected to a bank of silicone manometers which
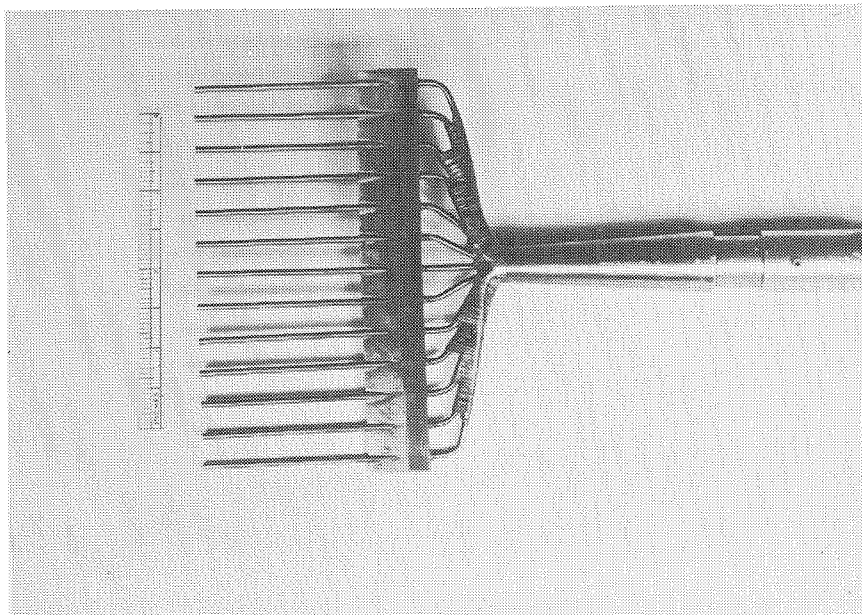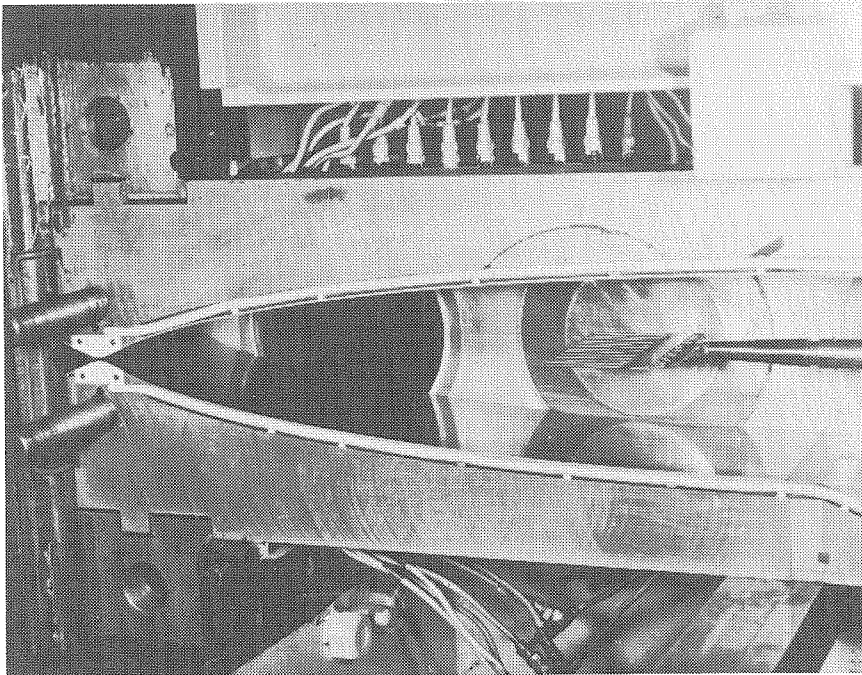
Figure 57. Rake Installation

were read manually. These data were then fed into an IBM 7090 program to obtain pressure contours, a few typical contours are shown in Figure 58. From these contours, it was evident that the flow was very uniform in the region immediately downstream of the cylindrical model (19 to 24 inches from the throat). It should be noted that the flow deteriorates with decreasing wind tunnel stagnation pressure so that the contours of Figure 58 represent close to the worst conditions.

A schlieren photograph of the flow around the model is shown in Figure 1. To obtain this schlieren, the model was embedded in the glass ports of the wind tunnel in which were drilled 1/4-inch holes approximately 1/4-inch deep for support. These holes were very carefully and slowly drilled into the ports in order to avoid stresses in the glass. This procedure, which allowed for easy model installation and minimum leakage at the model supports, was possible because the dynamic pressure on the model was very low; consequently, high forces due to air loads were not present. It might be mentioned that the schlieren shown in Figure 1 was taken with the knife edge horizontal. Photographs were also taken with the knife edge vertical; however, the density gradients in the axial direction were too low for satisfactory visible display.

Some effort was expended in trying to take spark pictures in a time interval short enough to see the microscopic wake structure. At a nominal velocity of 2740 ft/sec (which results from isentropic expansion to Mach 5.7 with the wind tunnel stagnation temperature of 262 F) the flow advances about 0.033 inch during 1.0 microsecond.
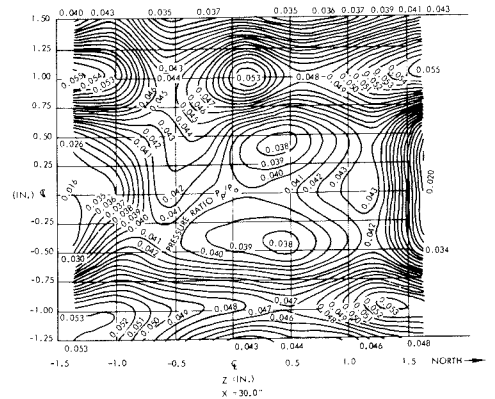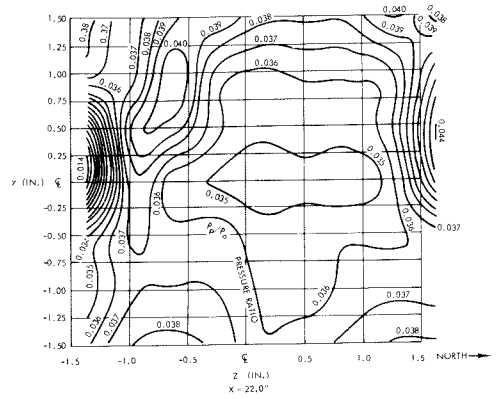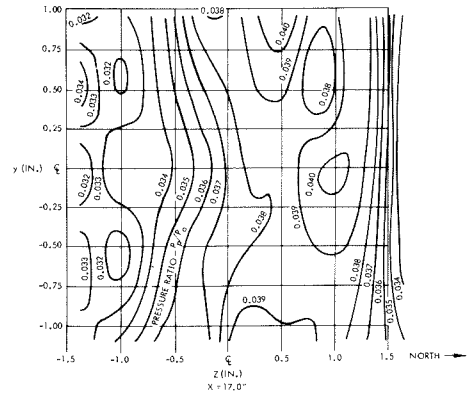
Figure 58. Pressure Contours for Empty Wind Tunnel

One microsecond, then, appears to be the largest order of magnitude of the time interval which must be achieved for visible microscopic wake investigation. In this time interval, it is very difficult to get light intensities high enough for schlieren photographs. An open air spark gap developed by Gorecki (Reference 44) was tried. This source provided time intervals of several microseconds with enough intensity to give photographs using sensitive film. However, due to the flow motion and the resultant smearing, no additional phenomena were visible over the longer-exposure-time schlierens. The project was therefore abandoned.

APPENDIX B

HEATED THERMOCOUPLE

The heated thermocouple used for total-temperature measurements is shown in Figure 23. The supports were heated to the same value as the measured wire temperature by the design shown in Figure 59. In Figure 59, it will be noted that three thermocouples were used, one for measuring the total temperature of the airstream, and one for measuring the support temperature at each end of the wire. The output from the thermocouple at the alumel support was fed into the servo along with the output from the thermocouple at the center of the wire.

The servo compared these two outputs and heated the alumel support, making the difference in outputs equal to zero. The temperature of the chromel support was then adjusted by comparing the output of its thermocouple with that of the alumel support with a sensitive galvanometer. The chromel-heated or the alumel-heated (or both) thermocouples were adjusted by varying the resistances shown in Figure 59; therefore, at equilibrium, both the servo and the galvanometer were nulled.

The servomechanism used was developed by Wood (Reference 43) for a heated shielded thermocouple. The system consists of a dc null detector, a CAT (current adjusting type) control unit, and a power manipulator.
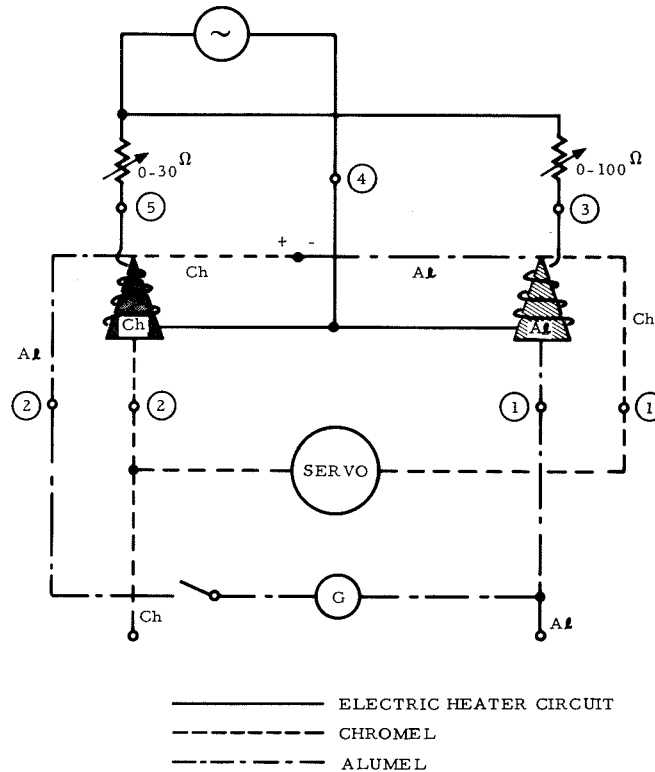
Figure 59. Schematic of Heated Thermocouple Probe

These elements are all commercially available. The dc null detector

measures the difference in output between two thermocouples. Its signal

is fed into the CAT control unit which, in turn, adjusts the power manipu-

lator. The CAT incorporates provisions for obtaining stability and

minimum response to demand changes.

The calibration needle shown in Figure 23 was used to determine

axial distances accurately. First, the distance between its tip and the

thermocouple junction was measured with an optical comparator. Then

the tip was allowed to barely touch the model during tunnel operation after

thermal equilibrium had been established. After axial distance was fixed

and the axial counter set, the calibration needle was then removed.

The chromel-alumel cold junction was coated with wax to eliminate spurious voltages induced by the melting ice. A chromel-alumel thermo-couple was selected for this experiment for the following reasons: neither metal is corrosive, the combination gives out a reasonably large output compared to other metals, and both metals are readily available. As indicated in Figure 23, the heated thermocouple allows for the use of 5-mil wire rather than the very thin wire necessary with conventional means. For this reason, the chances of breaking the wire due to wind tunnel starting loads are minimized.

APPENDIX C

TRANSPORT PROPERTIES

Because of the very low static temperatures in the test section, the conventional Sutherland formula for coefficient of viscosity was suspected -- especially since no experimental data for coefficient of viscosity for dry real air exists below 180 F. Therefore, the coefficient of viscosity was computed using the Lennard-Jones potential as outlined by Hirschfelder, Bird, Curtiss, and Spotz (Reference 45). The results of these computations are shown in Figure 60 and Table IV. Along with the
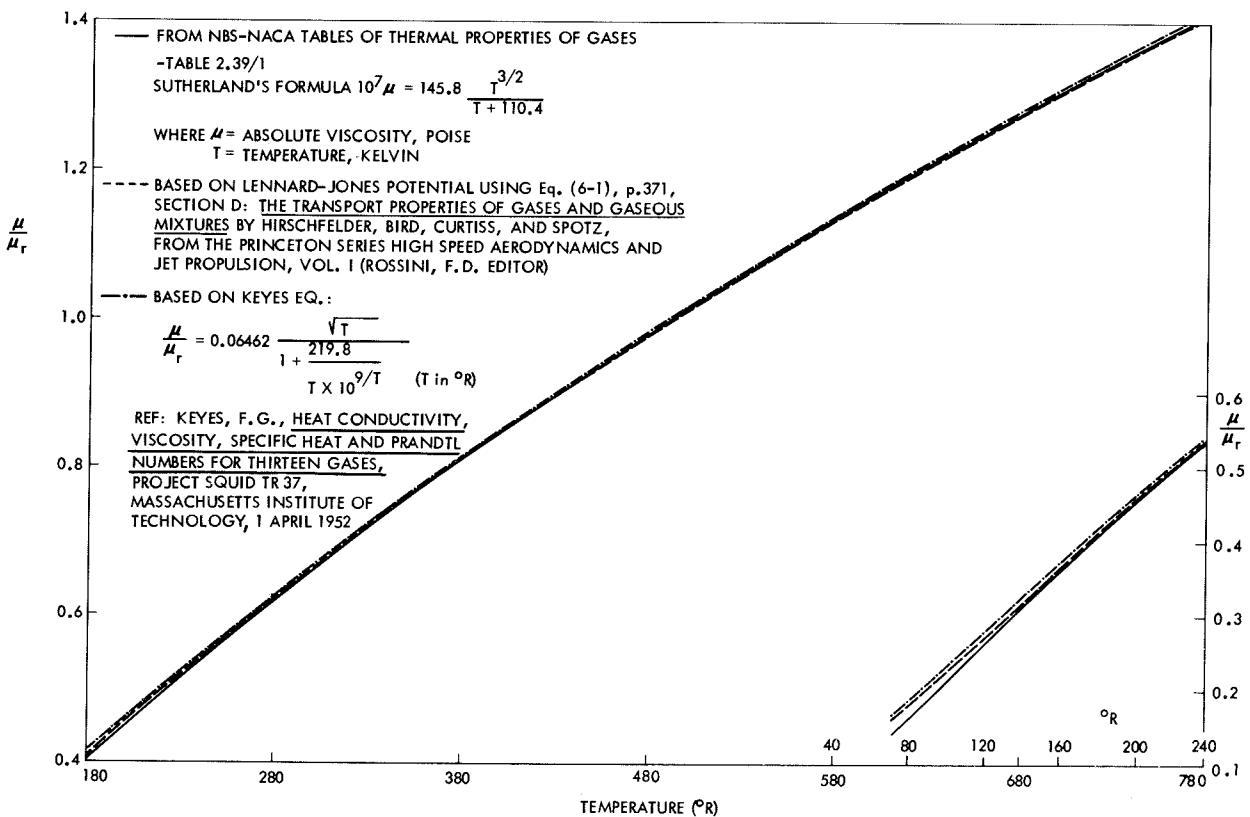
Figure 60. Coefficient of Viscosity for Air Versus Temperature

values based on the Sutherland formula and the Lennard-Jones potential,
a curve based on Keyes' equation * (Reference 46) is also shown in Figure
60. Reynolds numbers based on the coefficients of viscosity given in
Figure 61 were used for all computations.

In a manner similar to that discussed above for viscosity, the
thermal conductivity of air was calculated for low static temperatures,
based on the Eucken assumption of fast energy transfer as presented by
Hirschfelder, Bird, Curtiss, and Spotz (Reference 44). The results of
these computations are shown in Figure 62. To compute the Prandtl
number, the experimental values of specific heat for dry real air
presented in Figure 63 were taken from Reference 48. The Prandtl
number based on these properties is shown in Figure 64.

---

*It should be noted that Keyes' equation as given by Graves, Quiel, and
Nagamatsu (Reference 47) and Matthews (Reference 28) contains errors.

Table IV
Coefficient of Viscosity for Air
Based on Lennard-Jones Potential

$$(\mu/\mu_r) = (T/T_r)^{1/2} \frac{g(\tau)}{g(\tau_r)} \frac{Y(2,2;\tau_r)}{Y(2,2;\tau)}$$

Choose:
$$T_r = 273.16\,°K \ (= 491.69\,°R)$$

$$\mu_r = 1716 \times 10^{-7} \text{ poise (g/sec-cm)}$$

$$\tau = (kT/\epsilon)$$

$$k, \epsilon = \text{force constants}$$

for air $\epsilon/k = 97.0\,°K$

Viscosity Functions							Comparison With Experiment		
τ	Y(2, 2)	g	τ	Y(2, 2)	g	T(°K)	μ exptl. (10⁻⁷ poise)	$\mu_{calc.}$
0.30	2.785	1.0014	2.7	1.069		100	713	702
0.35	2.628		2.8	1.058		120	846	840
0.40	2.492		2.9	1.048		140	975	972
0.45	2.368		3.0	1.039	1.0034	160	1101	1099
0.50	2.257	1.0002	3.1	1.030		180	1221	1221
0.55	2.156		3.2	1.022		200	1336	1337
0.60	2.065		3.3	1.014		220	1448	1447
0.65	1.982		3.4	1.007		240	1556	1554
0.70	1.908		3.5	0.9999		260	1659	1657
0.75	1.841	1.0000	3.6	0.9932		280	1756	1756
0.80	1.780		3.7	0.9870		293.16	1819	1819
0.85	1.725		3.8	0.9811		300	1851	1851
0.90	1.675		3.9	0.9755		400	2294	2290
0.95	1.629		4.0	0.9700	1.0049	500	2680	2678
1.00	1.587	1.0000	4.1	0.9649		800	3613	3680
1.05	1.549		4.2	0.9600		1000	4165	4257
1.10	1.514		4.3	0.9553		1200	4631	4761
1.15	1.482		4.4	0.9507		1500	5262	5494
1.20	1.452		4.5	0.9464		5000		12080
1.25	1.424	1.0001	4.6	0.9422		10000		18870
1.30	1.399		4.7	0.9382				
1.35	1.375		4.8	0.9343				
1.40	1.353		4.9	0.9305				
1.45	1.333		5	0.9269	1.0058			
1.50	1.314	1.0004	6	0.8963				
1.55	1.296		7	0.8727				
1.60	1.279		8	0.8538				
1.65	1.264		9	0.8379				
1.70	1.248		10	0.8242	1.0075			
1.75	1.234		20	0.7432				
1.80	1.221		30	0.7005				
1.85	1.209		40	0.6718				
1.90	1.197		50	0.6504	1.0079			
1.95	1.186		60	0.6335				
2.00	1.175	1.0014	70	0.6194				
2.1	1.156		80	0.6076				
2.2	1.138		90	0.5973				
2.3	1.122		100	0.5882	1.0080			
2.4	1.107		200	0.5320				
2.5	1.093	1.0025	300	0.5016				
2.6	1.081		400	0.4811	1.0080			

LENNARD-JONES POTENTIAL	
$T_{°R}$	μ/μ_r
54	0.1257
72	.1638
90	.2024
93.6	.2103
95.4	.2144
97.2	.2184
108	.2426

FAIRING	
$T_{°R}$	μ/μ_r
126	.2830
144	.3235
162	.3630

NBS-NACA TABLES	
μ/μ_r	$T_{°R}$
0.4038	180
0.4448	198
0.4848	216
0.5239	234
0.5621	252
0.5994	270
0.6359	288
0.6716	306
0.7065	324
0.7407	342
0.7742	360
0.8070	378
0.8391	396
0.8706	414
0.9015	432
0.9319	450
0.9617	468
0.9909	486
1.020	504
1.048	522
1.076	540
1.103	558
1.130	576
1.157	594
1.183	612
1.209	630
1.234	648
1.259	666
1.283	684
1.308	702
1.332	720
1.356	738
1.379	756
1.402	774
1.425	792
1.448	810

TO CONVERT TABULATED VALUED OF	TO	HAVING THE DIMENSIONS INDICATED BELOW	MULTIPLY BY
μ/μ_r	μ	POISE OR G (M) SEC^{-1} CM^{-1}	1716×10^{-7}
		CENTIPOISE	1716×10^{-5}
		G (F) SEC CM^{-2}	1.7498×10^{-7}
		KG (F) SEC M^{-2}	1.7498×10^{-6}
		LB (F) SEC IN^{-2}	2.4889×10^{-9}
		LB (F) SEC FT^{-2} (SLUG/FT SEC)	3.5840×10^{-7}
		LB (M) SEC^{-1} FT^{-1}	1.1531×10^{-5}
		LB (M) SEC^{-1} IN^{-1}	9.6093×10^{-7}

FAIRING

FROM NBS-NACA TABLE OF THERMAL PROPERTIES OF GASES - TABLE 2.39/1, COEFFICIENT OF VISCOSITY OF DRY AIR

BASED ON LENNARD-JONES POTENTIAL USING EQ. (6-1), P. 371, SECTION D: THE TRANSPORT PROPERTIES OF GASES AND GASEOUS MIXTURES BY HIRSCHFELDER, BIRD, CURTISS, AND SPOTZ, FROM THE PRINCETON SERIES HIGH SPEED AERODYNAMICS AND JET PROPULSION, VOL. I (ROSSINI, F. D. EDITOR).
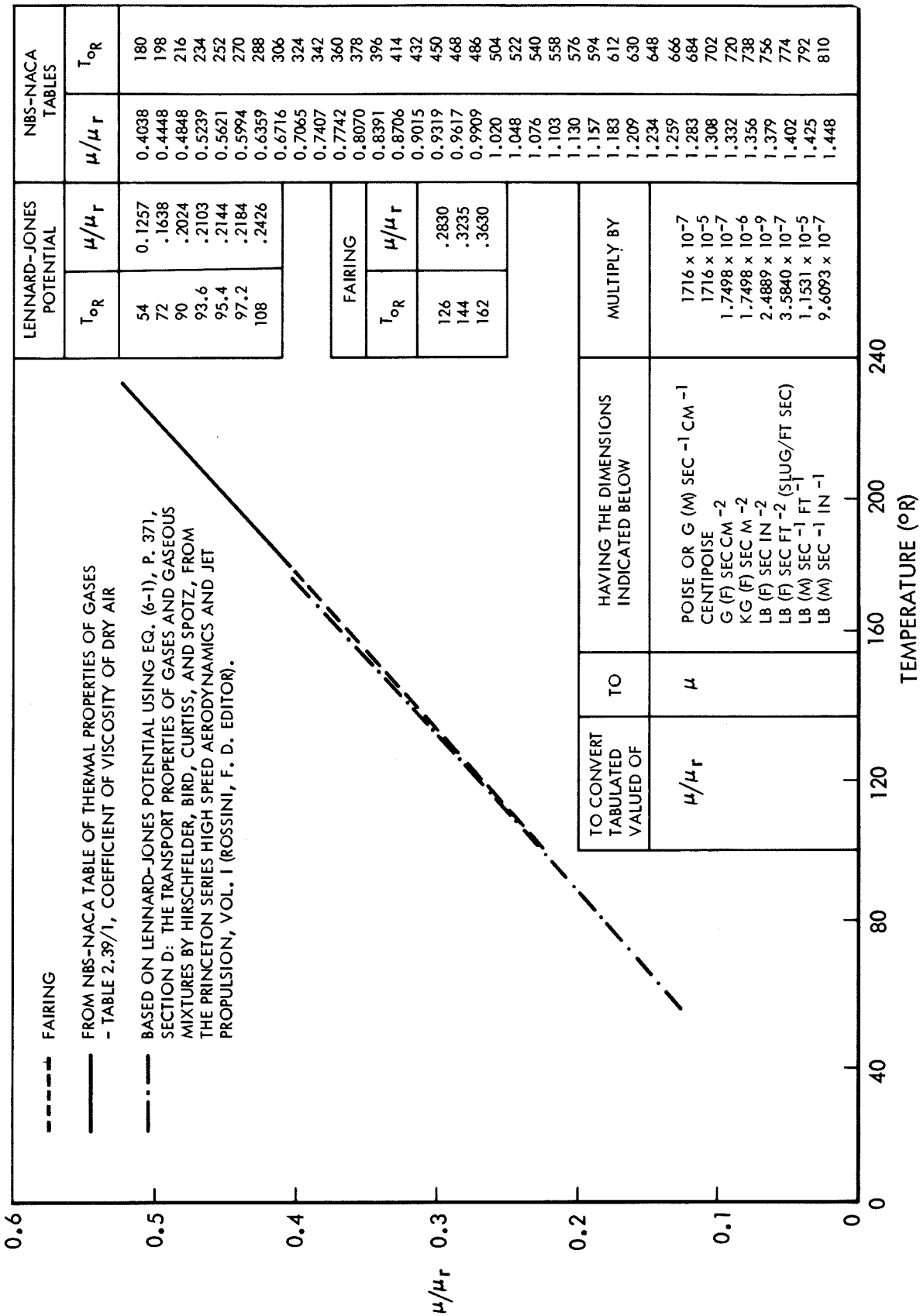
Figure 61. Values Used for Coefficient of Viscosity for Air at Low Temperatures
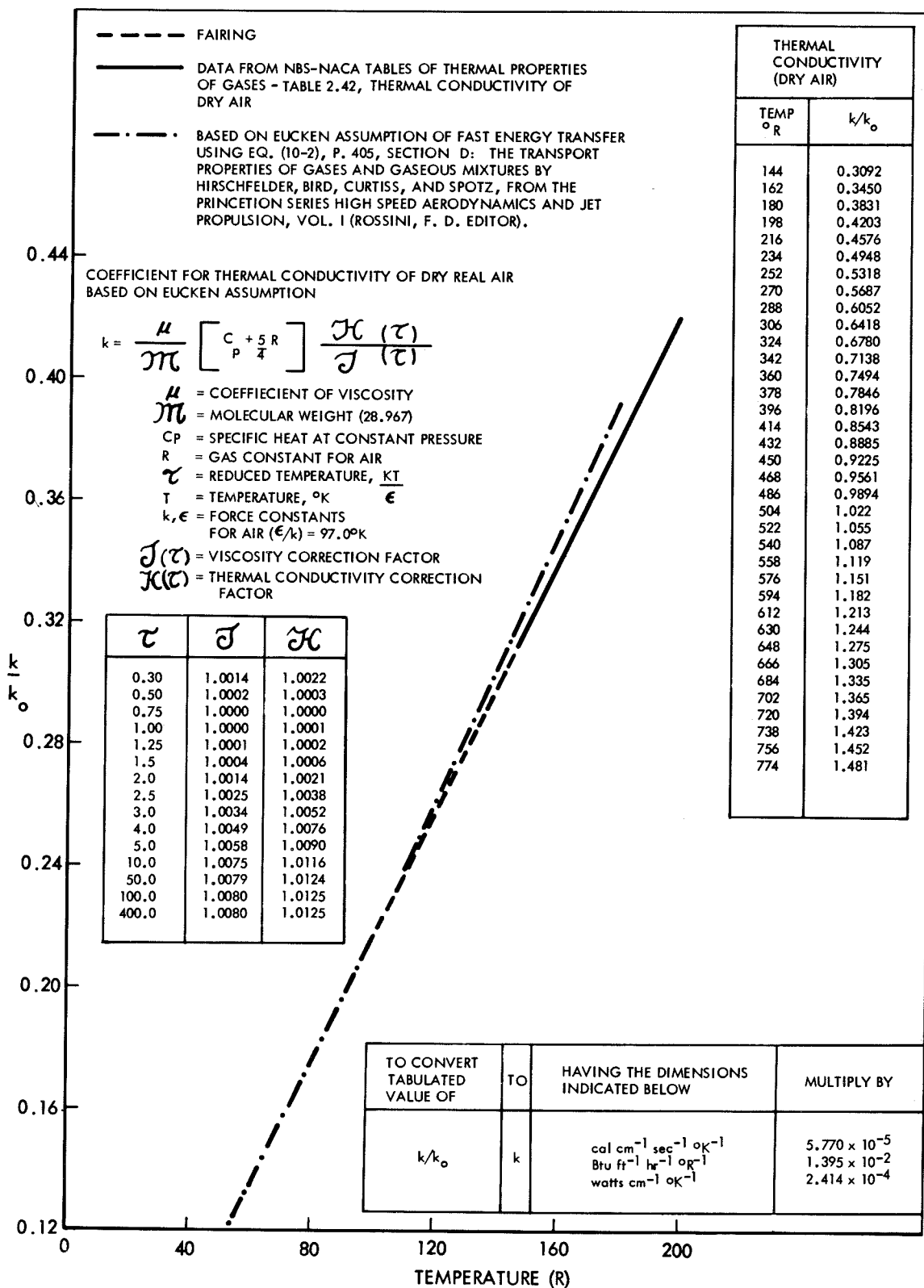
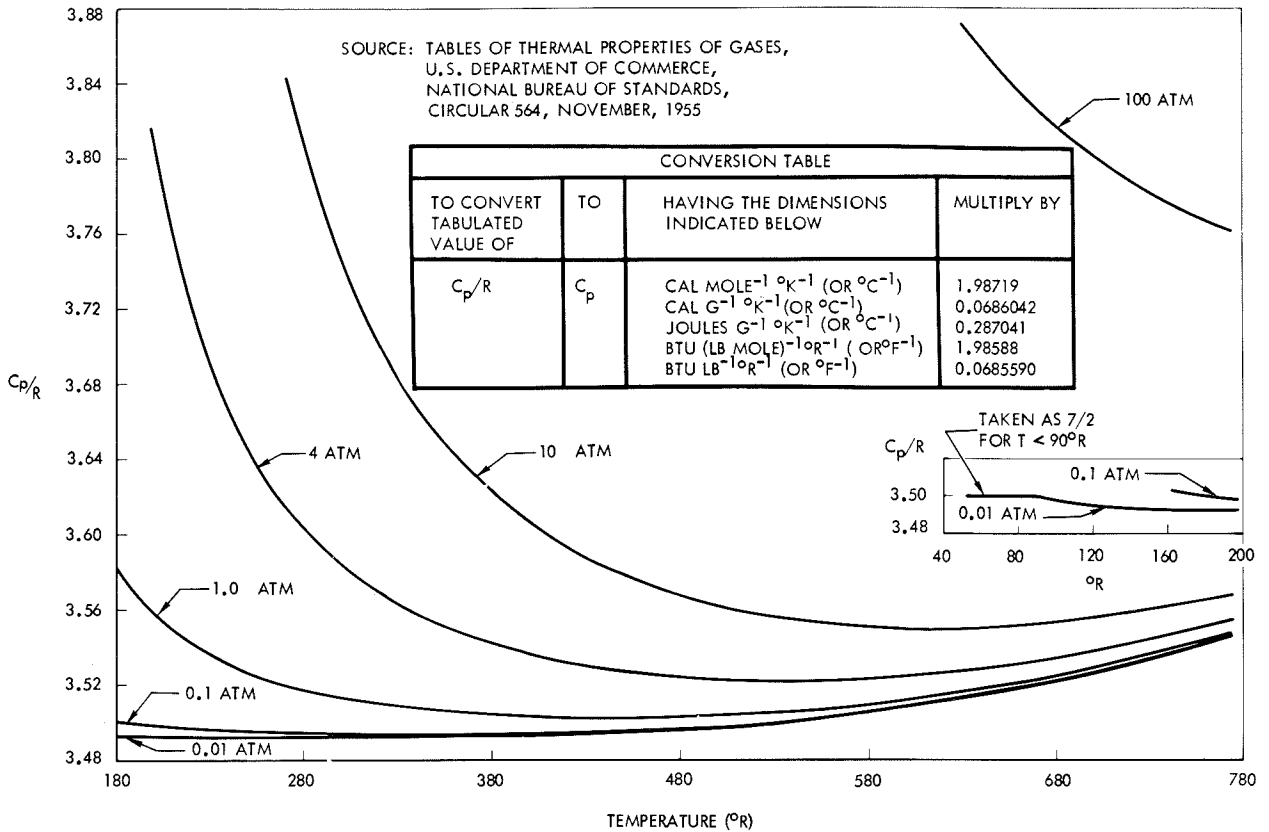Figure 62. Thermal Conductivity of Dry Real Air

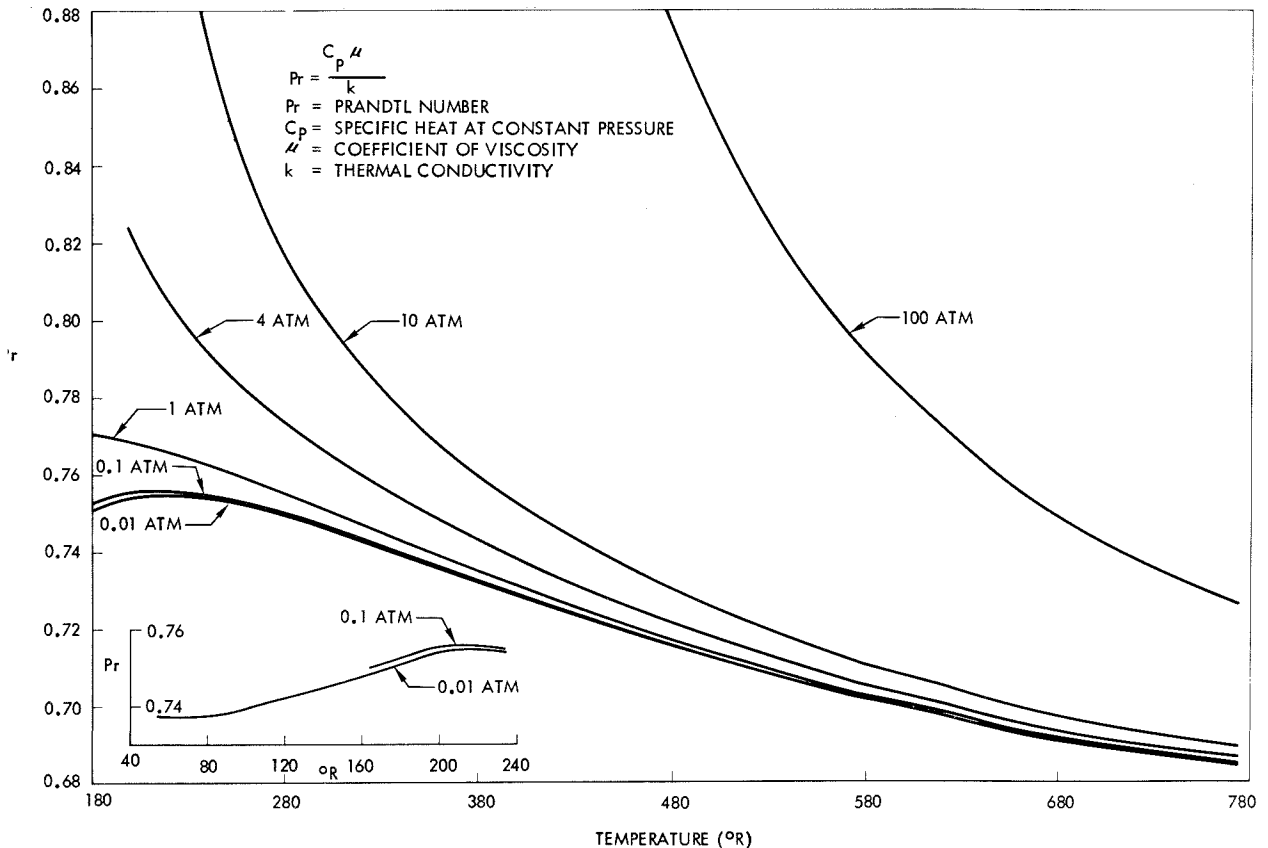Figure 63. Specific Heat at Constant Pressure for Dry Real Air

Figure 64. Prandtl Number for Dry Real Air

APPENDIX D

LAMINAR-WAKE THEORY

Using Kubota's approach (Reference 18), it is assumed that the flow in the viscous wake can be described by the boundary-layer type equations:

$$\frac{\partial(\rho u)}{\partial x} + \frac{\partial(\rho v)}{\partial y} = 0 \tag{1}$$

$$\rho u \frac{\partial u}{\partial x} + \rho v \frac{\partial u}{\partial y} = \rho_e u_e \frac{du_e}{dx} + \frac{\partial}{\partial y}\left(\mu \frac{\partial u}{\partial y}\right) \tag{2}$$

$$\frac{\partial p}{\partial y} = 0 \tag{3}$$

$$\rho u \frac{\partial H}{\partial x} + \rho v \frac{\partial H}{\partial y} = \frac{\partial}{\partial y}\left(\frac{\mu}{\sigma} \frac{\partial H}{\partial y}\right) - \frac{\partial}{\partial y}\left(\frac{1-\sigma}{\sigma} \mu u \frac{\partial u}{\partial y}\right) \tag{4}$$

where the total enthalpy,

$$H = h + \frac{1}{2} u^2, \tag{5}$$

and assuming a perfect gas,

$$p = \frac{\gamma - 1}{\gamma} \rho h . \tag{6}$$

The boundary conditions of symmetry and free-stream flow at infinity apply, viz:

$$\left.\begin{aligned}
\frac{\partial u}{\partial y}(x, 0) &= 0 \quad ; & u(x, \pm\infty) &= u_e(x) \\[2ex]
\frac{\partial H}{\partial y}(x, 0) &= 0 \quad ; & H(x, \pm\infty) &= H_e
\end{aligned}\right\} \tag{7}$$

The following transformation is used

$$\bar{x}(x) = \int_0^x \frac{\rho_e \mu_e u_e}{\rho_\infty \mu_\infty u_\infty} \frac{dx}{d} \tag{8}$$

$$\bar{y}(x,y) = \frac{u_e}{u_\infty} \sqrt{Re_d} \int_0^y \frac{\rho}{\rho_\infty} \frac{dy}{d} \tag{9}$$

then the differential Equations (2) and (4) become

$$\bar{u} \frac{\partial \bar{u}}{\partial \bar{x}} + \bar{v} \frac{\partial \bar{u}}{\partial g} = (g - u^2) \frac{1}{M_e} \frac{dM_e}{dx} + \frac{\partial^2 \bar{u}}{\partial \bar{y}^2} \tag{10}$$

$$\bar{u} \frac{\partial g}{\partial \bar{x}} + \bar{v} \frac{\partial g}{\partial \bar{y}} = \frac{1}{\sigma} \frac{\partial^2 g}{\partial \bar{y}^2} - \frac{1 - \sigma}{\sigma} \frac{(\gamma - 1) M_e^2}{1 + \frac{\gamma - 1}{2} M_e^2} \frac{\partial}{\partial \bar{y}} \left(\mu \frac{\partial \bar{u}}{\partial \bar{y}} \right) \tag{11}$$

where, from continuity

$$\bar{u} = \frac{u}{u_e} \tag{12}$$

and, by definition

$$g = \frac{H}{H_e} \tag{13}$$

It is assumed that the Prandtl number is constant (not necessarily = 1), and, analogous to the Chapman-Rubesin relation for linear temperature-viscosity relationship,

$$\rho \mu = \rho_e \mu_e \tag{14}$$

In order to linearize Equations 10 and 11 first, let

$$\bar{u} = 1 - w \tag{15}$$

$$G = g - 1 \tag{16}$$

and assume the velocity defect, $w \ll 1$. Substituting into Equations 10 and 11 and retaining lowest-order terms, we obtain

$$\frac{\partial}{\partial \bar{x}} \left(\frac{h}{h_e} - 1 \right) = \frac{1}{\sigma} \frac{\partial^2}{\partial \bar{y}^2} \left(\frac{h}{h_e} - 1 \right) \qquad (17)$$

$$\frac{\partial}{\partial \bar{x}} (M_e^2 w) + G \frac{dM_e}{d\bar{x}} = \frac{\partial^2}{\partial \bar{y}^2} (M_e^2 w) \qquad (18)$$

where

$$\frac{h}{h_e} - 1 = (\gamma - 1) M_e^2 w + \left(1 + \frac{\gamma - 1}{2} M_e^2 \right) G \qquad (19)$$

with the boundary conditions

$$\left. \begin{array}{l} G = o \\ w = o \end{array} \right\} \text{ at } \begin{array}{l} \bar{x} = \infty \\ \bar{y} = \pm \infty \end{array} \qquad (20)$$

$$\left. \begin{array}{l} \dfrac{\partial w}{\partial \bar{y}} = o \\[2ex] \dfrac{\partial G}{\partial \bar{y}} = o \end{array} \right\} \text{ at } \bar{y} = o \qquad (21)$$

$$w(-\bar{y}) = w(+\bar{y})$$
$$G(-\bar{y}) = G(+\bar{y}) \qquad (22)$$

If

$$G \ll w \qquad (23)$$

Equations 17 and 18 reduce to the diffusion equation

$$\frac{\partial W}{\partial \xi} = \frac{\partial^2 W}{\partial \eta^2} \qquad (24)$$

with homogeneous boundary conditions and symmetry

$$W = o \Big\} \text{ at } \quad \begin{matrix} \xi = \infty \\ \\ \eta = \pm \infty \end{matrix}$$

$$\frac{\partial W}{\partial \eta} = o \text{ at } \eta = o \tag{25}$$

$$W(-\eta) = W(+\eta)$$

Using Laplace transform techniques, the general solution of Equations 24 and 25 is

$$\overline{W} = \frac{1}{2} \int_{\eta}^{\infty} W_o(\eta') \frac{1}{\sqrt{p}} e^{-\sqrt{p}(\eta' - \eta)} d\eta'$$

$$+ \frac{1}{2} \int_{-\infty}^{\eta} W_o(\eta') \frac{1}{\sqrt{p}} e^{\sqrt{p}(\eta' - \eta)} d\eta' \tag{26}$$

where

$$\overline{W} = \mathscr{L}\{W\} = \int_o^{\infty} W e^{-p\xi} d\xi \tag{27}$$

and $W_o(\eta)$ represents the initial conditions. If $W_o(\eta)$ is a delta function of strength Q, Equation 26 reduces to

$$\overline{W} = \frac{Q}{2} \frac{1}{\sqrt{p}} e^{-\sqrt{p}\,\eta} \tag{28}$$

or

$$W = \frac{A}{\sqrt{\xi}} e^{-\frac{\eta^2}{4\xi}} \tag{29}$$

Thus, the solutions of Equations (17) and (18) for $G \ll w$ and initial delta functions at the origin of $\bar{x}$ are

$$M_e^2 w = \frac{A}{\sqrt{\bar{x}}} \exp \left(- \frac{\bar{y}^2}{4\bar{x}} \right) \tag{30}$$

$$\frac{h}{h_e} - 1 = \frac{B}{\sqrt{\bar{x}}} \exp \left(- \frac{\sigma \bar{y}^2}{4\bar{x}} \right) \tag{31}$$

where A and B are determined from the initial condition (usually taken at the neck)

$$A = \frac{1}{2} \sqrt{\frac{R_{e_d}}{\pi}} \left(\frac{\rho_e u_e \theta}{\rho_\infty u_\infty d} M_e^2 \right)_0 \tag{32}$$

$$B = \frac{\sqrt{\sigma R_{e_d}}}{2\sqrt{\pi} (\rho_\infty u_\infty d) h_{e_0}} \left[Q + (\rho_e u_e^3 \theta)_0 \right] \tag{33}$$

where θ is the momentum thickness

$$\theta = 2 \int_o^\infty \frac{\rho u}{\rho_e u_e} \left(1 - \frac{u}{u_e} \right) dy \tag{34}$$

and Q is the heat transfer to the body.

From Equation 32

$$\frac{\theta}{\theta_0} = \frac{\left(\rho_e u_e M_e^2 \right)_0}{\rho_e u_e M_e^2} \tag{35}$$

To determine the wake semi-width, y_e, one notes that

$$\frac{y_e}{d}\sqrt{R_{e_d}} = \frac{\rho_\infty u_\infty}{\rho_e u_e}\left[\bar{y}_e + \frac{\gamma-1}{2}M_e^2 G\bar{y}_e + \frac{\gamma-1}{2}\left(M_e^2\frac{\rho_e u_e}{\rho_\infty u_\infty}\frac{\theta}{d}\sqrt{R_{e_d}}\right)_0\right] \qquad (36)$$

where $\bar{y}_e$ is the wake semi-width in the transformed plane.

Assuming that at the wake edge

$$w_e = \frac{1}{N} \qquad (37)$$

then

$$\frac{\bar{y}_e^2}{4\bar{x}} = \ln\frac{N}{2}\sqrt{\frac{R_{e_d}}{\pi}}\left(\frac{\rho_e u_e \theta}{\rho_\infty u_\infty d}M_e^2\right)_0 - \ln M_e^2\sqrt{\bar{x}} \qquad (38)$$

It is interesting to note that

$$\left(\frac{y_e}{d}\right)_0 = \frac{\gamma-1}{2}\left(M_e^2\frac{\theta}{d}\right)_0 \qquad (39)$$